STRATIFIED FIBER-RESONATOR: FABRICATION, CHARACTERIZATION AND POTENTIAL APPLICATIONS

by

Zeba Naqvi

A dissertation submitted to the faculty of
The University of North Carolina at Charlotte
in partial fulfillment of the requirements
for the degree of Doctor of Philosophy in
Optical Science and Engineering

Charlotte

2017

Approved by:

____
Dr. Tsing-Hua Her

____
Dr. Faramarz Farahi

____
Dr. Greg J. Gbur

____
Dr. Shunji Egusa

____
Dr. Stuart T. Smith

ABSTRACT

ZEBA NAQVI. Stratified Fiber-Resonator: Fabrication, Characterization and Potential Applications. (Under the direction of DR. TSING-HUA HER)

Whispering Gallery Mode Resonators (WGMR) are compact, monolithic resonators used for photonic applications. Controlling the properties of WGM while keeping the geometry simple is desired to improve their performance, especially for sensing and non-linear interactions. One way to achieve this is by coating the WGMR with a layer of certain refractive index profile, which has been shown to modify the effective optical potential thus allowing control of the WGM field. This dissertation focusses on coating of an optical fiber with single or multiple thin films with precise control of thickness and refractive index. Transfer matrix method is applied to study the effect of coated films on the mode structures and field profiles of fiber WGM. For small layer thickness the mode shifts to the periphery while for large thicknesses waveguide modes are found and coupling is observed for multiple layers. Fibers are coated uniformly in a commercial PECVD instrument modified to enable continuous rotation of fibers. Mie scattering of coated fibers is utilized to extract refractive index and thickness of coated thin films, which is otherwise challenging due to non-flat topology and small size of the fibers. It is found that rotation leads to higher deposition rate and refractive index of films, compared to those deposited on a static wafer. These differences are demonstrated to depend on the rotation speed, opening interesting dynamic tuning capabilities. Further, fibers with Bragg layers are fabricated and their scattering analyzed. It is found that judicious choice of film thickness can drastically modify scattering signatures of Bragg fibers. A ray model taking into account photonic bandgap of Bragg layers is proposed to successfully explain these anomalous features.

DEDICATION

To my parents

ACKNOWLEDGEMENTS

My long pending gratitude to my PhD supervisor Dr. Tsing-Hua Her. Five years with him transformed me positively at several levels. The freedom he gave me to argue with him based on evidence awakened some dormant energies in me. I might miss that environment where logic reigns supreme. I will also miss the Chinese peanuts he offered to calm me down in our heated discussions. He valued me for who I am and accepted my idiosyncrasies as much as I did his. Thanks for teaching me several soft and hard skills patiently despite occasional locking of horns of true Taurean bulls that we both are.

Complementary to the energetic and ecstatic personality of Dr. Her, were the gentle souls like Dr. Farahi, Dr. Fiddy and Dr. Smith. Witnessing Dr. Fiddy's unmatched people skills, generosity and ultra-efficient management first hand was an enriching experience in itself apart from his insights in the field of scattering. Dr. Farahi's support in my rough times saved me a lot of trouble. His faith in my abilities toned down my imposter syndrome. Speaking of support, Dr. Angela Davies deserves the credit for my finishing PhD in time. Hats off to her for giving me her precious time amidst a heap of responsibilities only she can handle. Big thanks to Dr. Smith who always had our back for electronics and mechanical engineering problems. Thanks to Dr. Egusa for sharing his most up-to-date knowledge on all sorts of multilayered fibers. I would also like to thank Dr. Gbur for his openness to discuss ideas on scattering even outside this project.

One great acquaintance I fortunately made was Dr. Lisa Russell Pinson who taught me that PhD is just the beginning. This realization reset my mind which was lost in striving for unattainable perfection. She supported me behind the scenes for nearly two years selflessly. While on the foreground were my lab mates - Mark Green and Yuanye Liu,

always there for technical and non-technical discussions sweeping a breadth of physical and metaphysical topics. Joseph Peller deserves a special mention for being a true friend-in-need throughout my 5 years at UNC Charlotte. Frances, Jonathan, Ali, Nasim, Farzaneh, Elisa, Patrick, Hossein and many more made my stay here memorable. Thanks to Dr. Asmaa Getan of Math department for her love and free food.

People from my past, Dr. Vasant Natarajan from Indian Institute of Science and Dr. Hema Ramachandran from Raman Research Institute, Bangalore deserve a special mention. These were the scientists who took a chance and let an IT major do experimental atomic physics in their labs. On the other hand discussions with Dr. R. Srikanth on theoretical concepts happened at a higher level of existence, devoid of ego and driven by pure spirit of enquiry. He reassured my faith in physics as a means to reach the truth. Of course he struggles for funding in a world that has forgotten the importance of curiosity that leads to great theories and serendipities. I also thank my friends RK, UT and ET for being supportive from my high school days.

Special thanks to my nephews and nieces Haider, Zahra, Zainab, Naaz and little Naqi spread across the globe. Their innocence and sweet voices are like a healing potion to a stressed mind. Thanks to my brothers-in-law and sisters for encouraging me to take risks I am fond of. Lastly, gratitude to my parents is best unsaid. Expressing it in words will belittle their magnanimous position in my life. This dissertation and every good thing I will ever do is dedicated to them.

TABLE OF CONTENTS

LIST OF TABLES

LIST OF FIGURES

LIST OF SYMBOLS/ABBREVIATIONS

WGM	Whispering Gallery Mode
WGMR	WGM Resonator
GRIN	Graded Index
PECVD	Plasma Enhanced Chemical Vapor Deposition
SMF	Single Mode Fiber
RI	Refractive Index
SEM	Scanning Electron Microscope
LSE	Least Square Error
PBG	Photonic Bandgap
ZNx	Fiber ID#

CHAPTER 1 INTRODUCTION

1.1 Motivation

Microresonators with whispering gallery modes (WGM) are compact, monolithic, mirrorless resonators with high Q-factors, storing light in a small volume near the periphery of the resonator, guided by total internal reflection. Since a WGM is concentrated near the periphery of the resonator, coating the surface of WGM resonator (WGMR) with a radial designer RI (refractive index) profile, graded or step index, offers a way to tune the shape of effective optical potential [1, 2] hence control the properties of modes of the resonator [3]. This can be understood by drawing an analogy between Schroedinger's equation and wave equation in optics, as in [4], where the optical potential for TM polarization in a cylinder (E || axis) with refractive index profile *n(r)* as a function of radius was derived to be:

$$V_{TM} = k^2\left[1-n^2\left(r\right)\right]+\frac{4m^2-1}{4r^2} \tag{1.1}$$

Here k is the vacuum wavevector, r is the radial coordinate and m is the order of Bessel function. The effective optical potential in a cylinder of radius 100 µm, refractive index 1.45 shown in black in the Figure 1.1 develops a deep well when peripheral RI is increased (n=1.7). The width, depth and shape of the potential well can be controlled by RI profile *n(r)* which in turn affects the shape of the mode.

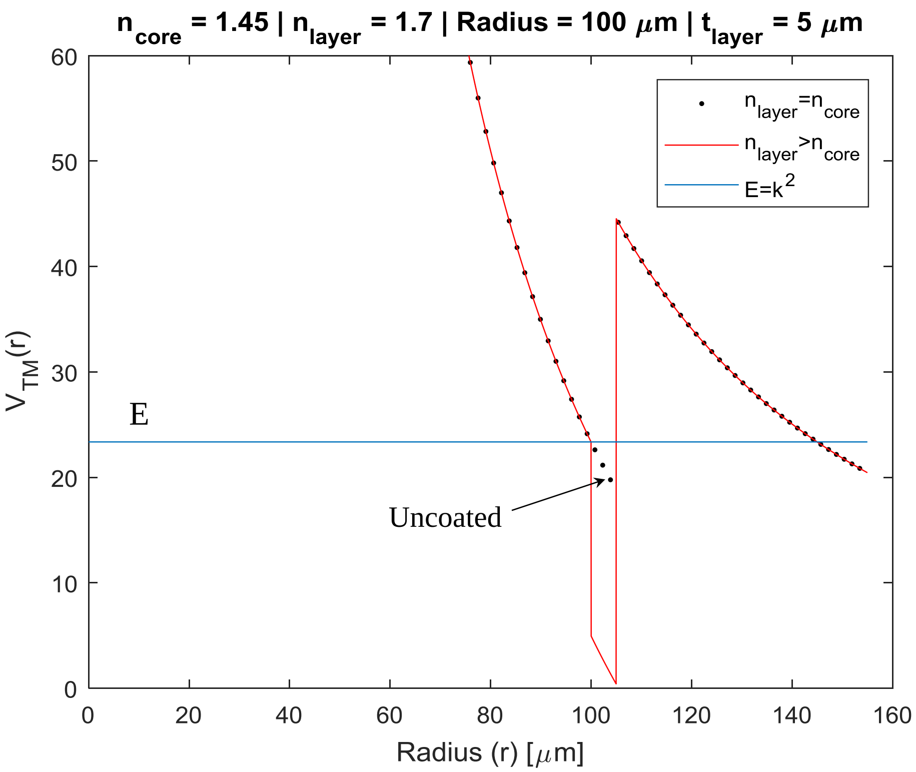

Figure 1.1: Potential function for a 100 µm dielectric cylinder coated with high index dielectric layer. Blue line marks the total energy.

Even though the WGM travels near the surface of the resonator, only a small evanescent tail protrudes outside demanding very high Q-factors. To enhance the sensitivity of a WGM sensor, the tail needs to be either elongated for larger interaction area with the analyte i.e. slower decay or stronger in intensity. The stronger field will induce larger polarization in the analyte thus increasing the sensitivity. Arnold et.al [5] showed that a microsphere coated with a high index subwavelength layer, has WGM field shifted to the periphery and exposed more to the surroundings. Their result is reproduced in Figure 1.2. The field for uncoated case corresponds to t=0. As the thickness of the high index layer increases (keeping the total radius of microsphere constant), the field shifts to the periphery and is compressed exposing a stronger evanescent field. Their result triggered interest in coated WGMRs mainly for sensing applications.

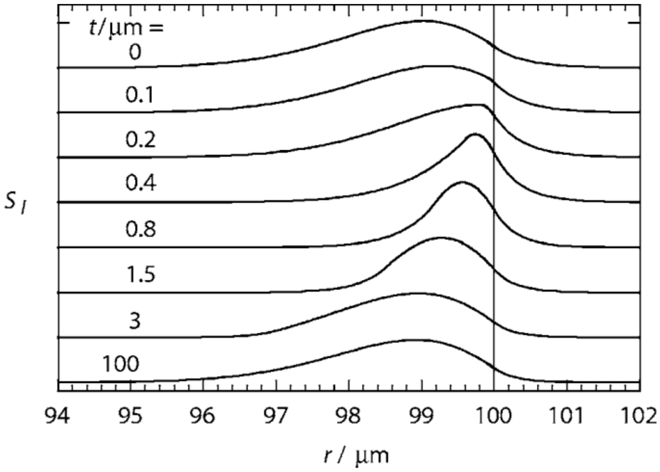

Figure 1.2: Radial function of WGM field in a microsphere coated with layer of n=1.6 and total radius 100 µm. Thickness t is indicated along each curve. Reproduced from [5].

A layer of graded index (GRIN) provides further freedom in tailoring the WGM field distribution and ease of coupling more importantly. Unlike a layer of homogeneous RI, GRIN layer can be designed to smooth out the potential barrier between external medium and the resonator allowing efficient light coupling. Using this principle, [6] showed that radially decreasing GRIN cladding of a Liquid Core Optical Ring Resonator can enhance penetration depth of field coupled from outside since the mode will gravitate toward the center where index is higher. A similar radially decreasing profile was suggested by [7] but in solid core WGMR. In this case the field will withdraw away from the outside into the solid core i.e. negligible evanescent tail. From sensing perspective this is of no use. However, the mode situated deeper inside will be more immune to external disturbances such as presence of the coupling device and hence useful for contact coupling. The coupler can be put in direct contact with the WGMR making the coupler-resonator system more robust. Correct index profile can therefore avoid the problem of maintaining critical gap between the WGMR and coupler. Such a mode being less exposed to the surface experiences lower losses due to surface roughness.

From the perspective of non-linear optics, GRIN is advantageous for tuning phase matching between different radial modes – an advantage not available with single layer of constant index. A radially decreasing index profile has been proposed for dispersion compensation in WGMRs for broadband frequency comb generation [7]. WGMRs with 3D confinement such as microspheres are known to suffer with geometrical dispersion. Higher frequencies travel at larger radial distance i.e. closer to the periphery thus experiencing longer optical path lengths leading to phase mismatch between modes of different frequencies. For applications requiring phase matching such as non-linear phenomena, this dispersion can be mitigated by having refractive index decrease in radial direction so that optical path of different modes is identical allowing exchange of energy. As illustrated in Figure 1.3, constant index WGMR has typically non-equidistant mode spectrum due to poor phase matching between modes of different frequencies traveling at different radii. A GRIN WGMR on the other hand allows a broadband frequency comb by creating equidistant modes. However, these ideas have not been implemented successfully as fabricating graded index profile is challenging due to factors such as coating uniformity, limited range of RI available, optical losses, surface roughness, poor control over RI and thickness.

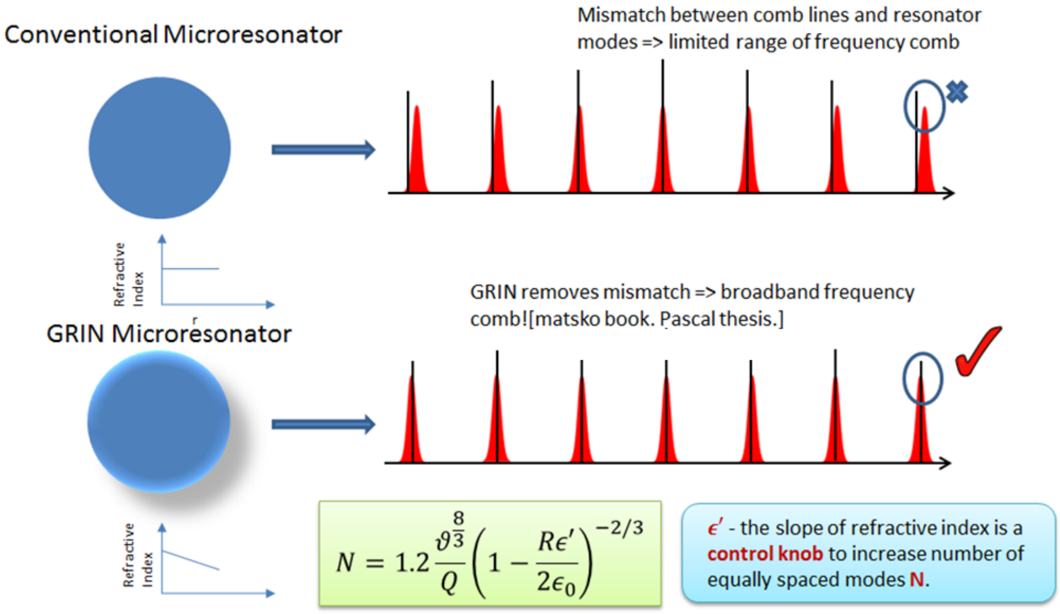

Figure 1.3: Effect of refractive index profile on the spacing of frequency comb teeth.

Apart from such monotonic RI profiles, multilayered step-index profiles have their several unique applications. For example, [8] showed theoretically that WGMs individually sustained in two concentric layers separated by a thick low index layer in a microsphere, can couple together. A system of multiple layers with coupled WGM, would be functionally similar to CROW [9] with multiple coupled resonators. Since splitting of the dispersion curve due to coupling creates regions of flatter dispersion or reduced group velocity, CROWs are used to make sensitive compact gyros [10]. However, it demands identical resonators which is not easy to fabricate. In addition, keeping all the resonators aligned is also difficult. In contrast, a system of radially coupled WGMs would be alignment free, easier to fabricate and lot more compact.

Another important prospective application of multilayered step-index profile on a WGMR would be a Bragg Surface WGMR for sensing. It is known that surface waves, with significant fraction of energy protruding out, exist in all-dielectric finite planar Bragg layers [11, 12], which make them exciting alternatives to surface Plasmon counterpart. If such a stack of layers is deposited on a WGMR, it may sustain a surface wave with a large evanescent tail making a highly sensitive sensor. Being all dielectric, it will be lossless provided the surface is smooth enough. Such a resonator can be realized by depositing Bragg layers onto a WGMR such as a fiber.

To experimentally realize these applications, it is essential to develop fabrication methods for coating WGMRs with layers of controlled thickness and refractive index of wide range. Any related experimental works have been limited to mostly polymers by dip-coat or sol-gel methods which do not provide good control over these parameters. Despite enough theoretical work, there is a lack of experimental realization of the coated WGMRs. Ristic et al. [13] used LPCVD to coat a microsphere with silicon and study the WGM sensor sensitivity as a function of layer thickness. LPCVD, however, requires high processing temperature around 600^0 Celsius and above, depending on film species and precursors, which limits itself to materials that can sustain very high temperature.

In this dissertation, PECVD is adapted to coat optical fiber with silicon Nitride and silica aiming fabrication of a coated WGMR for future work. The use of plasma opens the possibility to incorporate temperature sensitive materials such as chalcogenide and phosphate glass, both of which are important classes of optical materials. Moreover, PECVD allows faster deposition rates of materials with a wide range of refractive index ranging from that of silica to silicon-rich silicon nitride via silicon oxy-nitride. PECVD films have low film stress and precisely controlled thickness, and is a suitable choice for designer step-index or quasi-graded index profiles as already demonstrated on flat wafers [14].

Optical fiber is chosen as the substrate for coated WGMR for its simplicity. All-dielectric fibers such as SMF have been used as WGMRs [3], owing to the inherent monolithic geometry with sub-mm diameter and required surface smoothness. Despite lacking axial confinement, cylinders can sustain strongly localized WGMs with high Q-factors as proved theoretically by Sumetsky [4], making fibers a handy non-trivial candidate for WGMR compared to complicated geometries. Shaping the fibers axially by CO_2 laser machining [1] or splicing [5] can further improve the confinement. With this motivation, this dissertation focuses on fabrication of coated fibers and characterization of the coatings and also explores potential of the coated fiber as a WGMR.

1.2 Outline

The chapters are organized as follows. In CHAPTER 2, transfer matrix method is applied to calculate the radial profile of WGM modes and effect of coating is numerically investigated. This is followed by fabrication of coated fibers in PECVD in CHAPTER 3. CHAPTER 4 deals with non-invasive characterization of the coated layers by Mie scattering, which forms the major part of the dissertation. Lastly, in CHAPTER 5, Mie scattering of the fabricated Bragg fibers is demonstrated and explanation of the anomalous scattering pattern is developed. Conclusion and ideas for future work are provided in CHAPTER 6.

CHAPTER 2 WHISPERING-GALLERY MODE RESONANCE IN COATED FIBERS

2.1 Introduction

The focus of this chapter is to demonstrate the potential of coated fibers for tweaking the WGM resonances. Modification of resonant field distribution resulting in narrower modes with modified evanescent field and stronger dispersion in coated fiber-resonator are demonstrated numerically.

The chapter is organized as follows. In Section 2.2, transfer matrix method is applied to determine the modes in a Bragg fiber with a defect layer. In Section 2.3 results for WGM in fibers coated with single and multiple layers are shown. Among results for single layer, attraction of WGM field toward a thin film exhibiting a stronger evanescent field than uncoated fiber is shown. This is followed by effect of film thickness on the modes, dispersion with film thickness, confinement of the mode in a layer thicker than the wavelength, and field profiles of 0^{th} to higher order radial modes for a given azimuthal order. Further modes in a three layer structure consisting of two layers separated by a spacer layer are studied as a function of spacer layer thickness.

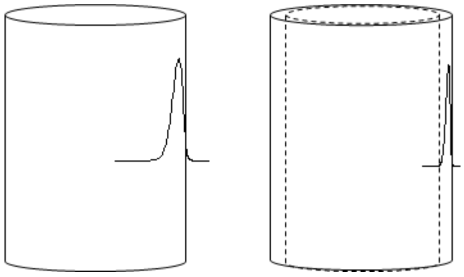

Figure 2.1: WGM mode in uncoated and coated fibers. The coating modifies the radial distribution of the field. High index coating pulls the mode toward the layer.

2.2 Transfer Matrix Method for Multilayered Fibers

This section derives the numerical expression for TM modes in a Bragg fiber. For

TM mode electric field $E_z\left(r,\varphi,z\right)$ exists only in the $\hat{z}$ direction and therefore Helmholtz equation reads,

$$\left(\nabla^2 + k^2\right)E_z(\mathrm{r},\varphi,\mathrm{z}) = 0 \tag{2.1}$$

which in cylindrical coordinates is

$$\left(\frac{1}{r}\frac{\partial}{\partial r}\left(r\frac{\partial}{\partial r}\right)+\frac{1}{r^2}\frac{\partial^2}{\partial\varphi^2}+\frac{\partial^2}{\partial \mathrm{z}^2}+k^2\right)E_z(\mathrm{r},\varphi,\mathrm{z}) = 0\,. \tag{2.2}$$

Substituting $E_z(\mathrm{r},\varphi,\mathrm{z}) = \mathrm{E}_z(\mathrm{r})\,\mathrm{E}_z(\varphi)\,\mathrm{E}_z(\mathrm{z})$ into 2.2, we get the well-known solution,

$$E_z(\varphi) = A_m e^{im\varphi}$$

$$E_z(\mathrm{z}) = \mathrm{e}^{i\beta z}$$

$$E_z(\mathrm{r}) = \mathrm{AJ}_m\left(r\sqrt{k^2-\beta^2}\right)+\mathrm{BY}_m\left(r\sqrt{k^2-\beta^2}\right)\ . \tag{2.3}$$

Here β is the component of propagation constant along $\hat{z}$. For WGM – a mode restricted to the cross-section of the fiber $\beta = 0$. Therefore the radial part is of the form $E_z\left(r\right) = AZ_m\left(kr\right)$, where Z_m is any Bessel function (J_m or Y_m) of order *m*. To represent cylindrical waves, we will use Hankel functions of first and second kinds for outgoing and incoming waves. Therefore 2.3 can be written as

$$E_z(\mathrm{r}) = AH_m^1\left(kr\right)+BH_m^2\left(kr\right) \tag{2.4}$$

Figure 2.2 shows schematic of cross-section of the multilayered cylinder with N layers creating N+1 interfaces separating N+2 domains of constant refractive index. The coefficients of outgoing and incoming cylindrical waves are marked by A_i and B_i respectively in the *i*th domain of refractive index n_i. Coefficients inside the core A_1 and B_1 are written as A_{co} and B_{co} while those in the N+2 domain i.e. outside the cylinder are represented by A_{out} and B_{out}.

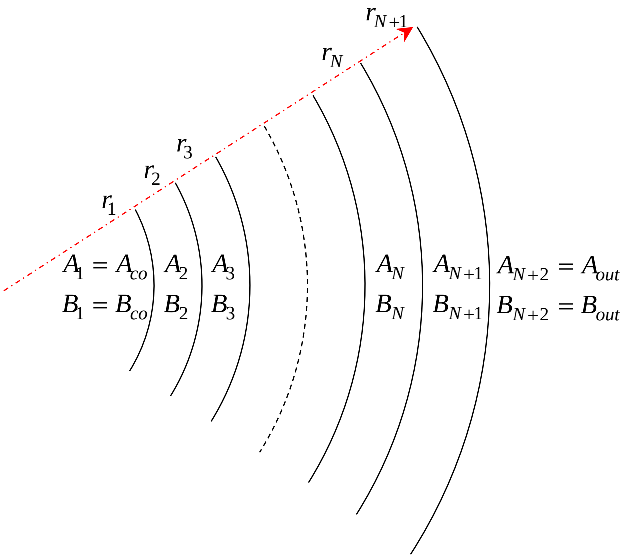

Figure 2.2: Schematic of N layered cylinder cross section showing coefficients of outgoing (A) and incoming (B) cylindrical waves in each region of constant refractive index. For N layers there are N+1 interfaces and N+2 regions.

Since Y_m blows up at the origin, for a mode to exist $A_{co} = B_{co}$ leaving only J_m inside the core. Outside the multilayered cylinder, only outgoing wave exists, hence $B_{out} = 0$. Thus electric field for TM mode as a function of radial coordinate is given by

$$E_z(r) = \begin{cases} 2A_{co} J_m(n_{co}k_0 r), & r < r_1 \\ A_i H_m^1(n_i k_0 r) + B_i H_m^2(n_i k_0 r), & r > r_1 \text{ and } r < r_{N+1} \\ A_{out} H_m^1(n_{out} k_0 r), & r > r_{N+1} \end{cases} . \qquad (2.5)$$

Here k_0 is the free space wavenumber. Being TM mode, the *H* field transverse to *E* has components H_r and H_φ. The boundary conditions require that $E_\parallel$ (E_z) and $H_\parallel$ (H_φ) be continuous. From $\nabla \times E = -\frac{\partial B}{\partial t}$, continuity of $H_\parallel$ translates to continuity of $\frac{\partial E_z}{\partial r}$. Applying the two boundary conditions at interface *i* gives the following pair of equations:

$$A_i H_m^1(k_i r_i) + B_i H_m^2(k_i r_i) = A_{i+1} H_m^1(k_{i+1} r_i) + B_{i+1} H_m^2(k_{i+1} r_i) \qquad (2.6)$$

$$n_i \left(A_i H_m^1{}'(k_i r_i) + B_i H_m^2{}'(k_i r_i) \right) = n_{i+1} \left(A_{i+1} H_m^1{}'(k_{i+1} r_i) + B_{i+1} H_m^2{}'(k_{i+1} r_i) \right). \qquad (2.7)$$

Here $k_i = n_i k_0$ and derivatives are denoted by prime. Writing the above equations in matrix form we get,

$$\underbrace{\begin{bmatrix} H_m^1\left(k_{i+1}r_i\right) & H_m^2\left(k_{i+1}r_i\right) \\ n_{i+1}H_m^1{}'\left(k_{i+1}r_i\right) & n_{i+1}H_m^2{}'\left(k_{i+1}r_i\right) \end{bmatrix}}_{M_i}\begin{bmatrix} A_{i+1} \\ B_{i+1} \end{bmatrix} = \underbrace{\begin{bmatrix} H_m^1\left(k_ir_i\right) & H_m^2\left(k_ir_i\right) \\ n_iH_m^1{}'\left(k_ir_i\right) & n_iH_m^2{}'\left(k_ir_i\right) \end{bmatrix}}_{N_i}\begin{bmatrix} A_i \\ B_i \end{bmatrix} \tag{2.8}$$

Coefficients in adjacent domains are therefore related as follows.

$$\begin{bmatrix} A_i \\ B_i \end{bmatrix} = N_i^{-1}M_i\begin{bmatrix} A_{i+1} \\ B_{i+1} \end{bmatrix}. \tag{2.9}$$

Hence coefficients in core and surrounding are related as

$$\begin{bmatrix} A_{co} \\ B_{co} \end{bmatrix} = N_{N+1}^{-1}M_{N+1}N_N^{-1}M_N \ldots N_1^{-1}M_1\begin{bmatrix} A_{out} \\ B_{out} \end{bmatrix} \tag{2.10}$$

Setting $A_{out} = 1$ and $B_{out} = 0$ all the coefficients can be determined. The mode condition is $A_{co} = B_{co}$. To determine the resonant wavelength, approach similar to Prkna et al. is adopted [15] and the lossy nature of the WGM modes is encompassed by the complex wavelength. In a search space of complex wavelength $\lambda = \lambda_r + \lambda_i$, we look for the λ satisfying the mode condition $A_{co} = B_{co}$. The resonant wavelength $\lambda_{res} \approx \lambda_r$ due to small imaginary part. The code implementing these equations is given in APPENDIX A. The electric field $E_z\left(r\right)$ is obtained by setting $A_{co} = B_{co} = 1$ and determining coefficients of Hankel functions in each layer. Therefore the obtained field is not absolute.

2.3 Results

2.3.1 Uncoated vs Coated Fiber WGMR

Effect of coating a thin layer of high index on the electric field $E_z\left(r\right)$ (Equation 2.5) was investigated. Note that total radius of fiber has been kept constant in all the cases unless specified otherwise. WGM mode of 0th radial order (v = 0) in a fiber of refractive index n_{co} = 1.447 and diameter 125 µm coated with a 60 nm layer of $n = n_{co}$ and n = 2.4 are compared in Figure 2.3. For layer index same as fiber's ($n = n_{co}$ = 1.447) WGM field is concentrated well within the fiber with peak occurring at r~61.5 µm, whereas for n higher than n_{co}, the

WGM gravitates toward the high index layer with asymmetric profile reminiscent of a surface wave. This indicates that the high index layer acts like a lower potential well attracting the photonic field.

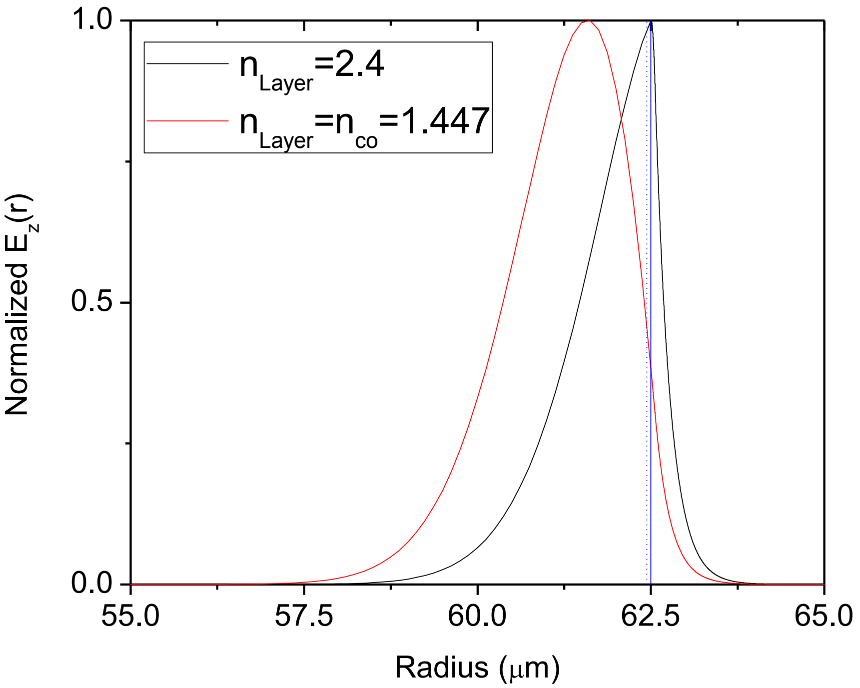

Figure 2.3: Normalized radial profile of WGM in uncoated (red) and coated (black) fiber. WGM gravitates towards the coated layer (60 nm) and is also narrower. Azimuthal order is 400.

2.3.2 Fundamental Mode as a Function of Layer Thickness

This fundamental WGM field as a function of layer thickness is plotted in Figure 2.4. For thickness below 60 nm, mode is concentrated in the low index core (n_{co} = 1.447). As the film thickness increases from 10 nm to 100 nm, the mode field becomes narrower and concentrates closer to the periphery. As thickness increases further, the single peaked mode so far, splits into multiple nodes progressively and shifts into the layer completely becoming a guided mode.

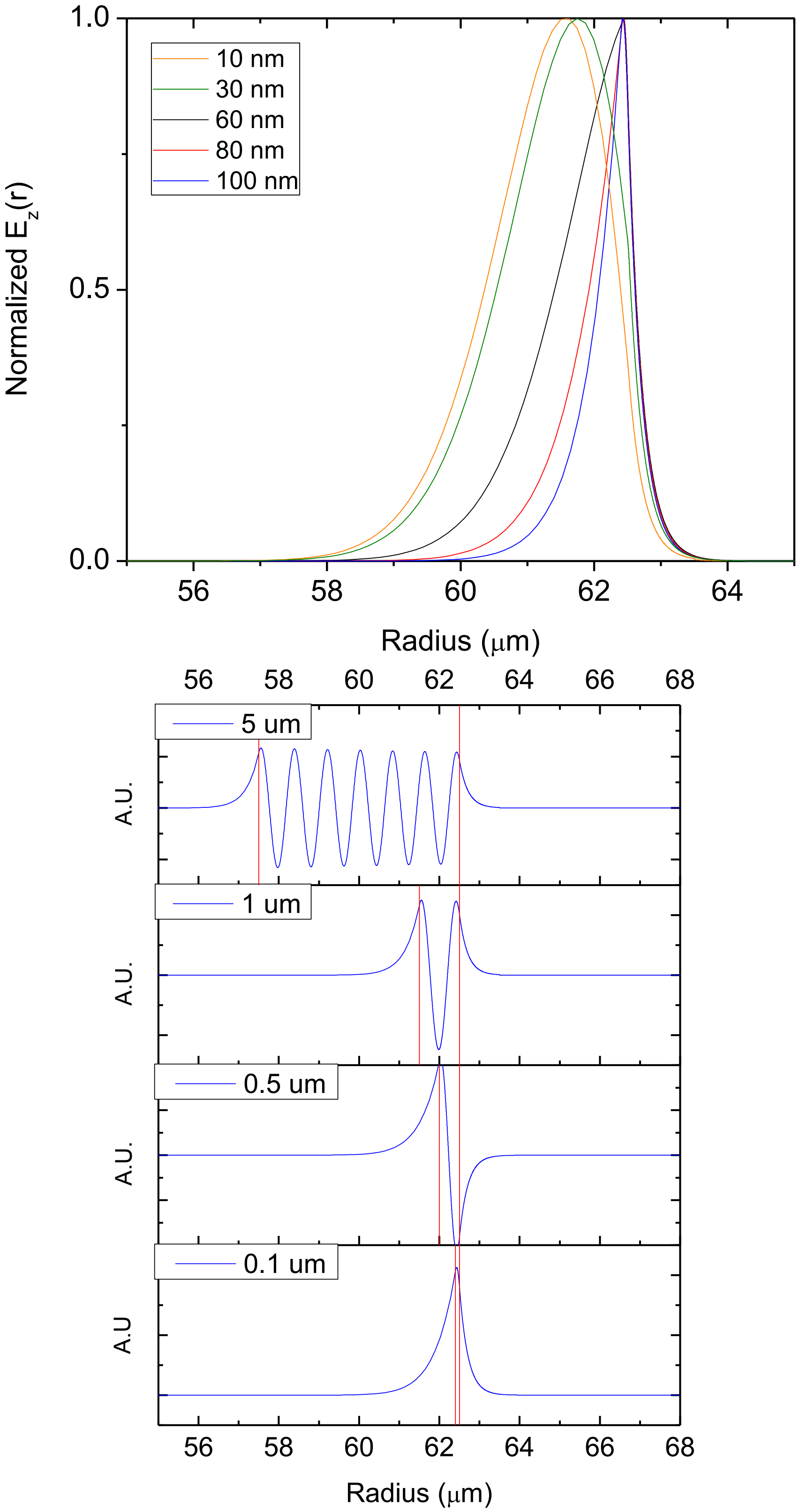

Figure 2.4: Effect of layer thickness on radial field profile of the lowest order WGM. $n_{layer} = 2.4$, $n_{fiber} = 1.447$. Total radius is held at 62.5 μm. $m = 400$.

2.3.3 Higher Order Mode Profiles

2.3.3.1 Subwavelength Layer

First we consider layer thickness less than one wavelength. In Figure 2.5, radial field profiles of higher order modes of SMF coated with 100 nm layer of n = 2.4 are plotted along with fundamental at the bottom. Azimuthal mode order *m* = 400. The field is squeezed narrowly at the location of the high index layer for all orders. For fundamental mode (v=0), the field is concentrated close to the layer whereas peak of higher order modes gradually recedes away from the periphery. As a result, resonant wavelength is shorter with increasing mode order.

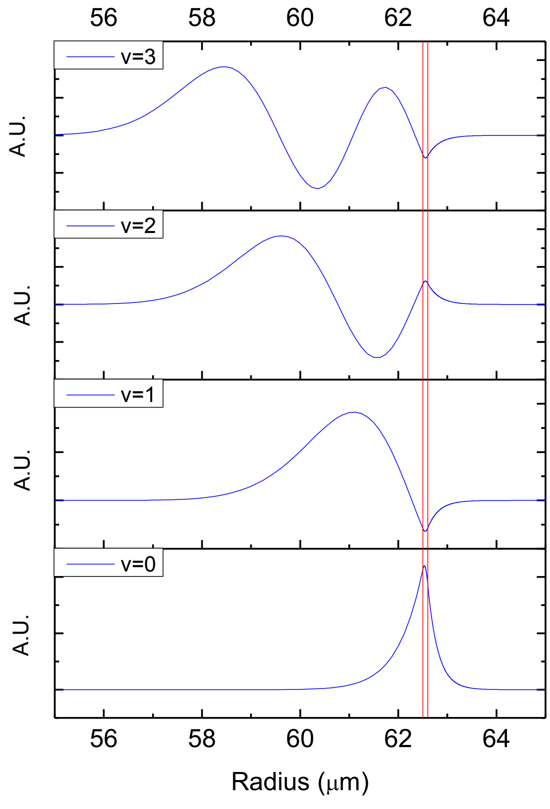

Figure 2.5: Normalized radial E field profile of TM polarized WGM modes of orders v=0 to 3 in an SMF fiber coated with a 100 nm layer of refractive index 2.4. Corresponding resonant wavelengths are: $\lambda_{res} = 1.486, 1.368, 1.335, 1.309\mu m$ respectively.

2.3.3.2 Layer thicker than wavelength

For layer thickness greater than wavelength, the higher order modes profiles look as in Figure 2.6. The fundamental mode is contained within the thick layer as also seen in Figure 2.4, while the higher order modes have energy concentrated in the core instead of the layer. The layer supports only a weak oscillatory field with oscillations increasing with mode order.

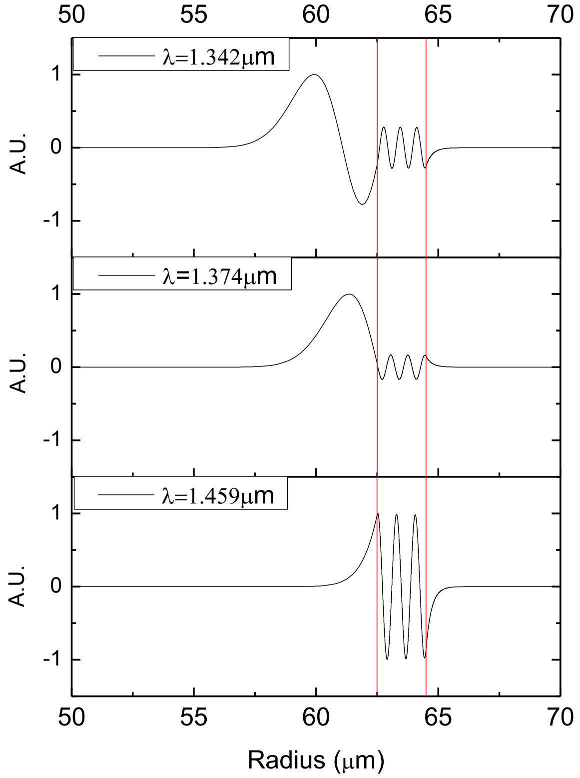

Figure 2.6: Radial E field profile of TM polarized WGM modes of first three modes in a fiber (n=1.447) coated with a layer of thickness 2 μm and refractive index 2.4. The corresponding resonant wavelengths are 1.4586, 1.374, 1.342 μm respectively. $m = 400$.

2.3.4 Effect of Layer Thickness on Fundamental Mode Resonant Wavelength

Next, the effect of layer thickness ($n = 2.4$) is studied on the resonant wavelength (λ_{res}) of fundamental whispering gallery mode existing in the fiber ($n_{co} = 1.447$). As seen in Figure 2.7, dispersion is stronger when the resonator is coated with high index layer (black and red) compared to the uncoated case i.e. when layer index is same as fiber's ($n = n_{co}$ = 1.447) shown with blue and bluish green markers. Within the coated case, fundamental mode (black) is more dispersive than higher order mode (red). Note that for coated 1st order mode, dispersion is strong for thinner high index layers and gradually tends to flatten out with increasing thickness, unlike the case of fundamental (black). For the uncoated case, dispersion is almost flat throughout in contrast. That this increase is indeed due to the structure of the resonator and not solely due to high index is verified by the curve in orange, plotting fundamental resonant wavelength for entire cylinder made of material with n=2.4. This curve is also almost flat indicating the dispersiveness arises due to the coating of high index.

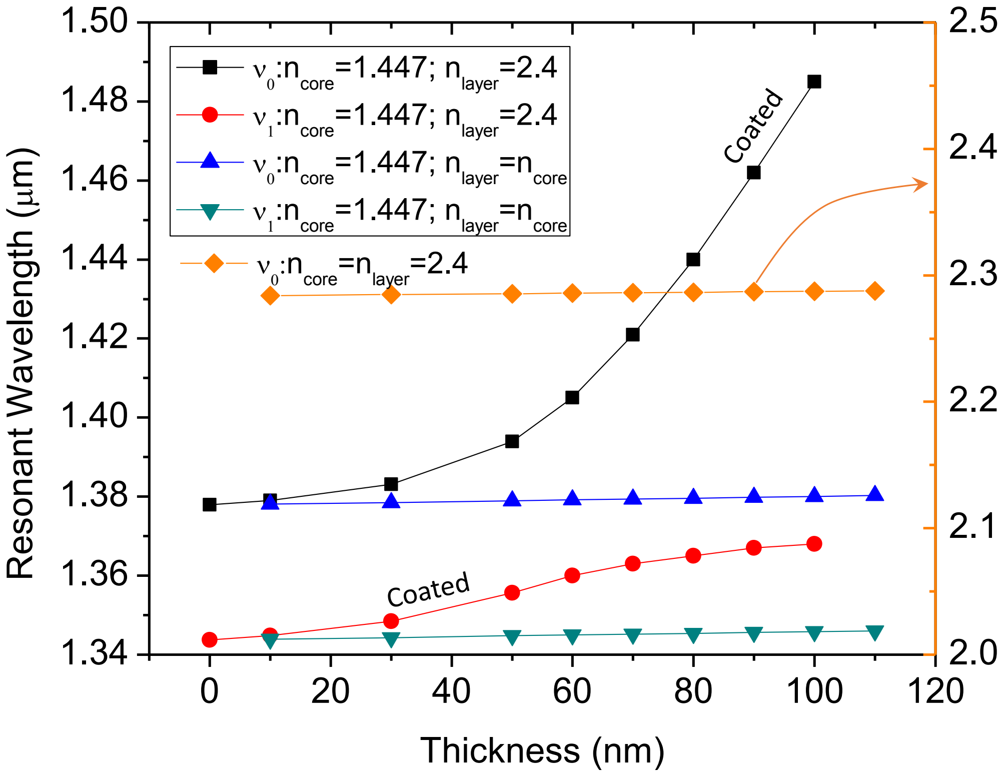

Figure 2.7: Resonant wavelength as a function of layer thickness. Black and red curves are for SMF coated with n=2.4 while blue and bluish green have $n=n_{co}$=1.447. Two curves for each case are for v=0 and v=1. Fiber RI n_{co}=1.447. The orange curve is for $n=n_{co}$=2.4 which has higher resonant wavelength, plotted on the Y axis on the right.

2.3.5 WGM in Three Layer Structure

Finally, WGM modes in a three layer structure are explored. Defect layer is added in the calculation of Section 2.2. Figure 2.8 shows the WGM field in a 3 layer structure as a function of thickness of middle layer separating the sub-micron films. These are TM polarized modes in a fiber-resonator (n=1.45) coated with 3 layers of high (n=1.7) low (n=1.44) high index (n=1.7). Radius of fiber is 62.5 µm, thicknesses of high index layers (t_1 and t_2) are 0.4 µm each while that of separation layer (T) varies from 1 to 10 µm. For smaller separation the mode with single peak of an uncoated fiber is split into two with each centered at the thin layers as if supported by the individual layers. For spacer layer thicker than 5 µm, the mode is confined to the inner layer thus sitting deep inside the cylinder while retaining its sharp radial profile centered at the inner layer. The spacer layer could be used to maintain a fixed coupling gap between fiber-resonator and coupler making it robust in environmental disturbances.

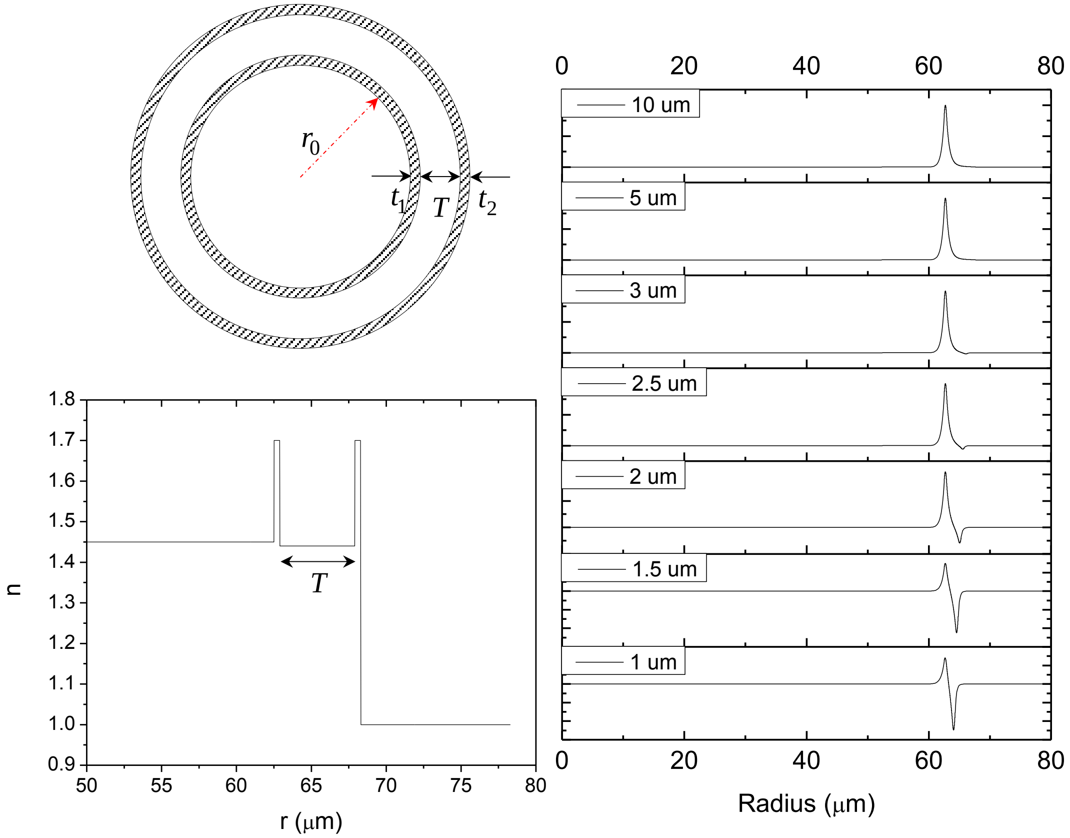

Figure 2.8: WGM mode in 3 layer structure as a function of thickness of separation layer T. Radial E field profile for TM polarized WGM modes in SMF fiber (n=1.45) coated with 3 layers of high (n=1.7) low (n=1.44) high index (n=1.7). Radius of fiber = 62.5 µm, thicknesses of high index layers are 0.4 µm each while that of separation layer varies from 1 µm to 10 µm. Coupling is observed between modes of the thin layers for 2 µm and beyond but the energy shifts to inner thin layer with increasing separation. Modes correspond to lowest order i.e. longest resonant wavelength. Azimuthal order m = 400.

CHAPTER 3 FABRICATION OF COATED FIBERS

3.1 Introduction

The earliest technique explored for fabrication of multilayer fibers with layers of large index contrast was fiber-drawing of preforms of thermo-mechanically compatible materials. In their pioneering work, Hart et al. [16] fabricated a Bragg fiber for mid-IR application by drawing a preform consisting of a polymer core surrounded by alternating layers of As_2Se_3 – a chalcogenide glass (n=2.8) and PES – a polymer (n=1.55). Within two years of this work, Katagiri et al. [17] introduced a new alternative method of fabrication: vapor deposition on a pre-defined core. In this work, a short silica glass fiber was sputter-coated with alternating layers of Si (n=2.5) and SiO_2 (n=1.45) eventually kick-starting research in vapor deposition techniques for fabricating multilayered fibers summarized below.

3.1.1 Overview of Vapor Deposition Methods Used for Multilayered Fibers

RF Sputtering: Sputtering is a Physical Vapor Deposition method in which a target is bombarded with high energy ions provided by a plasma to eject particles from the target which in turn get deposited on the object to be coated. Such deposition being directional, makes it non-trivial to sputter-coat a fiber uniformly. Therefore Katagiri had to employ multiple sputtering guns to achieve uniformity around the fiber [17]. Moreover separate chambers had to be used for each material species to avoid cross contamination. From the viewpoint of controllable refractive index, important for fabricating desired index-profiles, this method is not convenient due to limited control parameters such as buffer gas pressure and temperature. Change refractive index using a different material is also cumbersome as evident from [17].

LPCVD: Low Pressure Chemical Vapor Deposition [18] or LPCVD is based on chemical reactions between radicals produced thermally in the deposition chamber held at low pressure. The low pressure is necessary to prevent unwanted gas-phase reactions which is also responsible for extremely slow growth of the films (few tens of Angstrom per min). Thin films with ideal stoichiometry can be deposited from proper mixture of precursor molecules and can achieve good conformal coverage. This process, however, requires high processing temperature around 600° Celsius and above, depending on film species and precursors, which limits itself to materials that can sustain very high temperature. An attempt in this direction was made by Hadley et al. [19] who fabricated wafer scale Bragg fiber using Si and SiO_2 while their similar work on Si/Si_3N_4 Bragg Fiber remained unpublished. In another work [18], multilayers of isotropic and anisotropic Boron Nitride were deposited on a silicon Carbide fiber passing through an LPCVD system utilizing temperature gradient in the chamber.

HPCVD: High Pressure CVD uses gas pressures on the order of 10s of MPa increasing the rate of chemical reactions. Chaudhuri et al. [20] reported fabrication of hollow core Bragg fibers by depositing alternate layers of Crystalline Si ($n=3.48$ at $\lambda=1.55$ μm) and SiO_2 ($n=1.44$ at $\lambda=1.55$ μm) in a hollow core fiber. Crystalline Si was achieved by annealing of amorphous Si layer deposited at 480° C. SiO_2 layers were produced by partial oxidation of Si layer at 850° C.

The other popular thin-film deposition method – plasma-enhanced chemical vapor deposition (PECVD) – employs plasma to significantly reduce process temperature and increased deposition rates. For instance, thin films of silicon nitride can be deposited at temperatures as low as 250° Celsius. This opens up possibilities to fabricate multilayer fibers that incorporate temperature sensitive materials such as chalcogenide and phosphate glass, both of which are important classes of optical materials. This dissertation work is dedicated to adapting PECVD for fabricating multilayered fibers.

3.1.2 PECVD for wafers: General Principle and Chemical reactions

Principle: As opposed to CVD, which relies on thermal energy to initiate chemical reactions, PECVD relies on high energy electrons in the plasma to rip off the bonds to create radicals. Electrons being much lighter than ions have much higher temperature while ions in the bulk remain at low temp due to poor energy transfer from e^- to ion by collision. The reactions that need high temperature, can now occur at lower temperature as the plasma provides part of the required energy. The deposition rate is also high owing to the plasma, compared to LPCVD. Hence the name Plasma Enhanced CVD.

Mechanism: In PECVD, the plasma is generated between a pair of electrodes in the popular parallel plate reactor design used in this work. The general schematic of the chamber is given in Figure 3.1. High frequency RF (13.56 MHz) generator is connected to the top electrode, designed as a showerhead for uniform gas distribution, while the bottom one (base platen) is grounded and held at 350^o C. The top electrode is about 60^0 colder creating a temperature gradient between the electrodes. The substrate wafer is placed on the hot base platen. A rotary pump connected to the chamber, creates a vacuum of about 1mTorr and reacting gases are introduced into the chamber. The RF generator creates the plasma from the gases. There is thin region of potential drop between plasma and objects it is in contact with. Being at higher potential than the substrate, the ions get accelerated downward and adsorbed onto the substrate. The plasma facilitates in creating more reacting species on the hot surface of the substrate and the ions migrate on the surface to form clusters which build up with time into a non-stoichiometric solid film. Volatile by-products formed during the surface reactions get desorbed and pumped out of the chamber.

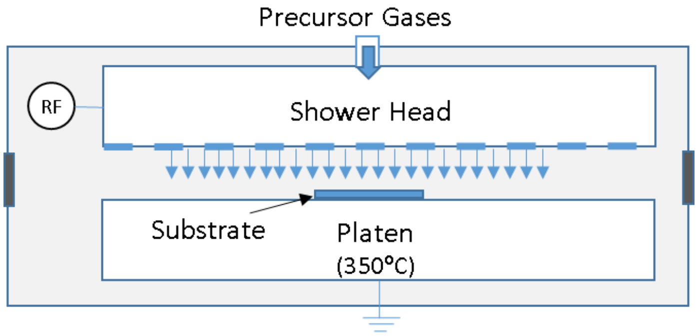

Figure 3.1: Schematic of PECVD chamber

Uniformity of reactant flux dictates the deposition uniformity on the substrate, which in turn depends on electric field distribution in the chamber. Due to concentration of ions on the edges of substrate, the E field varies near the edges leading to non-uniform deposition on peripheries.

<u>Chemical reactions</u>: The materials used for fabricating Bragg layers in this work are silicon nitride and silica. The gas used as the source of silicon is 2% silane (SiH_4) diluted in nitrogen - an inert carrier gas. Dilution in inert gases allows to increase power density of plasma (hence high deposition rate) without SiH_x powder formation that happens with pure silane [21]. For deposition of silica, N_2O gas was employed which releases N_2 and H_2 as byproducts.

$$SiH_x + N_2O \longrightarrow SiO_x + N_2\uparrow + H_2\uparrow$$

For the deposition of silicon nitride, NH_3 is used as the source of N, releasing H_2 and leaving a solid film of non-stoichiometric silicon sitride (SiN_x) with some hydrogen content.

$$SiH_x + NH_x \longrightarrow SiN_x + H_2\uparrow$$

Even though N_2 can also be used in place of NH_3 for less H content, but the high bond energy of N_2 leads to silicon rich films. From the point of view of optical losses, one may argue in support of Ammonia free recipe for SiN_x. For consistency with previous work [22], the recipes used in this dissertation were the same as those provided by the PECVD tool manufacturer and no changes to any parameter were made.

3.2 Experiment

3.2.1 PECVD Adapted for Coating Optical Fibers

The challenge with PECVD for coating optical fibers is the directional deposition unsuitable for azimuthally uniform coatings, as experienced by Michalak et al. [23] and Dr. Her’s group [22] before this work. The deposited layer around the fiber is thicker at the top due to high reactant flux and gradually thins down at the bottom (Figure 3.2). To overcome this challenge, the fiber was rotated continuously during deposition.

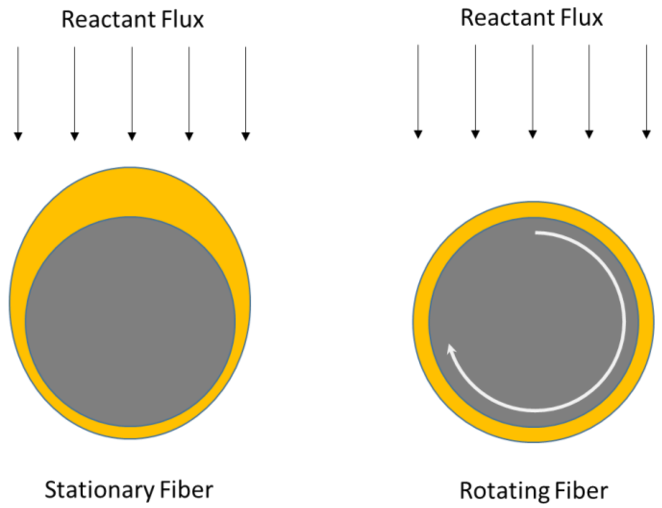

Figure 3.2: (a) Stationary fiber has non-uniform deposition due to high flux at the top. (b) Rotating the fiber equalizes the flux exposure creating uniform film

To enable rotation of the fiber about its axis, we adapted the commercial RF-PECVD unit (STS Multiplex Pro CVD MP0565) available in the cleanroom. Figure 3.3 (a) shows the schematic of the deposition chamber with the modifications. A rotary feedthrough driven by a stepper motor controlled via Arduino UNO is attached to a view port on the chamber wall (b). The rotation speed of the feedthrough is set at 30 rpm with a potentiometer in the motor driver circuit. The rotary shaft holds a fiber chuck parallel to the base platen (c), which holds the fiber approximately 4 mm above the platen. The other end of the fiber rests in a holder sitting diametrically opposite to keep long fibers from sagging. Precursor gases entering the chamber from the top are pre-mixed and a purple-pink plasma is created. The reacting species are directed downward onto the fiber.

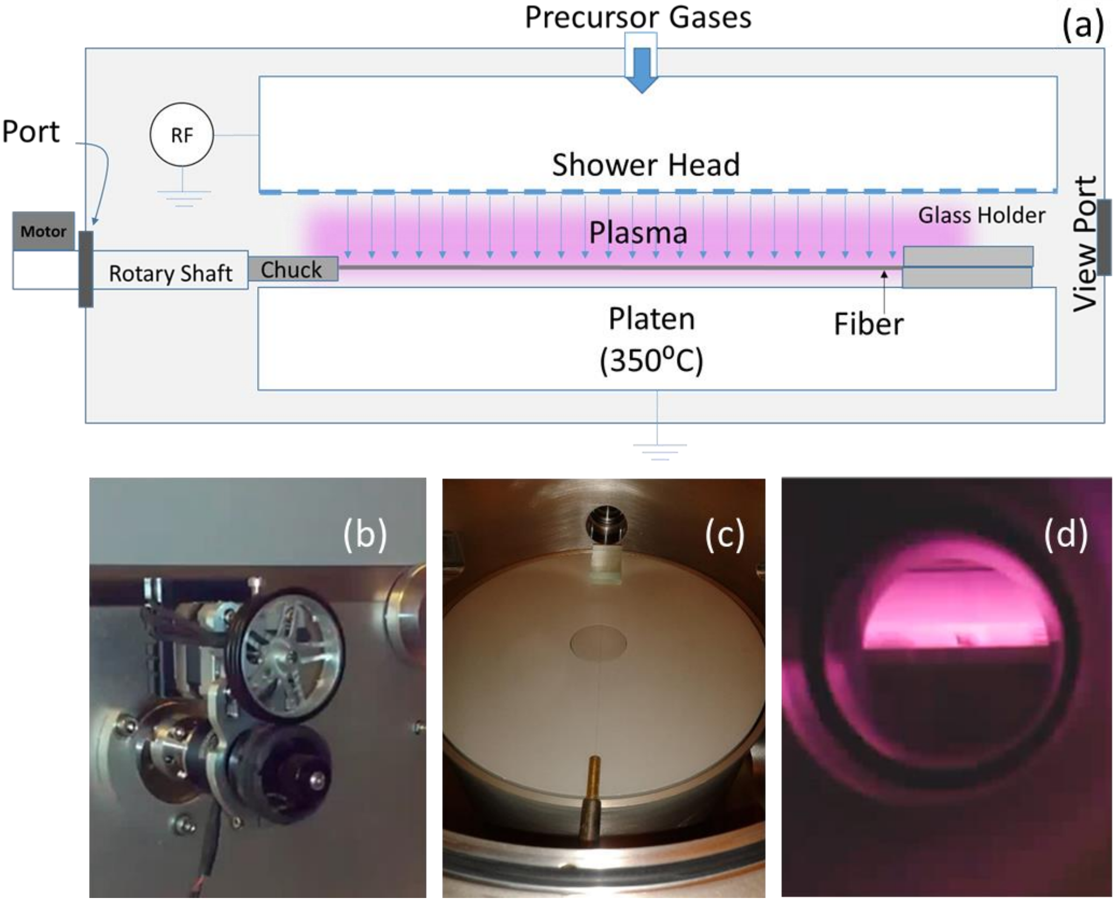

Figure 3.3: (a) Schematic of PECVD chamber modified for deposition on fiber. (b) Outside view of the rotary feedthrough with a stepper motor attached overhead. (c) Inside view of the chamber showing the circular base platen with glass holder on the extreme end and Brass fiber chuck diametrically opposite. Faintly visible fiber is held by the chuck and the glass holder. View from the circular viewport on the side of holder can be seen in (d) showing the pink plasma between the platen and showerhead.

Note that the fiber is not in contact with the base platen and hence is at a temperature less than 350° C which is expected to alter the growth kinetics.

3.2.2 Fabrication Procedure

Substrate Preparation: We used two types of fibers as substrate for deposition: one is Corning SMF28 (jacket stripped, outer diameter = 125 µm) and the other is Thorlabs FT200EMT (cladding stripped, core diameter = 200 µm). Since the chamber is small, we use a 9-10 inch long segment of the fiber. To prepare Thorlabs fiber, its jacket is stripped and the thin polymer cladding wiped away by hand to expose the 200 µm multimode fiber core, while to coat SMF28, only jacket is stripped and fiber is wiped to obtain 125 µm cladding with small embedded core. The stripped fiber is slid into a in a tube of <5 mm inner diameter. The tube is filled with cleaning agent, sealed at both ends and placed in a sonicator. Acetone is used for initial thorough cleaning of any oily deposits and remaining polymer, followed by gentler IPA and then DI water, for 2 mins each. The fiber is allowed to dry to load into the chamber.

Loading: The cleaned fiber is slid all the way into a fiber chuck to provide enough friction between fiber and chuck. A metal sleeve for the chuck is secured tightly in the slit making sure it is in contact with the fiber to prevent fiber from slipping out or not rotate in sync with motor during deposition. For SMF28, it is necessary to insert an additional metal shim to secure the fiber well enough for the rough conditions in the chamber. Remember the fiber will shake during deposition.

Before opening the chamber vented to atmosphere, the port in the side wall of the chamber is opened to install the rotary feedthrough just above the base platen, to minimize contamination by prolonged exposure. The chamber lid is opened and fiber holder is placed on the platen. Then the chuck loaded with fiber is slipped into the rotary shaft while the other end of fiber sits in the holder. Vacuum grease can be applied on the portion of chuck inside the shaft once between several runs for a good grip. Thickness of the glass holder is chosen according to the height of the fiber in the chamber which is about 4 mm. Another glass piece is placed over this holder to secure the fiber in the groove. For thicker fibers a simple support may also work. About an inch long groove is sufficient to prevent the SMF28 from sagging across the 8” diameter of platen, whereas a simple metal sheet with a slot cut in it worked for Thorlabs FT200EMT. The chamber is closed and pumped down.

Speed setting: Speed of the rotary shaft is adjusted to the desired value with a potentiometer on the motor driver board.

Deposition: The desired deposition recipe is started. The gas flow rates for SiN_x growth are 1980 and 55 sccm for SiH_4 and NH_3 respectively, while for silica growth, flow rates are 400 and 1420 sccm respectively for SiH_4 and N_2O. These numbers and all other process parameters such as RF power etc. were provided by STS. Desired sequence of layers are deposited, as the fiber rotates about its axis continuously until the recipe is over.

Unloading: The chamber is vented to atmosphere and the lid of the chamber is opened to unload the coated fiber. The deposition on the chuck is cleaned after every use to prevent contamination of the PECVD system during purge.

For details on PECVD operating instructions, see APPENDIX B.

3.3 Results

3.3.1 Single-Layered Optical Fibers

Single layers of silicon nitride were coated on FT200EMT (core diameter = 200 µm) with increasing deposition times given in Figure 3.4. All fibers were coated at 30 rpm.

The fiber with shortest deposition time looks almost transparent whereas the rest of the fibers have a well-defined hue going from brown to bluish green to green to yellowish green to orangish green.

Another set of single layered fibers coated with SiN_x was prepared using Corning SMF28. Images taken under Olympus microscope are shown in Figure 3.5. Note that the hue of the fibers changes from violet to green to yellow for increasing layer thickness as a result of thin film interference. However this raises the question why ZN9 and ZN19 have different color when the deposition times are almost similar. The difference between these fibers is that fiber substrate is different, deposition time is not identical and these were fabricated two years apart. The difference may be due to position of observation point away from the center of chamber.

Not surprisingly, the fibers coated with SiO_2 did not exhibit such colors (Figure 3.6) due to small index contrast between the fiber and PECVD deposited SiO_2 film.

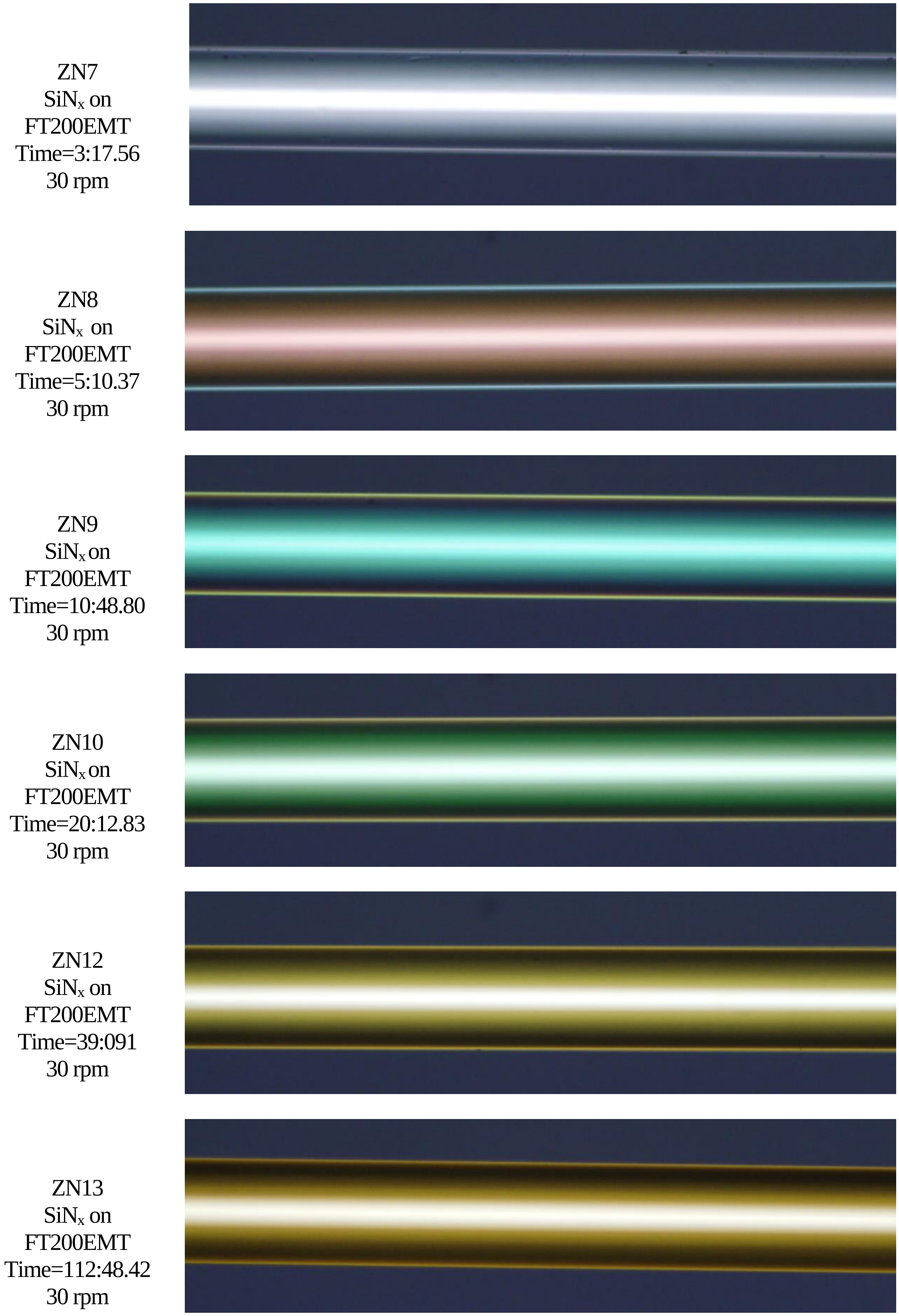

ZN7
SiN_x on
FT200EMT
Time=3:17.56
30 rpm

ZN8
SiN_x on
FT200EMT
Time=5:10.37
30 rpm

ZN9
SiN_x on
FT200EMT
Time=10:48.80
30 rpm

ZN10
SiN_x on
FT200EMT
Time=20:12.83
30 rpm

ZN12
SiN_x on
FT200EMT
Time=39:091
30 rpm

ZN13
SiN_x on
FT200EMT
Time=112:48.42
30 rpm

Figure 3.4: Bright field images of Thorlabs fiber FT200EMT coated with SiN_x for progressively increasing deposition times.

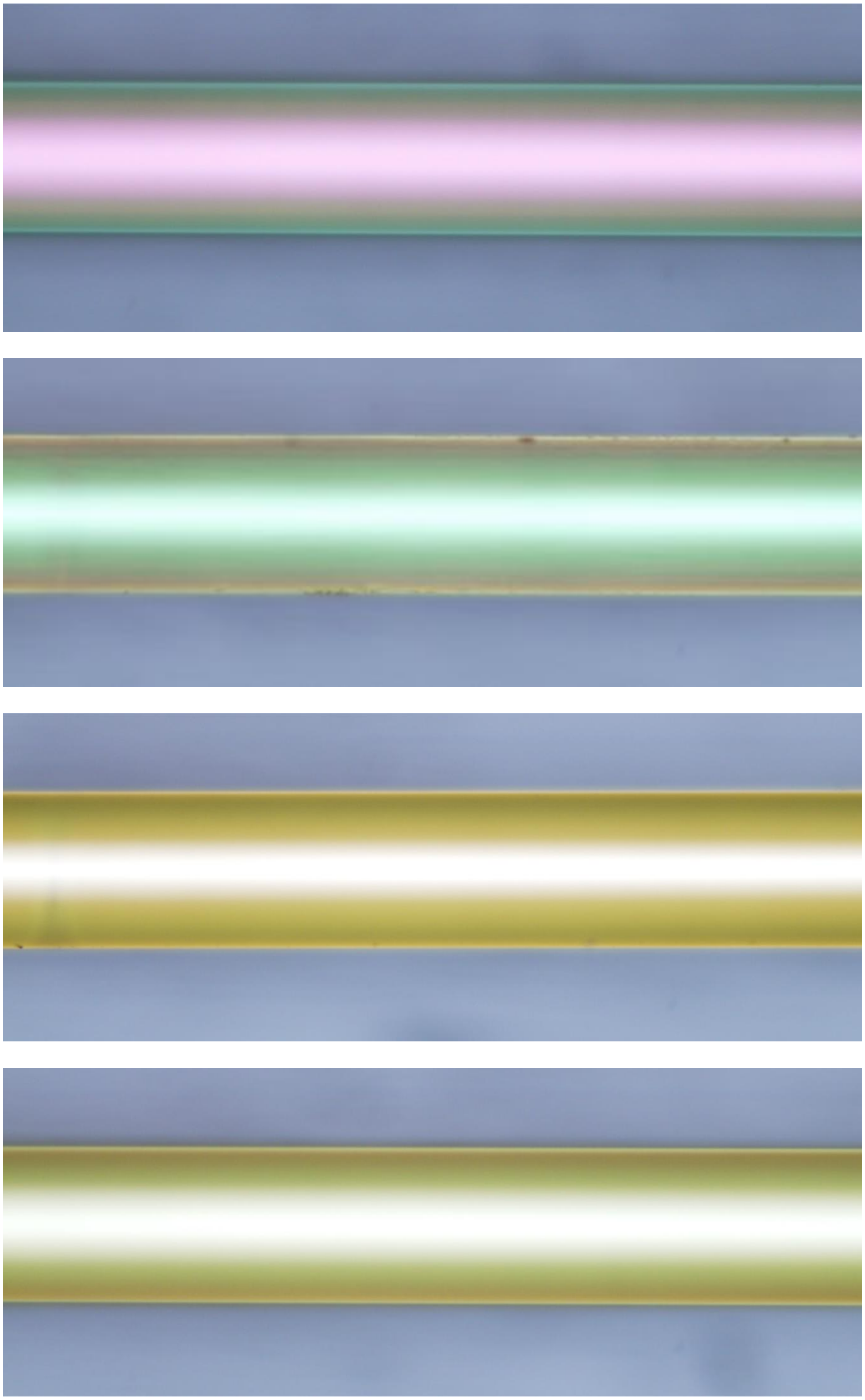

ZN19
SiN_x on
SMF28e+
Time=10:00
30 rpm

ZN17
SiN_x on
SMF28
Time=21:00
30 rpm

ZN20
SiN_x on
SMF28e+
Time=30:00
30 rpm

ZN21
SiN_x on
SMF28e+
Time=40:00
30 rpm

Figure 3.5: Bright field images of Corning SMF28 coated with SiN_x with increasing deposition times.

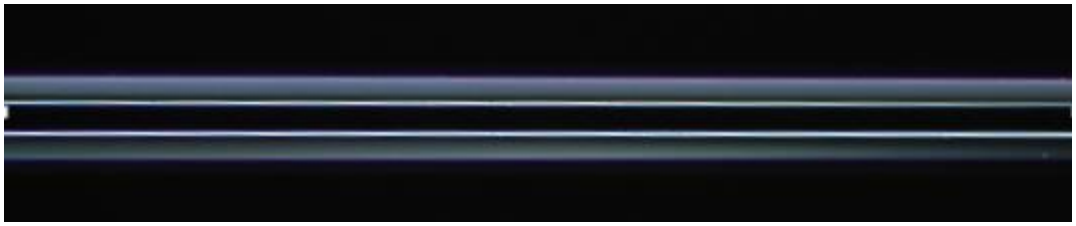

ZN18: SiO_2 on SMF28e+ | Deposition Time=5:00 | 30 rpm

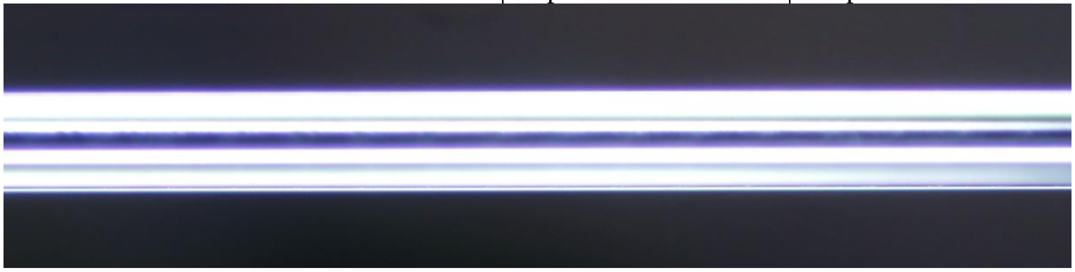

Dark Field: Uncoated SMF28e+

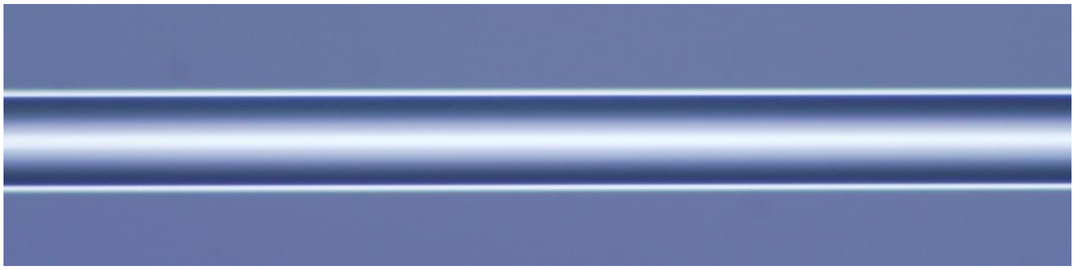

Bright Field: Uncoated SMF28e+

Figure 3.6: Dark field image of Corning SMF28e+ coated with SiO_2 for 5 mins at 30 rpm (top) and uncoated SMF28e+ (middle and bottom).

3.3.2 Multilayered Optical Fibers

Alternate layers of SiN_x and SiO_2 were deposited to form Bragg fibers ZN4, ZN5 and ZN27. ZN4 and ZN5 were made by depositing 12 pairs of SiN_x and SiO_2 on FT200EMT terminating the stack in a thick layer of SiO_2 deposited for 5 minutes. While ZN27 was made with SMF28e+ with only 4 pairs and no thick terminal layer. Optical microscope images of these fibers along with the deposition times can be seen in Figure 3.7. ZN4 and ZN5 have yellowish and orangish brown hue respectively unlike ZN27 which is green.

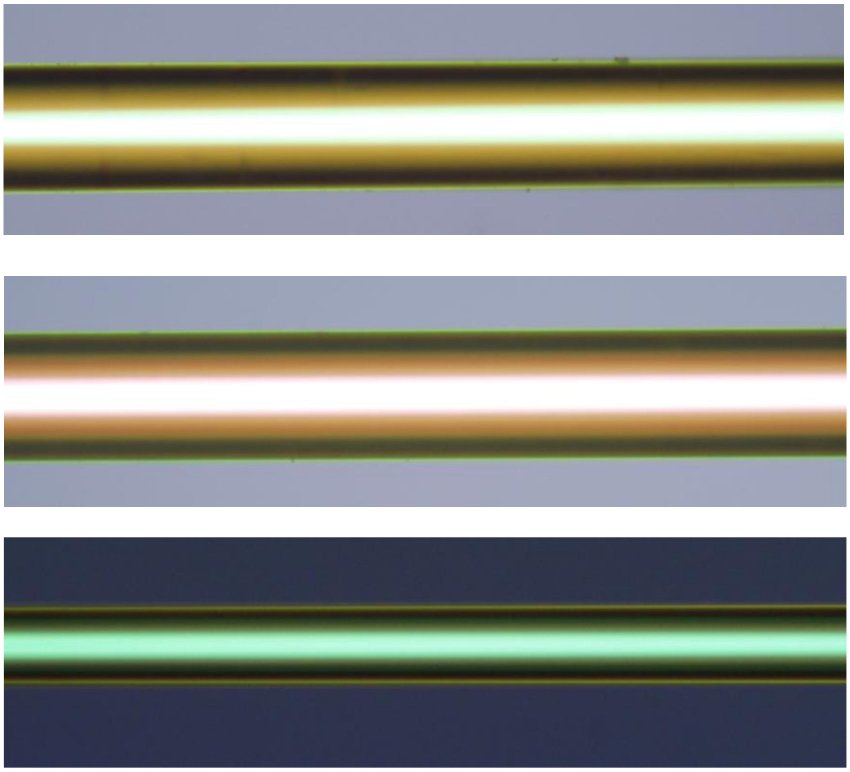

(a)

ZN4:
$(SiN_x/SiO_2)^{12}(SiO_2)$
$(11:2.3/36.9)^{12}/(5:00)$
FT200EMT

(b)

ZN5: $(SiN_x/SiO_2)^{12}(SiO_2)$
$(8:19.7/1:49.3)^{12}/(5:00)$
FT200EMT

(c)

ZN27: $(SiN_x/SiO_2)^4$
$(10:00/36.00)^4$
SMF28e+

Figure 3.7: Bright field images of Bragg Fibers fabricated in PECVD. (a) ZN4 has 12 pairs of SiN_x and SiO_2 terminated with thick layer of SiO_2 deposited for 5 mins. (b) ZN5 also has 12 pairs of SiN_x and SiO_2 but with different deposition time, and terminated in a 5 min SiO_2 layer. (c) ZN27 has 4 such pairs with deposition time of 10 mins for SiN_x and 36 sec for SiO_2. (Deposition Time format - mm:ss.ss)

The cross section of an end polished Bragg fiber shows a bright ring in Figure 3.8. The core diameter is 200 µm. SEM image of the Bragg layers of ZN4 in Figure 3.9 show the multilayered structure in detail. The substrate fiber lies on the extreme left followed by the 12 pairs of SiN_x and SiO_2 terminating in about 1 µm thick silica layer. To prepare the fiber for SEM, the coated fiber was cleaved at one end and exposed to a 3 molar KOH solution for 5 hours. The KOH dissolves SiO_2 faster than SiN_x [24] creating a difference in depth between layers that allows the SEM to differentiate between different materials.

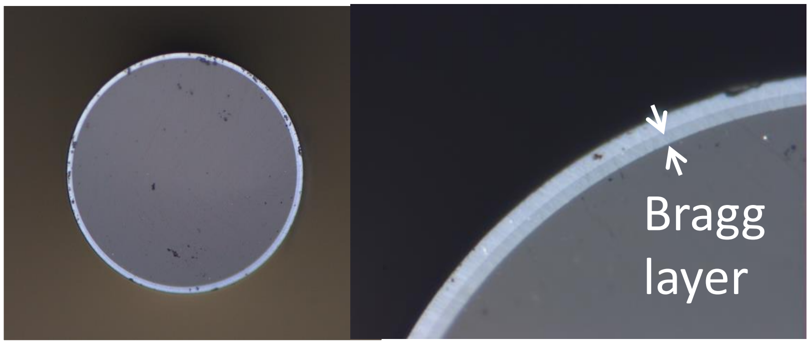

Figure 3.8: Optical microscope image of cross section of Bragg fiber with 200 µm core. Outer bright ring consists of the Bragg layers terminated by thick SiO_2 layer.

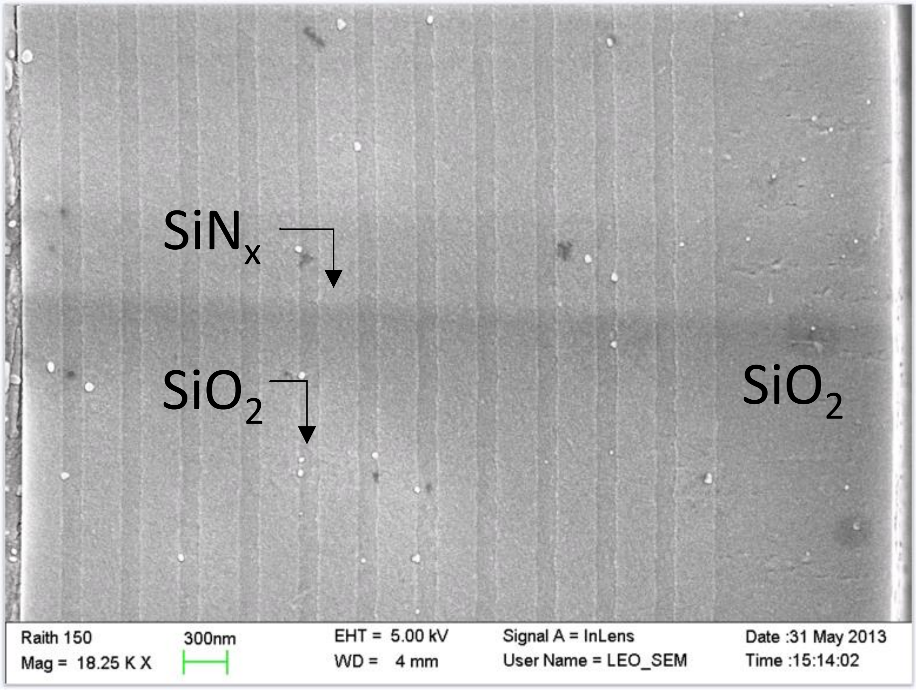

Figure 3.9: SEM image of Bragg layers of ZN4. Left to right: Substrate fiber, 12 pairs of SiN_x/SiO_2, terminal layer of SiO_2.

3.3.3 Uniformity of Layers

Axial Uniformity: The fibers coated with SiN_x show rapidly changing color on fiber ends (Figure 3.10) due to edge effects suggesting a gradient in thickness. The color becomes constant over the fiber region located at the center of the chamber during deposition. This can be seen in Figure 3.11 showing images of ZN9 taken along its axis. Rapidly changing color near the fiber end (a) transitions to purple-pink (b) which transitions to bluish green (c) and remains so over a long length near the center finally becoming yellowish green (d). Depositing too thick of a film such as 3 µm, develops cracks on frequent handling (Figure 3.12). Therefore it is important to check for cracks in Bragg fibers before examining them. Submicron films are easier to handle and have been used for characterization of films in Chapter 4.

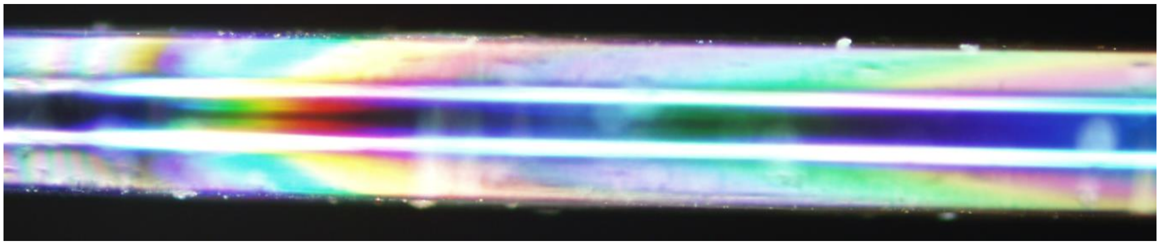

Figure 3.10: Non-uniform deposition near the fiber end

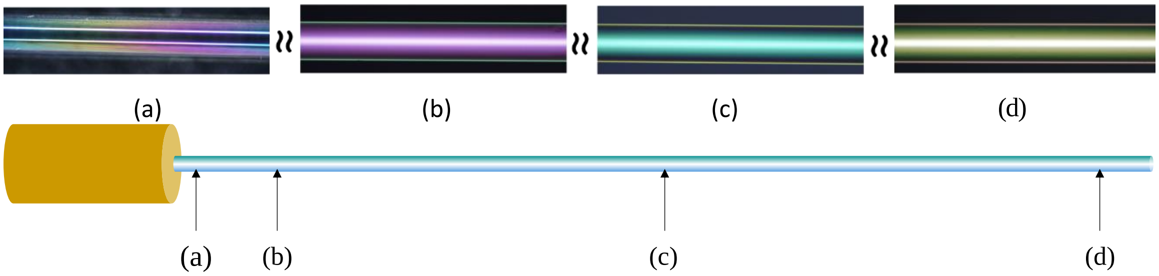

Figure 3.11: Optical images of ZN9 taken along fiber axis.

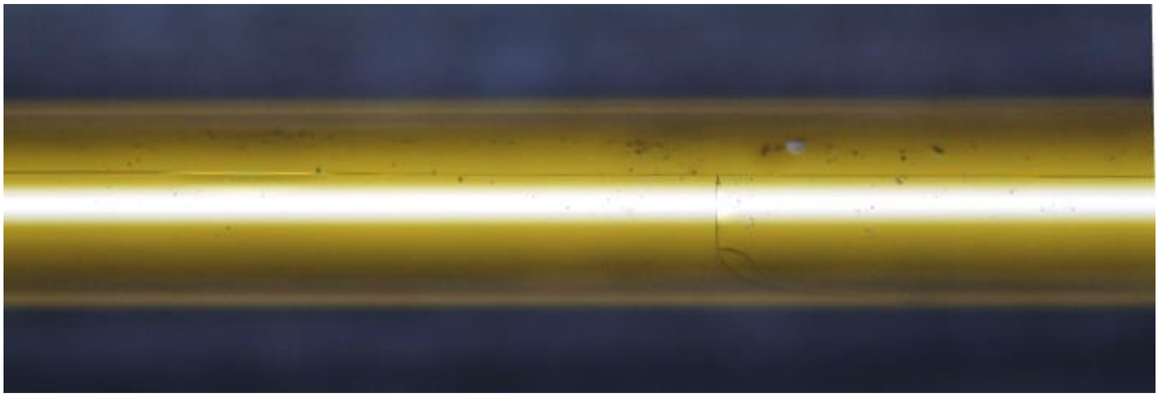

Figure 3.12: Crack in thickest layer coated (~ 3 um): ZN13. Thick layers are prone to crack on frequent handling.

Azimuthal Uniformity: To assess the azimuthal uniformity qualitatively, ZN4 was imaged in steps of 45 degrees under microscope (Figure 3.13). The hue of the fiber remains the same over 360 degrees indicating good azimuthal uniformity of layers. For a comparison, images of a Bragg fiber prepared without rotation in previous work [25] are also shown. The coating thickness varies dramatically around the fiber when kept stationary during deposition. For quantitative comparison between stationary and rotated case, SEM was performed by first treating the layers with KOH to distinguish between the SiN_x and SiO_2 layers. The measured thicknesses plotted with respect to azimuthal angle in Figure 3.14 show 9% variation about the mean thickness for stationary case in contrast to flat curve of rotated fiber.

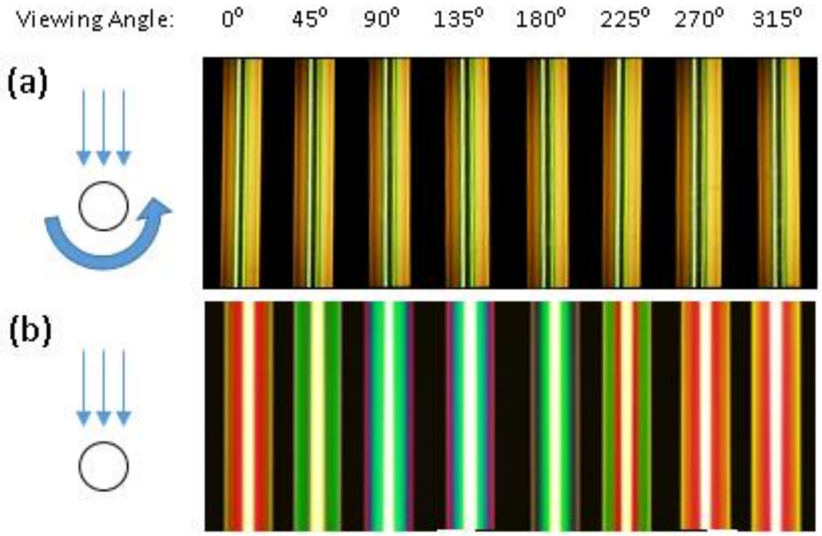

Figure 3.13: Comparison of iridescence of Bragg fiber fabricated by rotation (ZN4) (a) and without rotation (b).

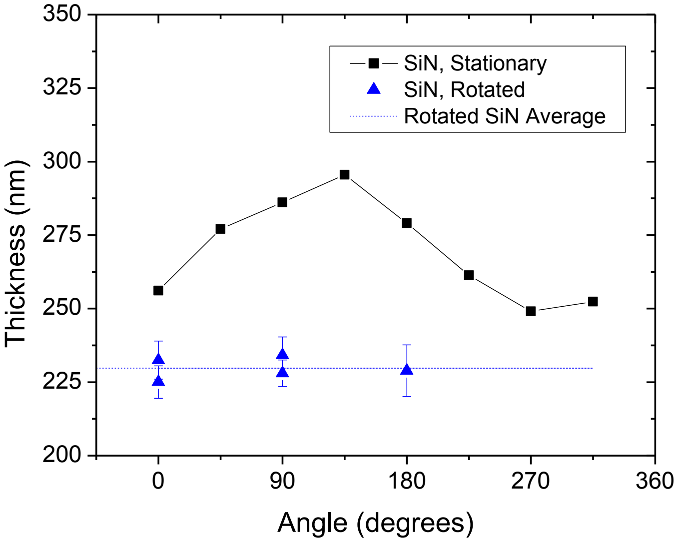

Figure 3.14: A comparison of thickness variation azimuthally for stationary (black squares connected by straight line as eye guide) and rotated (blue triangles) case. Blue dashed marks the mean value of thickness.

3.3.4 Coated NIST's Microrod Resonator

Other than fibers, microrod resonator [26] carved on a fused silica rod 2 mm in diameter by CO_2 laser machining at NIST, was also coated in the modified PECVD tool. We received about a cm long rod with the resonator carved at the center. To coat this in

PECVD chamber, the resonator rod was attached to a long glass rod (Figure 3.15) so that the resonator is located at the center of the chamber during deposition.

Figure 3.15: The short resonator rod attached to a long 2mm diameter glass rod with a ceramic sleeve. Metal shim was used to fill the gap between sleeve and the 2 glass rods.

The samples received from NIST seemed to have particles from ablation left on the sides of the small ablated region that forms the resonator, giving a hazy appearance (Figure 3.16 (a)) falling off away from the ablated areas. When subjected to conditions in a PECVD chamber for deposition of SiN_x, these particles agglomerated into a white powder (b). The resonator was free from such whiteness as it was annealed during machining, which would mean no such dust left over. However, while handling this sample with flaky powder, some flakes could fall on the resonator. Therefore we tried cleaning it before deposition. The sample #3 was cleaned using Acetone/Isopropanol/DI water (c) before coating. As expected, there was no whiteness on this cleaned resonator (d). This confirms the existence of very fine SiO_2 particles on the pedestal region. We hypothesize that this is caused by rapid cooling of evaporated SiO_2 when it expands into cooler air during CO_2 machining.

The coated microresonator was shipped back to NIST. The collaborators measured a Q factor of 2.2×10^6 for λ=1.55 μm indicating a good film quality.

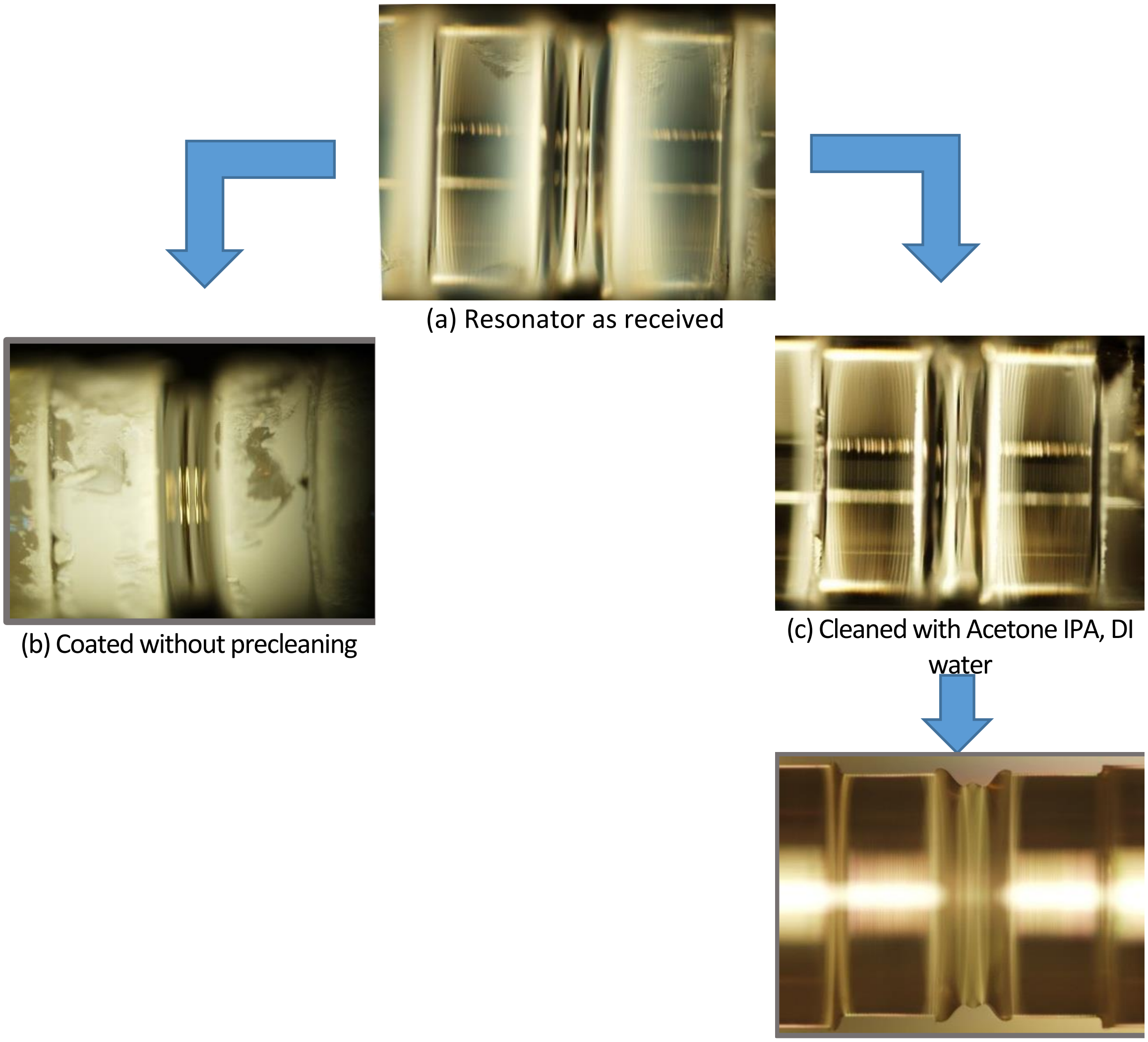

(a) Resonator as received

(b) Coated without precleaning

(c) Cleaned with Acetone IPA, DI water

(d) Coated with SiN_x

Figure 3.16: Microrod resonators received from NIST have a milky appearance (a). When coated without cleaning, the milky appearance turns into white debris (b) while the resonator region remains clean. But if the resonator is cleaned (c), the milky appearance vanishes and the coated resonator is free of any debris (d).

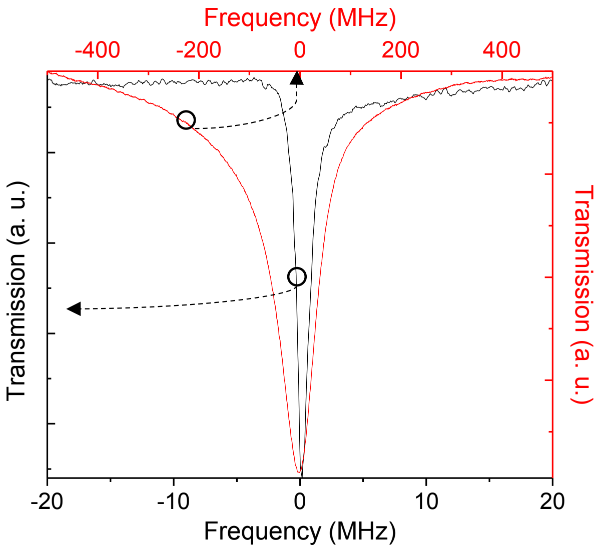

Figure 3.17: Resonance dip in the transmission spectrum of coated microrod resonator has a linewidth of 90 MHz and Q-factor 2.2x10^6 (red). The dip for uncoated resonator (black) is shown for comparison. It has about 1 MHz linewidth. (Image credit: Pascal Del'Haye at NIST Boulder, now at NPL - UK)

CHAPTER 4 CHARACTERIZATION OF THIN FILMS ON OPTICAL FIBERS

4.1 Introduction

The standard method to characterize thickness and refractive index of thin films is ellipsometry. But performing ellipsometry on highly curved surfaces such as an optical fiber with good resolution is challenging with conventional ellipsometers. Devices with high lateral resolution about 10 µm and high accuracy of measurement have been reported in literature. However most of them are "state-of-the-art" rather than commercial devices. Micro-ellipsometers designed to examine samples with flat surface could be used for curved surfaces, if the lateral resolution is high enough allowing a part of the cylindrical surface to be considered as planar. Some micro-ellipsometers are developed to measure optical parameters of rough or curved surfaces but the output optical signal is difficult to interpret. Moreover it would need correct model to perform ellipsometric measurement even if an appropriate ellipsometric device is at our disposal. Imaging ellipsometers, on the other hand, have a higher resolution (1 - 10 um)[27, 28]. The highest lateral resolution of 1 µm available in a commercial device [27], may suffice for measuring film thickness on an optical fiber but the light reflected from the bottom side of the fiber could pose a challenge. Efforts are still ongoing to make an imaging ellipsometer for curved surfaces [29] and several problems have been acknowledged in interpreting the measurement data.

In this chapter, another technique is explored for measurement of film RI and thickness. The coated fiber is treated as a scatterer and its scattering signature is analyzed at a given wavelength to extract the thin film properties. The motivation comes from the fact that Mie scattering of a particle is sensitive to its geometrical and optical properties and has been used extensively for decades to characterize various scatterers, spinning off several applications including characterization of optical fibers. Presby in his pioneering work [30] applied scattering from a fiber to determine its diameter and refractive index. His work was followed by some others related to core-shell systems such as polymer coated fibers, tapered fibers [31]. However none of these shells can be considered as a thin film. In this chapter, scattering signatures of the coated fibers presented in Chapter 3 are used to determine refractive index and thickness of the films. Section 4.2 is an overview of the theory of light scattering from concentric cylinders, followed by experiment and data presented in Section 4.3 and 4.4. Data analysis along with results are presented in Section 4.5 where the encountered challenges and alternatives have been presented.

4.2 Theory of Scattering from Layered Fibers

The theory of light scattering from multilayered cylinders was first proposed by Kerker [32]. A concise review of the theory starting from wave equation up to the scattering intensity is presented in this section. We begin by identifying the orthonormal set of vector functions that are solutions to the vector wave equation. These are generated by a scalar function that satisfies scalar wave equation and a pilot unit vector. Any solution to the vector wave equation can be expressed as a linear combination of these vector functions. Thus $\vec{E}$ and $\vec{H}$ are expressed as a combination this basis set in cylindrical coordinates, which satisfy Maxwell's equations. Next, the boundary conditions are derived. To derive the scattering intensity, all we need is to construct the scalar function in each layer that generates the field. We begin with the vector wave equation,

$$\nabla^2 \vec{A} + n^2 k^2 \vec{A} = 0 \,. \tag{4.1}$$

It is easy to verify that if ψ is a solution of the scalar wave equation $\nabla^2 \psi + n^2 k^2 \psi = 0$, and $\vec{a}$ is a constant unit vector, then the following three vector functions satisfy Equation

4.1:

$$\begin{aligned} \vec{L} &= \nabla \psi \\ \vec{M} &= \nabla \times \psi \vec{a} \\ \vec{N} &= \frac{\left(\nabla \times \vec{M}\right)}{nk} \end{aligned} \tag{4.2}$$

Below is a quick proof that M satisfies Equation 4.1. Substituting $\vec{M}$ into Equation 4.1, we get

$$\nabla^2 \vec{M} + n^2 k^2 \vec{M} = \nabla^2 \left[\nabla \times \psi \vec{a}\right] + n^2 k^2 \left[\nabla \times \psi \vec{a}\right] \ . \tag{4.3}$$

Using the identity $\nabla^2 \left(\nabla \times \vec{A}\right) = \nabla \times \nabla^2 \vec{A}$, RHS of Equation 4.3 becomes

$$\nabla \times \nabla^2 \psi \vec{a} + \nabla \times n^2 k^2 \psi \vec{a} \ . \tag{4.4}$$

Taking the curl operator out, we get

$$\nabla \times \left[\nabla^2 \psi + n^2 k^2 \psi\right] \vec{a} = 0 \tag{4.5}$$

Since ψ is the solution of scalar wave equation. Hence $\vec{M}$ (and therefore $\vec{N}$) satisfies vector wave equation.

Note that curl L = 0 and hence cannot satisfy Maxwell's equations for time harmonic fields. Therefore, from here we use only $\vec{M}$ and $\vec{N}$.

An important point to note is that all 3 are orthonormal functions and form a basis set. Any solution to the vector wave equation can be represented as a linear combination of these vector functions. We will attempt to construct $\vec{E}$ and $\vec{H}$ from these such that they satisfy Maxwell's equations:

$$\nabla \times \vec{E} = -ik\vec{H} \tag{4.6}$$

$$\nabla \times \vec{H} = ikn^2 \vec{E} \tag{4.7}$$

It can be shown that the following combinations of $\vec{M}$ and $\vec{N}$ forming $\vec{E}$ and $\vec{H}$ satisfy Equations 4.6 and 4.7:

$$\vec{E} = \overrightarrow{M}_v + i\overrightarrow{N}_u \tag{4.8}$$

$$\vec{H} = n\left(-\overrightarrow{M}_u + i\overrightarrow{N}_v\right) \tag{4.9}$$

Here subscripts v and u are scalar functions creating the vector solution $\vec{M}$ or $\vec{N}$. All we need to find is the scalar functions v and u and obtain $\vec{E}$ and $\vec{H}$ using Equations 4.8 and 4.9. It is easy to verify and also intuitive, that the pilot vector $\vec{a}$ for a cylinder is $\hat{z}$ i.e. unit vector pointing along the cylinder axis. Thus vectors $\vec{M}$ and $\vec{N}$ for a cylinder are as follows.

$$\overrightarrow{M_\psi} = \nabla\times\psi\hat{z} \tag{4.10}$$

$$\overrightarrow{M_\psi} = \hat{r}\frac{1}{r}\frac{\partial\psi}{\partial\phi} - \phi\frac{\partial\psi}{\partial r} \tag{4.11}$$

$$\overrightarrow{N_\psi} = \frac{1}{nk}\left\{\left[\frac{\partial\partial\psi}{\partial z\partial r}\right]\hat{r} + \left[\frac{1}{r}\frac{\partial\partial\psi}{\partial z\partial\phi}\right]\phi - \frac{1}{r}\left[\frac{\partial}{\partial r}\left(r\frac{\partial\psi}{\partial r}\right) + \frac{1}{r}\frac{\partial^2\psi}{\partial\phi^2}\right]\hat{z}\right\}. \tag{4.12}$$

Since ψ_m, the solution of the scalar wave equation in cylindrical coordinates is of the form $e^{im\phi}Z_m\left(\mathrm{r}\sqrt{n^2k^2-\beta^2}\right)e^{-i\beta z+i\omega t}$, where *m* is the azimuthal order, *Zm* is Bessel function of any kind, *r* is radial coordinate, *β* is propagation constant and *ω* is angular frequency, $\vec{M}$ and $\vec{N}$ can be further written as,

$$\vec{M} = \hat{r}\frac{im}{r}\psi - \phi\frac{\partial}{\partial r}\psi \tag{4.13}$$

$$\overrightarrow{N}_{\psi_m} = \left(\frac{-i\beta}{nk}\frac{\partial}{\partial r}\psi_m\right)\hat{r} + \left(\frac{m\beta}{nkr}\psi_m\right)\phi - \frac{1}{nkr}\left(\frac{\partial}{\partial r}\left(r\frac{\partial}{\partial r}\psi_m\right) + \frac{1}{r}\frac{\partial^2}{\partial\phi^2}\psi_m\right)\hat{z}. \tag{4.14}$$

But since ψ satisfies scalar wave equation in cylindrical coordinates which is,

$$\frac{1}{r}\frac{\partial}{\partial r}\left(r\frac{\partial}{\partial r}\psi\right) + \frac{1}{r^2}\frac{\partial^2}{\partial\phi^2}\psi + \frac{\partial^2}{\partial z^2}\psi + n^2k^2\psi = 0 \tag{4.15}$$

the last term of Equation 4.14 can be simplified. Thus

$$\overrightarrow{N}_{\psi_m} = \left(\frac{-i\beta}{nk}\frac{\partial}{\partial r}\psi_m\right)\hat{r} + \left(\frac{m\beta}{nkr}\psi_m\right)\phi - \left(n^2k^2 - \beta^2\right)\hat{z} \tag{4.16}$$

The final expression for $\vec{E}$ and $\vec{H}$ fields is

$$\vec{E}=\left(\frac{im}{r}v\right)\hat{r}-\left(\frac{\partial v}{\partial r}\right)\hat{\phi}+\left(inku\right)\hat{z} \tag{4.17}$$

$$\vec{H}=n\left(\left(-\frac{im}{r}u\right)\hat{r}+\frac{\partial u}{\partial r}\hat{\phi}+inkv\hat{z}\right). \tag{4.18}$$

Here we pause for an important observation. Note that for u=0, $\vec{H}$ has only z component while E is in the transverse plane of the cylinder. This mode is called the TE mode. While for v = 0, $\vec{E}$ has only z component while $\vec{H}$ is in transverse plane which is the TM mode. This is the consequence of β being 0. For non-zero β, the modes cannot be separated. This dissertation is all about normal incidence to the fiber or β=0. Now for concentric cylinder case, we construct u and v and use that to obtain coefficients a_n and b_n for multilayered cylinder and obtain intensity at infinity. Before doing that we need boundary conditions simplified in terms of u and v.

Boundary Conditions: For dielectric cylinder such as a fiber, tangential components (z and ϕ) of $\vec{E}$ and $\vec{H}$ fields will be continuous. Therefore the boundary conditions following from Equations 4.17 and 4.18 are:

$$\begin{aligned} n_i u_i &= n_{i+1}u_{i+1} \\ \frac{\partial v_i}{\partial r} &= \frac{\partial v_{i+1}}{\partial r} \\ n_i^2 v_i &= n_{i+1}^2 v_{i+1} \\ n_i\frac{\partial u_i}{\partial r} &= n_{i+1}\frac{\partial u_{i+1}}{\partial r} \end{aligned} \tag{4.19}$$

The expression for u for a single layered cylinder with core radius *a* and cladding radius *b* can be written as follows, as derived in [32].

$$\begin{aligned} &(r > b) && u = \sum_{m=-\infty}^{\infty} F_m \left\{ J_m(n_0 kr) - b_m{}^0 H_m(n_0 kr) \right\}, \\ &(b > r > a) && u = \sum_{m=-\infty}^{\infty} F_m \left\{ B_m{}^1 J_m(n_1 kr) - b_m{}^1 H_m(n_1 kr) \right\}, \\ &(r < a) && u = \sum_{m=-\infty}^{\infty} F_m \left\{ B_m{}^2 J_m(n_2 kr) \right\}. \end{aligned} \tag{4.20}$$

Here $F_m = (-1)^m e^{im\theta + i\omega t}$ and n_0 , n_1 and n_2 are refractive indexes of outer medium, layer and core respectively. The 4 boundary conditions applied each interface yield 4 equations relating coefficients of adjacent regions. Applying crammers rule yields the scattering coefficient:

$$b_m^0 = \frac{\begin{vmatrix} n_1 H_m^{'}(n_1\alpha_2) & n_1 J_m^{'}(n_1\alpha_2) & n_2 J_m^{'}(n_2\alpha_2) & 0 \\ H_m(n_1\alpha_2) & J_m(n_1\alpha_2) & J_m(n_2\alpha_2) & 0 \\ n_1 H_m^{'}(n_1\alpha_1) & n_1 J_m^{'}(n_1\alpha_1) & 0 & n_0 J_m^{'}(n_0\alpha_1) \\ H_m(n_1\alpha_!) & J_m(n_1\alpha_1) & 0 & J_m(n_0\alpha_1) \end{vmatrix}}{\begin{vmatrix} n_1 H_m^{'}(n_1\alpha_2) & n_1 J_m^{'}(n_1\alpha_2) & n_2 J_m^{'}(n_2\alpha_2) & 0 \\ H_m(n_1\alpha_2) & J_m(n_1\alpha_2) & J_m(n_2\alpha_2) & 0 \\ n_1 H_m^{'}(n_1\alpha_1) & n_1 J_m^{'}(n_1\alpha_1) & 0 & n_0 H_m^{'}(n_0\alpha_1) \\ H_m(n_1\alpha_!) & J_m(n_1\alpha_1) & 0 & H_m(n_0\alpha_1) \end{vmatrix}} \tag{4.21}$$

Here $\alpha_2 = ka$ and $\alpha_1 = kb$. This is similar in form to equation 5.1.28 in Kerker's book [33] for multilayered sphere, though not apparent at first look. On replacing Hankel function in the first column by J+iY, and splitting the determinant into two - D_1, D_2, first 2 columns of D_1 become identical thus vanishing D_1, while D_2 takes the form of 5.1.28 except that spherical functions ψ, χ and ζ are replaced by cylindrical functions J, Y and H respectively. This similarity is not surprising because, for normal incidence, cross section of a cylinder is similar to equatorial plane of a sphere.

The calculation of scattering coefficients in already implemented in MatScat code [34] and used in this dissertation with only minor adaptations.

Next section presents experimental details to obtain the scattering pattern to which best-fit theoretical patterns will be found using MatScat.

4.3 Experiment

To determine the film thickness and refractive index of SiN_x and SiO_2, four strands of Corning SMF28 were coated with single layer of SiN_x and four others with SiO_2. SMF was chosen for its better axial uniformity compared multimode fibers from Thorlabs. Deposition times for SiN_x are 10, 21, 30 and 40 mins while 3, 4, 5 and 6 mins for SiO_2 which grows faster.

A simple scatterometer was set up to obtain scattering pattern of the coated fibers to determine layer thickness and refractive index from the pattern. The set up schematic shown in Figure 4.1 consists of a HeNe laser (<1 mW), polarizer, beam splitter, Newport rotation stage, computer controlled stage controller, detector with pinhole mounted on a rigid metal arm 9-10 inch long while the arm is attached to the rotation stage. Optical limit switch of the stage was disabled to allow 360 degree rotation. At the center of the stage, the fiber is placed perpendicular to the beam and the stage. Fiber is secured in a chuck held in a holder screwed to a kinematic mount glued to lab jack (Figure 4.2). Kinematic mount is necessary to align the fiber perpendicular to the beam and rotation stage while lab jack is used to adjust the height of the fiber to probe different regions. The mounted fiber is placed at the center of the stage. Rotation stage is held at an elevation such that beam height and detector coincide.

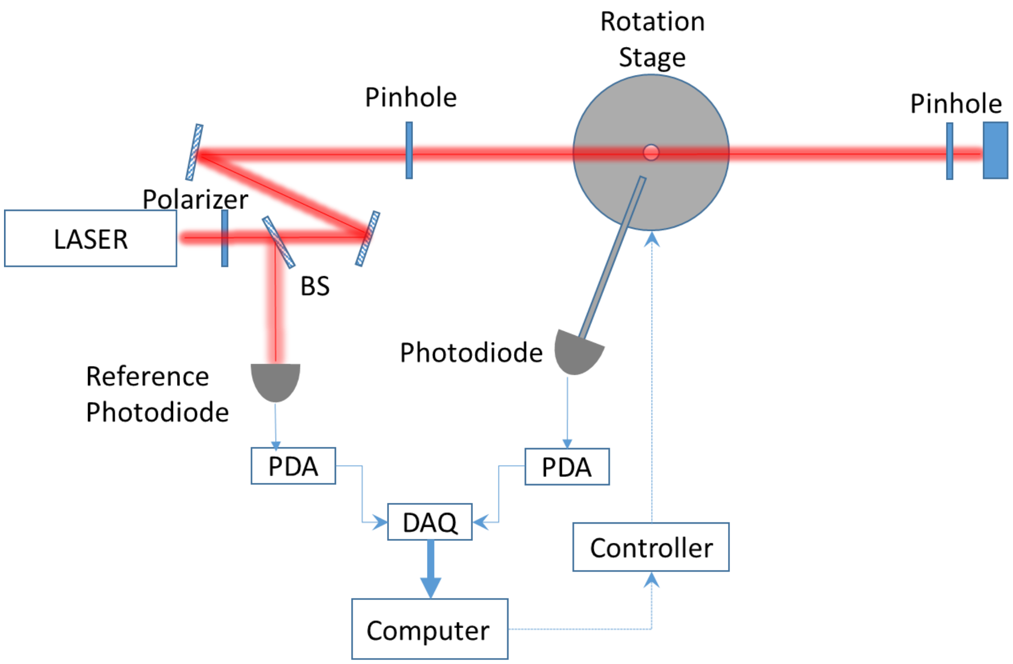

Figure 4.1: Schematic of experimental set-up. BS: Beam Splitter, PDA: Photodiode Amplifier, DAQ: Data Acquisition card. Computer controls the rotation stage and scattering signal is read through the DAQ.

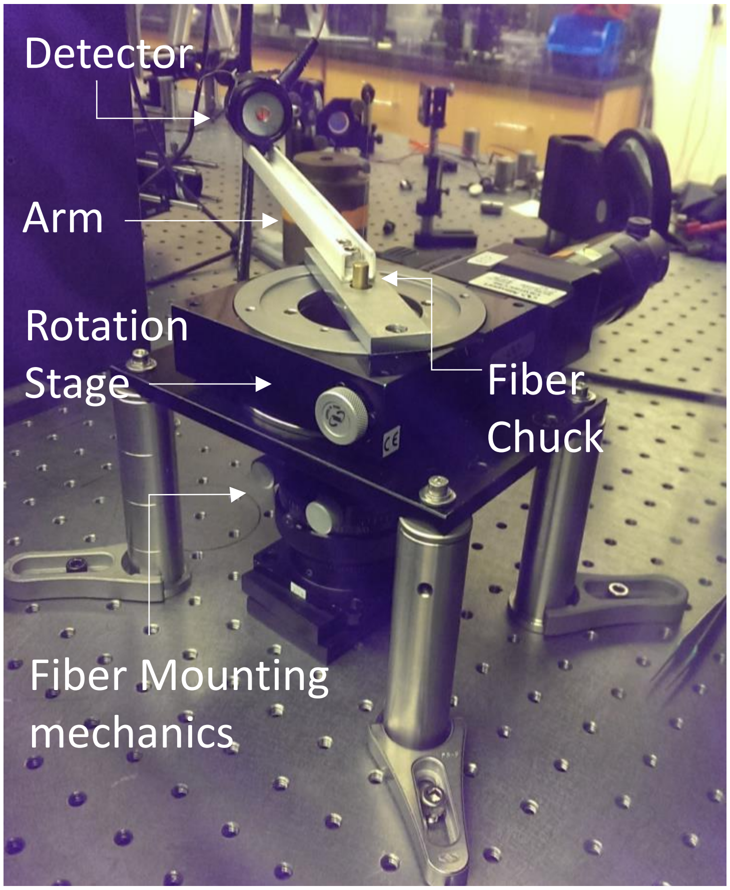

Figure 4.2: Scatterometer for fiber characterization.

The normally incident HeNe beam polarized parallel (TM) or perpendicular (TE) to the fiber axis is scattered off the fiber generating a pattern and the detector collects the scattering signal. A generated pattern for SMF28 can be seen in Figure 4.3 showing photograph of scattering of TM polarized HeNe on a circular screen with an entry hole for beam. Portion of the long fiber hit by beam is marked as fiber. Almost symmetric backscattering with a sharp cut-off can be seen on either side of the beam entry hole. Axial uniformity of the fiber can be gauged from the straightness of the fringes in the pattern. If uniform, the fringes will be aligned with the fiber axis like in this picture of SMF. Thorlabs fibers forms curved or tilted fringes generally and necessitates using a pinhole, while for SMF, a simple slit can be attached to the detector head for appropriate resolution.

When sweeping across backscattering, the detector (~1.5” wide) blocks the beam clipping data between scattering angles 175 – 180 degrees (measured from incident wavevector $\vec{k}$) which makes sense as the detector arm is about 9” long.

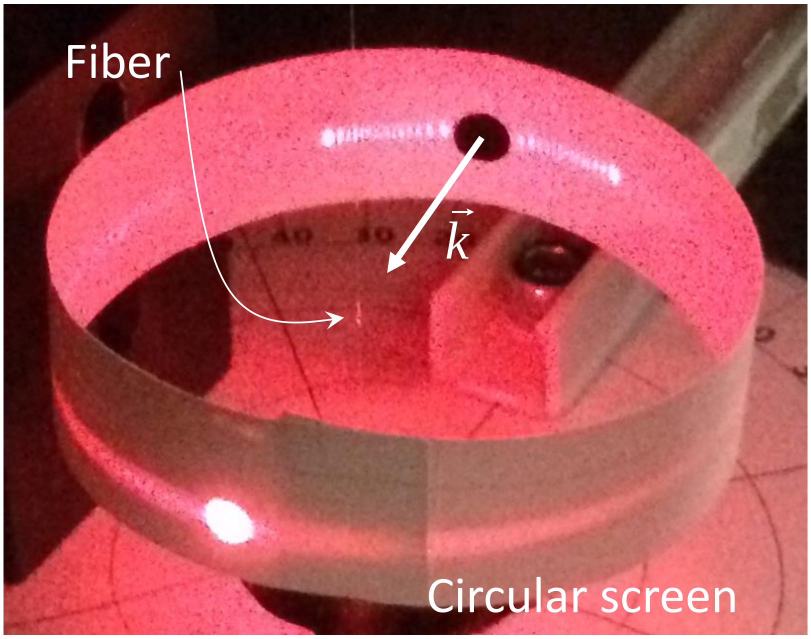

Figure 4.3: Scattering of polarized HeNe (E || fiber) from a fiber on a circular screen with an entry hole for beam. Portion of the fiber hit by beam is marked as fiber. Backscattering pattern can be seen with beam entry hole at the center.

4.4 Scattering Data for Single Layered Fiber

FT200EMT: Data for FT200EMT were collected with a pinhole mounted on the detector. Backscattering patterns of ZN7, ZN8, ZN9, and ZN10 coated with SiN_x with increasing deposition times (see Figure 3.4 for optical images) are given in Figure 4.4 - Figure 4.7. For each fiber, data was collected at 90 degree intervals around the fiber giving 4 patterns. Since the pattern is theoretically symmetric about the incident wavevector, it has been overlapped about the symmetry line in these figures. A good overlap is indicative of symmetry of the coated fiber. Any deviations are due to non-uniformity of core fiber, coated film or both. Out of these 4 fibers, overlap of ZN8 (Figure 4.5) is the best.

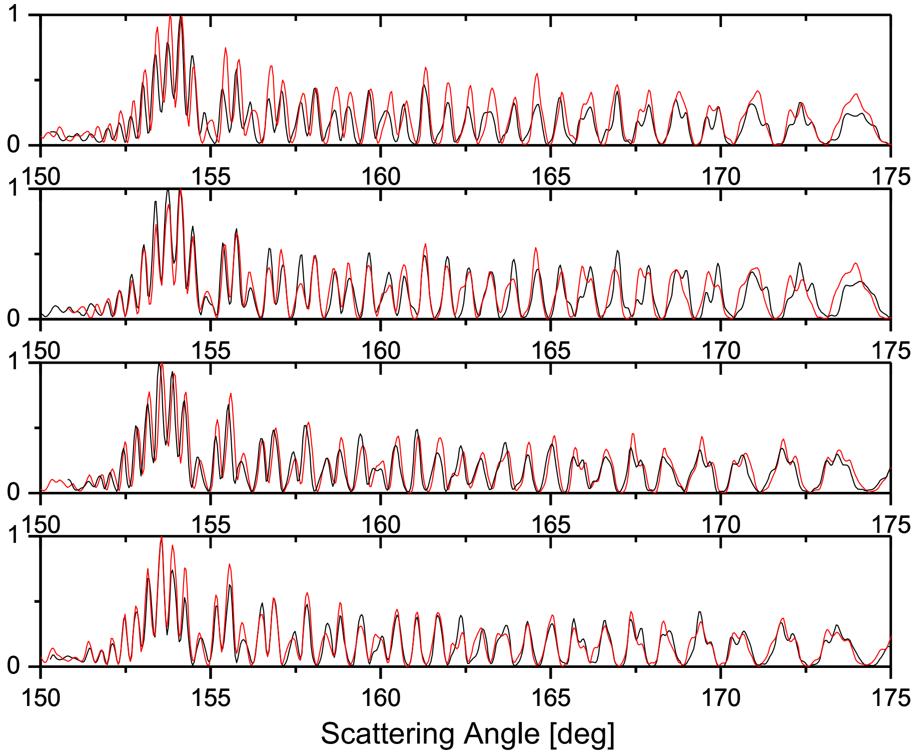

Figure 4.4: Normalized backscattering patterns of FT200EMT coated with ~50 nm layer [ZN7], taken at 90^0 azimuthal intervals. Two patterns (red and black) in each plot are data about symmetry axis i.e. incident beam.

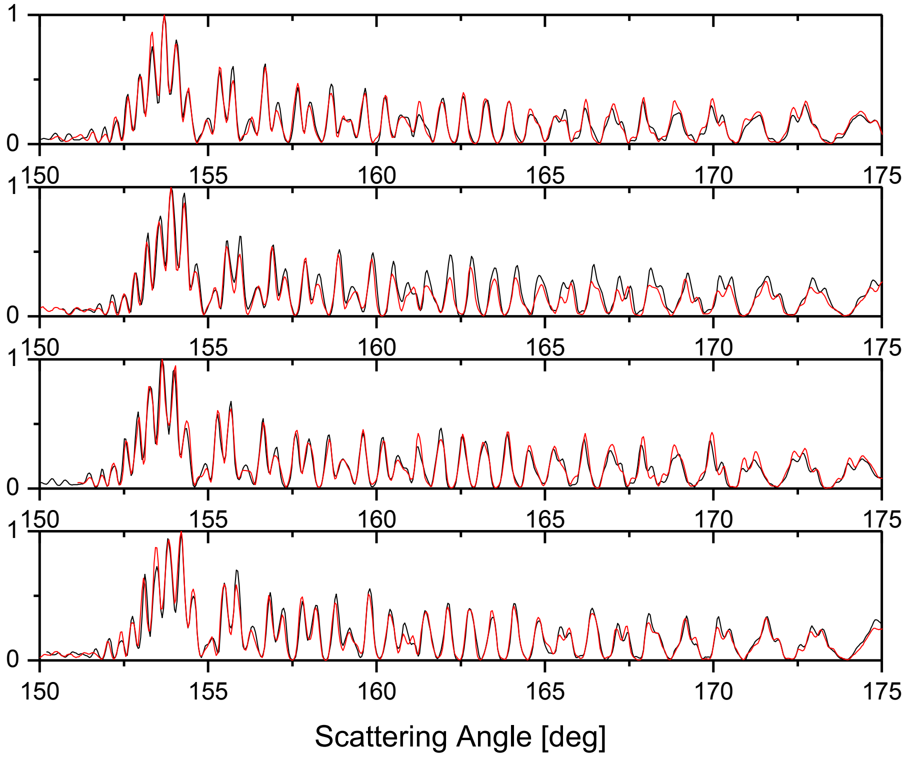

Figure 4.5: Normalized backscattering patterns of FT200EMT coated with ~100 nm layer [ZN8], taken at 90^0 azimuthal intervals. Two patterns (red and black) in each plot are data about symmetry axis i.e. incident beam.

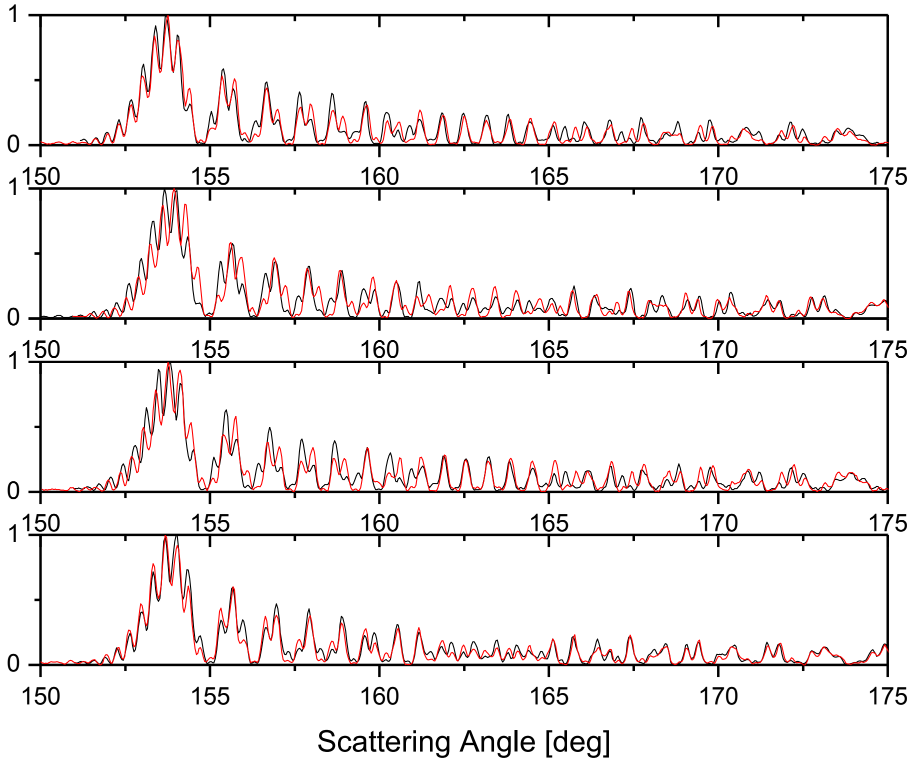

Figure 4.6: Normalized backscattering patterns of FT200EMT coated with ~250 nm layer [ZN9], taken at 90^0 azimuthal intervals. Two patterns (red and black) in each plot are data about symmetry axis i.e. incident beam.

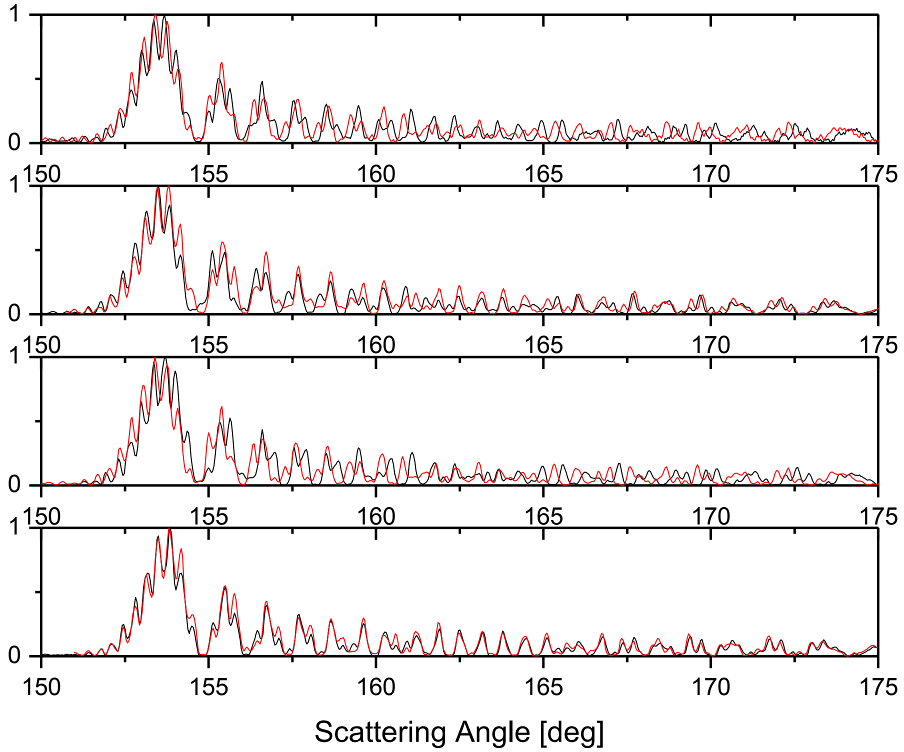

Figure 4.7: Normalized backscattering patterns of FT200EMT coated with ~500 nm layer [ZN10], taken at 90^0 azimuthal intervals. Two patterns (red and black) in each plot are data about symmetry axis i.e. incident beam.

Corning SMF28: Scattering patterns of ZN19, ZN17, ZN20, ZN21 coated with SiN_x (see Figure 3.5 for their optical image) are shown in Figure 4.8. Compared to the patterns of FT200EMT, these patterns are more spread out with broader fringes. This is due to smaller diameter to wavelength ratio that provides shorter optical path length compared to FT200EMT almost double the size of SMF.

Note that the pattern for fiber with deposition time 21 minutes is very different from other three. This is because ZN19, ZN20 and ZN21 with deposition times 10,30,40 mins were prepared with Corning SMF28e+ supplied by Fiber Instrument Sales Inc. while ZN17 with deposition time 21 mins was made with fiber from an old spool of SMF. Samples of bare fiber from this spool when characterized had a slightly higher RI than expected for silica.

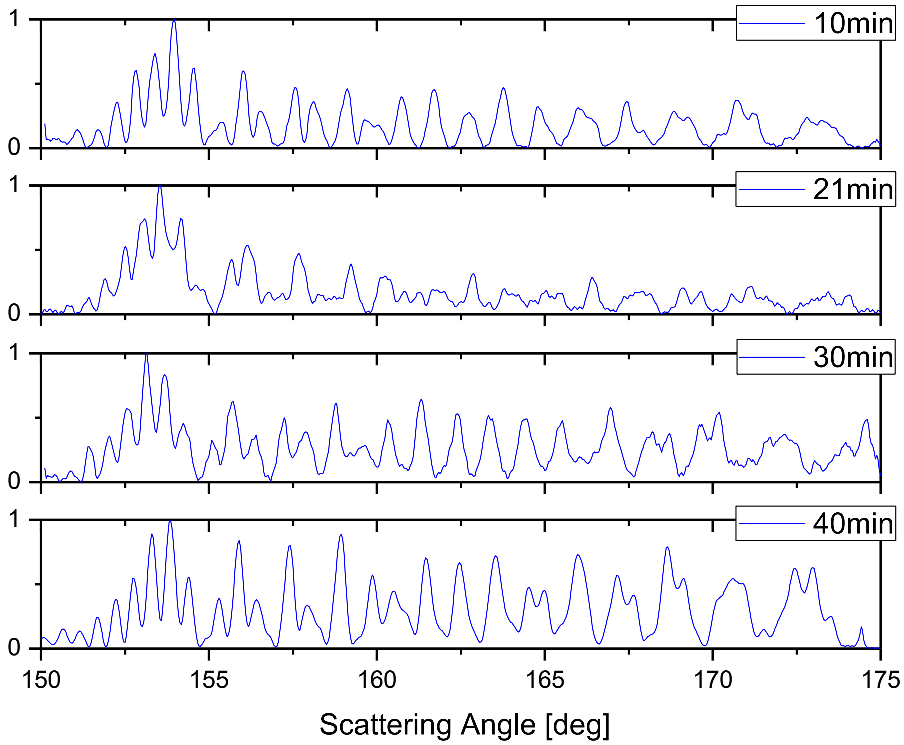

Figure 4.8: Normalized backscattering patterns of SMF28 coated with silicon nitride for 10-40 mins (Fiber ID's are ZN19, ZN17, ZN20, ZN21 respectively).

Due to high uniformity of the bare SMF28e+, LHS and RHS patterns overlap much better for coated fibers than those of Thorlabs (Figure 4.4 - Figure 4.7). An example of spectacular overlap of a coated SMF28e+ can be seen in Figure 4.9.

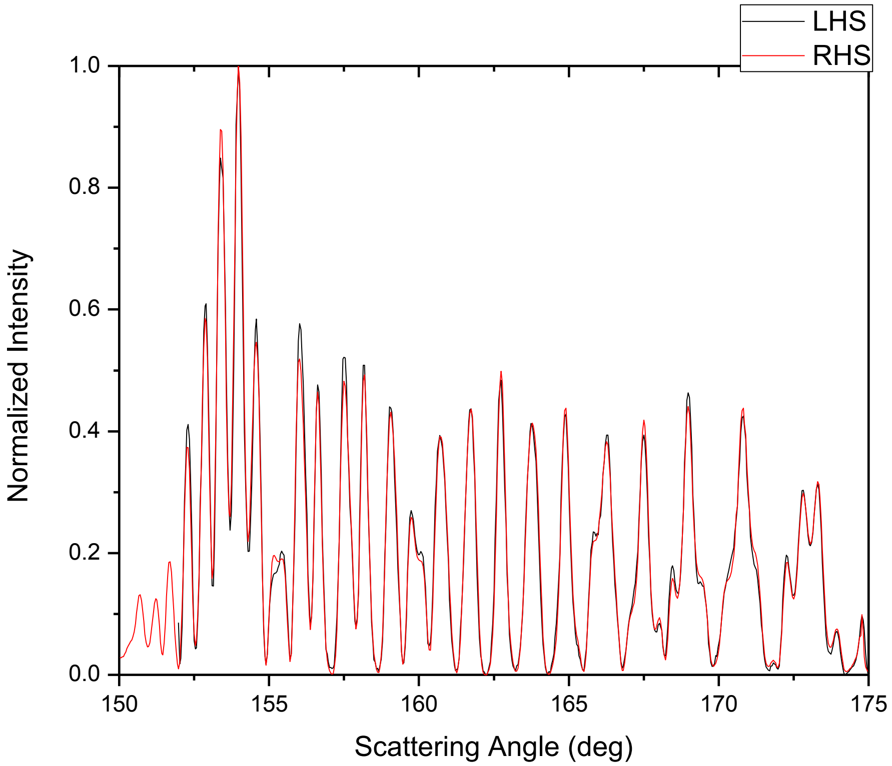

Figure 4.9: LHS-RHS overlap of backscattering of ZN19 prepared using Corning SMF28e+.

Another set of fibers (Fiber ID: ZN25, ZN26, ZN18, ZN24) was coated with silica for 3, 4, 5 and 6 minutes respectively. As mentioned earlier, these fibers do not exhibit iridescent colors due to low index contrast between fiber (fused silica) and film (PECVD silica). See Figure 3.6 for a representative optical image of silica coated fiber. Normalized backscattering patterns for these 4 fibers are shown in Figure 4.10. The fringe contrast is lower than that for SiN_x coated fibers.

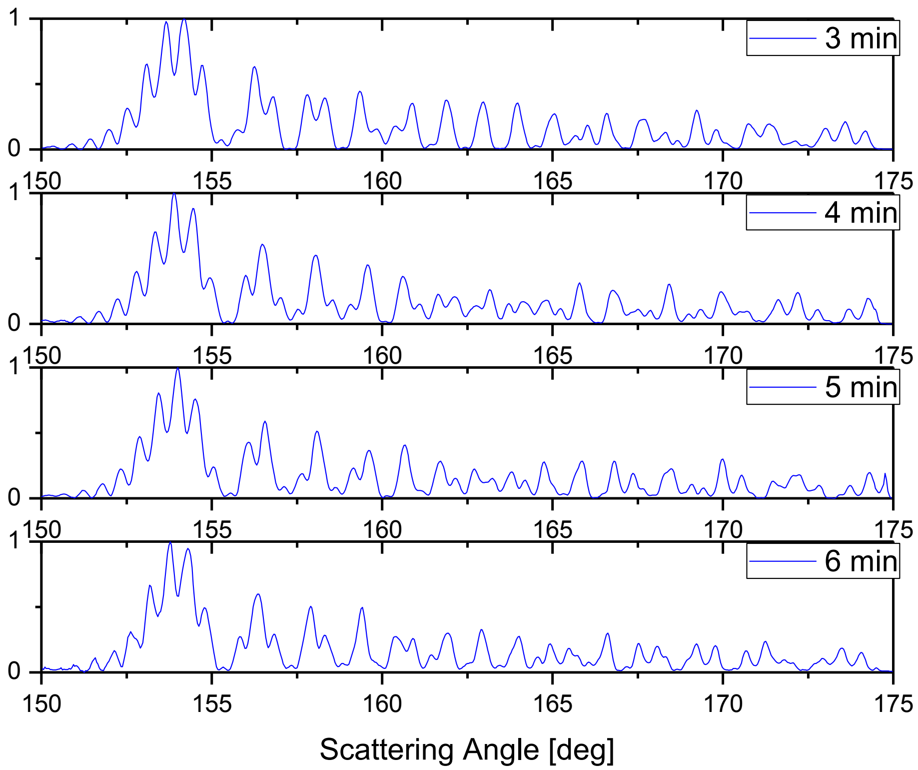

Figure 4.10: Normalized backscattering patterns of SMF28 coated with silica for 3-6 mins. (Fiber ID’s are ZN25, ZN26, ZN18, ZN24 respectively)

4.5 Data Analysis

4.5.1 Algorithm for Characterization of Fibers

The Matlab code – MatScat [34] implementing the theory of light scattering from concentric cylinders was adapted to determine the unknown refractive index and thickness of the coated fibers. The program takes in a set of radii $\mathbb{R} = \{r_1, r_2, \ldots, r_N\}$ and refractive indexes $\mathbb{N} = \{n_1, n_2, \ldots, n_N\}$ for N concentric cylinders and calculates the scattering pattern in far field for any polarization and wavelength. In this work, a brute-force search was used to characterize the coated fibers, a system of concentric cylinders essentially. The search time can be reduced by predetermining the refractive index of the core fiber on which layer is coated. The procedure to characterize the index and thickness of layers and bare fiber refractive index and diameter is explained below.

Bare Fiber: For a bare or uncoated fiber, $N = 1$ and only unknowns to be determined are r_1 - the radius of the fiber and n_1 - its refractive index. To find r_1 and n_1, a 2 dimensional search space of radius and index is created. The search space for fiber radius and index consists of M_r and M_n odd elements respectively. If tolerance specification of the fiber is $r_{10} \pm \Delta r$, then the search space S_r for radius consisting of M_r elements is $S_r = \{r_{10} - \Delta r, r_{10} - \Delta r + \delta_r, r_{10} - \Delta r + 2\delta_r, \ldots, r_{10} + \Delta r\}$ where $\delta_r = \frac{2\Delta r}{M_r - 1}$. Similarly search space S_n is $S_n = \{n_{10} - \Delta n, \mathrm{n}_{10} - \Delta n + \delta_n, \mathrm{n}_{10} - \Delta n + 2\delta_n, \ldots, n_{10} + \Delta n\}$ where $\delta_n = \frac{2\Delta n}{M_n - 1}$. Theoretical backscattering pattern is generated for each pair $\{S_r(i), S_n(j)\}$ where i and j are element index in each set. The peak of generated theoretical pattern is normalized to 1 (denoted as $\Psi(i,j)$) and compared to similarly normalized experimental data Ξ by summing the squares of the differences between theory and experimental data ($\varepsilon(i,j) = \left(\Psi(i,j) - \Xi\right)^2$). This gives a 2D map of ε .The value $\varepsilon(I,J) = \min\left(\varepsilon(i,j)\right)$ is the Least Square Error (LSE) and { $S_r(I), S_n(J)$ } are the radius and refractive index of the bare fiber. This procedure can be applied to data taken from different segments of fiber from the spool to confirm the value of refractive index (n_{co}) of the fiber.

Coated Fiber: A coated fiber has 2 concentric cylinders consisting of the core and the film. Here $N = 2$ and hence it is a 4 dimensional search space. But using n_{co} from bare fiber characterization, it reduces to 3D space of $M_{r1} \times M_{n2} \times M_t$ elements. Search range for fiber radius is still $r_{10} \pm \Delta r$, while that of film index and thickness is $n_{20} \pm \Delta n_2$ and $t_0 \pm \Delta t$ respectively. Here t_0 is the guessed thickness guided by SEM (see APPENDIX C) and Δt is chosen within 5-10% of t_0 . Choice of n_{20} was made based on the observation that transmission spectrum of Bragg fibers fabricated assuming unchanged had shifted to that corresponding to higher refractive index.

Error is calculated in the 3 dimensional space of r_1, n_2 and t. Finding the global LSE gives the root { $S_{r1}(I), S_{n2}(J), S_t(K)$ } where K is the index of thickness value corresponding to LSE. Thus the fiber diameter, film refractive index and thickness are determined at the location of beam on the fiber. The execution time of the code depends on the granularity of the search space which should be chosen wisely.

4.5.2 Results

4.5.2.1 Bare Fiber

Before moving onto characterization of films, it is helpful to first characterize the bare (uncoated) fiber to pre-determine the refractive index of its material. Once the material index is known, it can be assumed to be constant throughout the spool with only the diameter varying within the tolerance specification. Both FT200EMT and SMF28 were characterized by light scattering using the algorithm in Section 4.5.1. Scattering data were collected at 3 different times without disturbing the fiber to ensure the repeatability simultaneously.

LSE method was used to find refractive index and diameter using backscattering signal (150^0 -175^0) on either side of the beam. Retrieved n_1 and r_1 from the two sides were averaged. Table 1 shows the results for FT200EMT performing this procedure 3 times separated by about 5 minutes.

Table 1: Calibration of Bare FT200EMT using backscattering.

	Time 1		Time 2		Time 3	
	Left	Right	Right	Left	Left	Right
n	1.4575	1.4569	1.4569	1.4573	1.4575	1.4569
D [µm]	201.35	201.85	201.85	201.60	201.35	201.85
Mean	n=1.4572, D=201.60		n=1.4571, D=201.72		n=1.4572, D=201.60	

Note that n and t retrieved from one side (left or right) are quite consistent with time. The mean value of refractive index at each time is very close to that provided by Thorlabs technical support (n= 1.457173023) and the diameter is also within the specification of core diameter - 200 ± 5 µm [35].

Corning SMF28 was characterized similarly. However it is not a single cylinder like FT200EMT. Geometrically speaking, it is a set of 2 concentric cylinder – an outer cladding of diameter 125 µm and an 8 µm core embedded at the center. First the effect of the core on the scattering pattern was investigated theoretically. Figure 4.11 shows the difference between patterns with and without core exhibiting negligible difference except in the range 0^0 – 10^0 and 175^0 – 180^0. Therefore core is neglected altogether for SMF28 in all subsequent work and any data in this range was truncated for analysis.

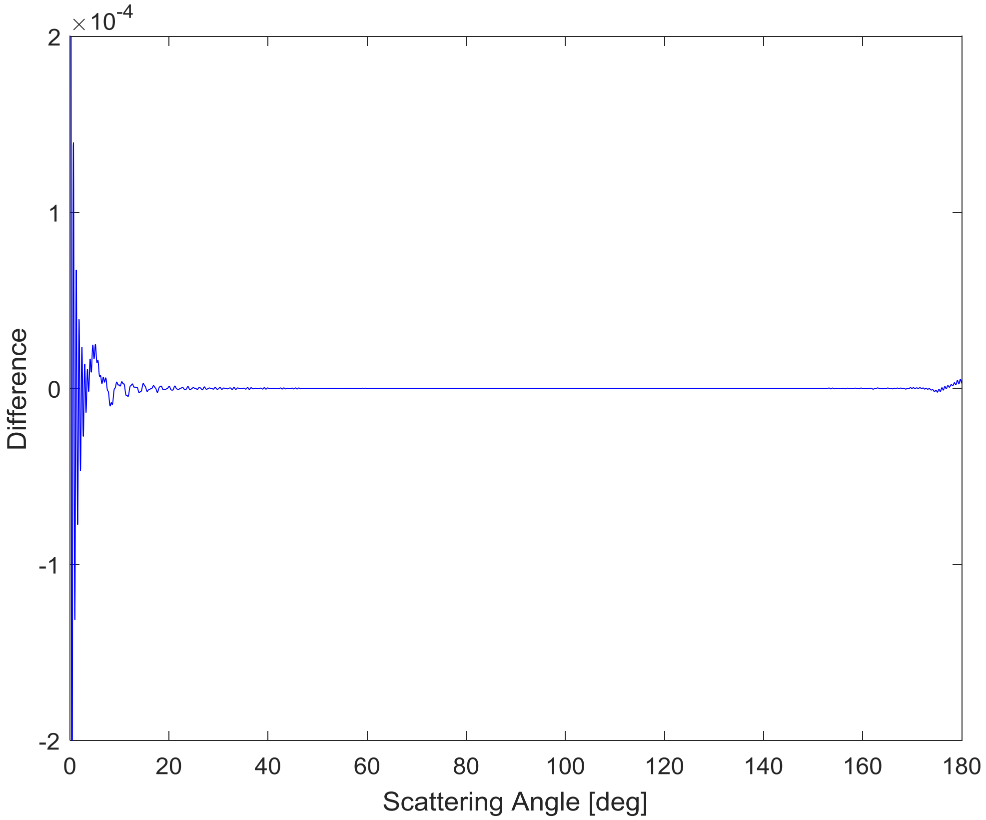

Figure 4.11: Difference between theoretical scattering patterns generated with the core and without the core.

This analysis simplified the model for SMF28 to a single rod of diameter 125 μm. Now its refractive index was found by the same method as for FT200EMT. Table 2 summarizes the results for SMF28 characterization.

Table 2: Calibration of Bare SMF28 using backscattering

	Time 1		Time 2		Time 3	
	Left	Right	Right	Left	Left	Right
n	1.4572	1.4567	1.4565	1.4574	1.4572	1.4567
D [μm]	125.098	125.119	125.133	125.077	125.098	125.119
Mean	n=1.4570, D=125.108		n=1.4570, D=125.105		n=1.4570, D=125.108	

The mean refractive index of the cladding was consistently 1.457 despite neglecting the core while the diameter is also with the specifications provided by Corning. This result further validates the fact that effect of core on backscattering is limited only within 175^0 - 180^0. Representative backscattering patterns of bare FT200EMT and SMF28e+ can be seen in Figure 4.12 with denser fringes for FT200EMT as noted earlier.

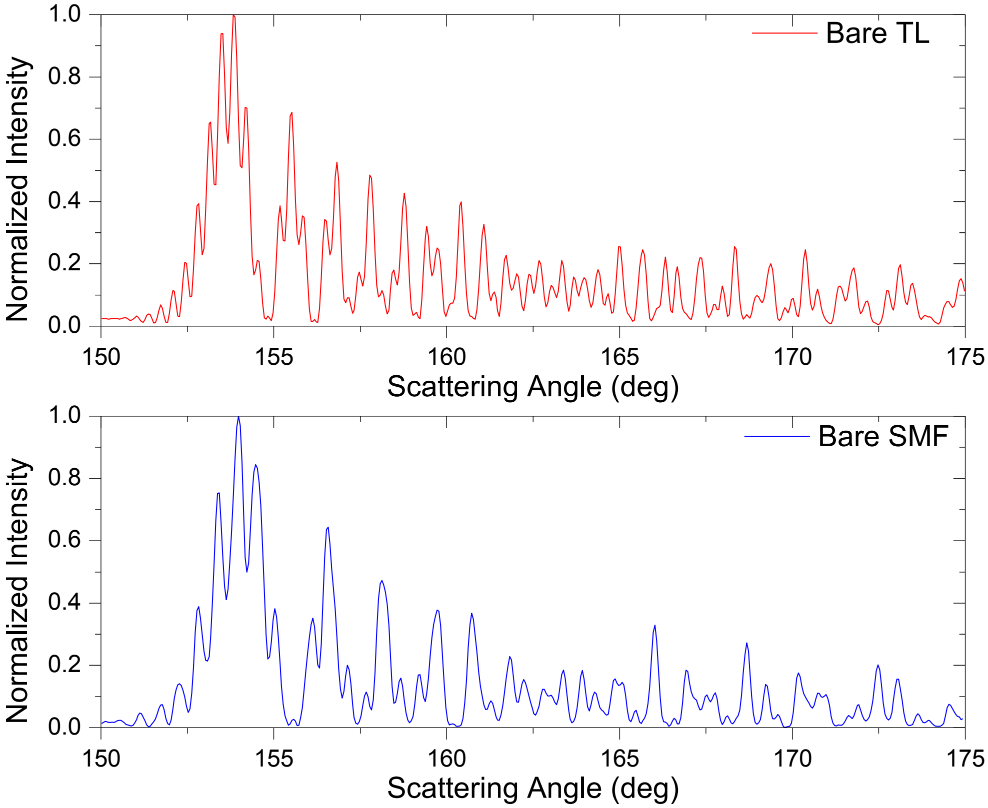

Figure 4.12: Normalized backscattering patterns of Thorlabs FT200EMT (red) and Corning SMF28e+ (blue).

4.5.2.2 Coated Fiber

Method described in Section 4.5.1 was followed to find the film RI, film thickness and fiber diameter from the best-fit pattern. Table 3 tabulates the resultant film parameters for SiN$_x$ coated fibers along with the search window limits and LSE. LSE variation with diameter axis is plotted in Figure 4.13.

Table 3: Result for SiN_x Root Search using backscattering

Fiber ID	Search Range			Root			
	n	t [nm]	d [µm]	n	t [nm]	d [µm]	LSE
ZN19	2.1 – 2.7	200 – 300	124.4 – 125.6	2.492	224	125.07	0.98
ZN17	2.3 – 2.8	475 – 525	124.3 – 125.7	2.482	502	124.99	0.65
ZN20	2.1 – 2.7	702 – 858	124.5 – 125.5	2.457	788	124.74	1.86
ZN21	2.2 – 2.8	1045 – 1155	124.3 – 125.7	2.497	1056	125.17	8.35

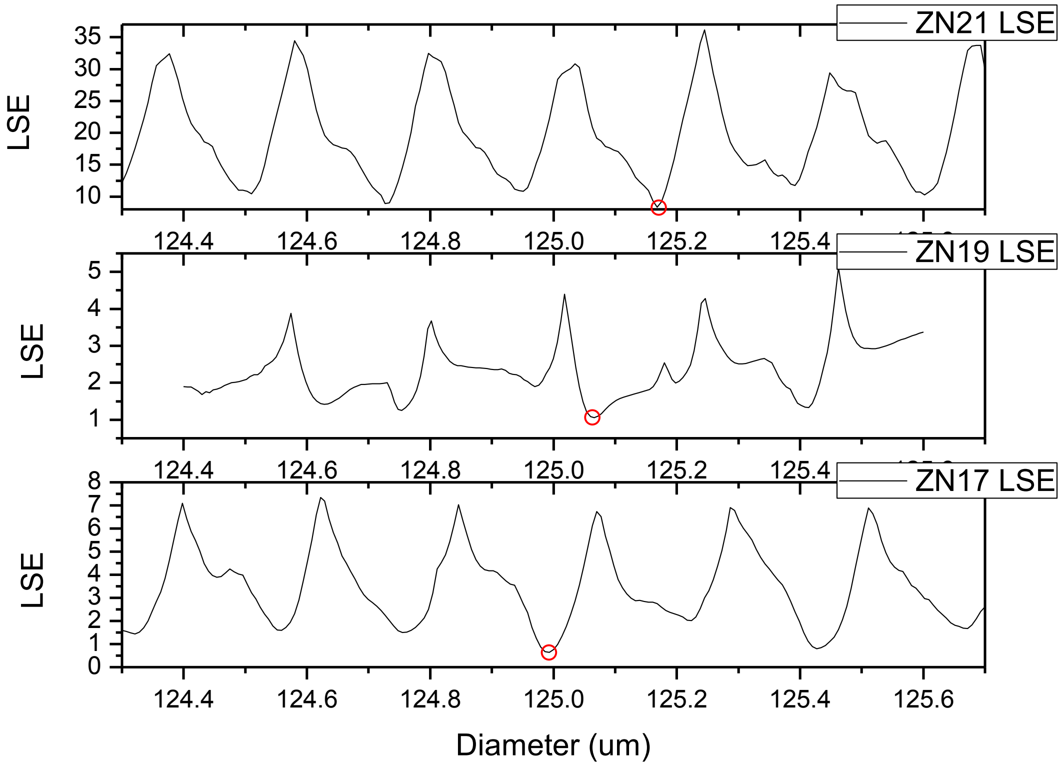

Figure 4.13: LSE vs Fiber Diameter for SiN_x coated fibers.

Some of the six valleys present in these graphs have competing LSEs, something to be wary of. The impact of such periodic LSE has been investigated in Section 4.5.3. Similar results for SiO_2 coated fibers are present in Table 4 and Figure 4.14.

Table 4: Result for SiO_2 Root Search using backscattering.

Fiber ID	Search Range			Root			
	n	t [nm]	d [µm]	n	t [nm]	d [µm]	LSE
ZN25	1.2 – 1.8	798 – 882	124.3 – 125.7	1.479	874	124.6	0.22
ZN26	1.3 – 1.7	1045 – 1155	124.3 – 125.7	1.464	1095	124.5	0.42
ZN18	1.4 – 1.6	1330 – 1470	124.4 – 125.6	1.462	1386	124.5	0.71
ZN24	1.3 – 1.7	1615 – 1785	124.3 – 125.7	1.476	1742	124.6	0.40

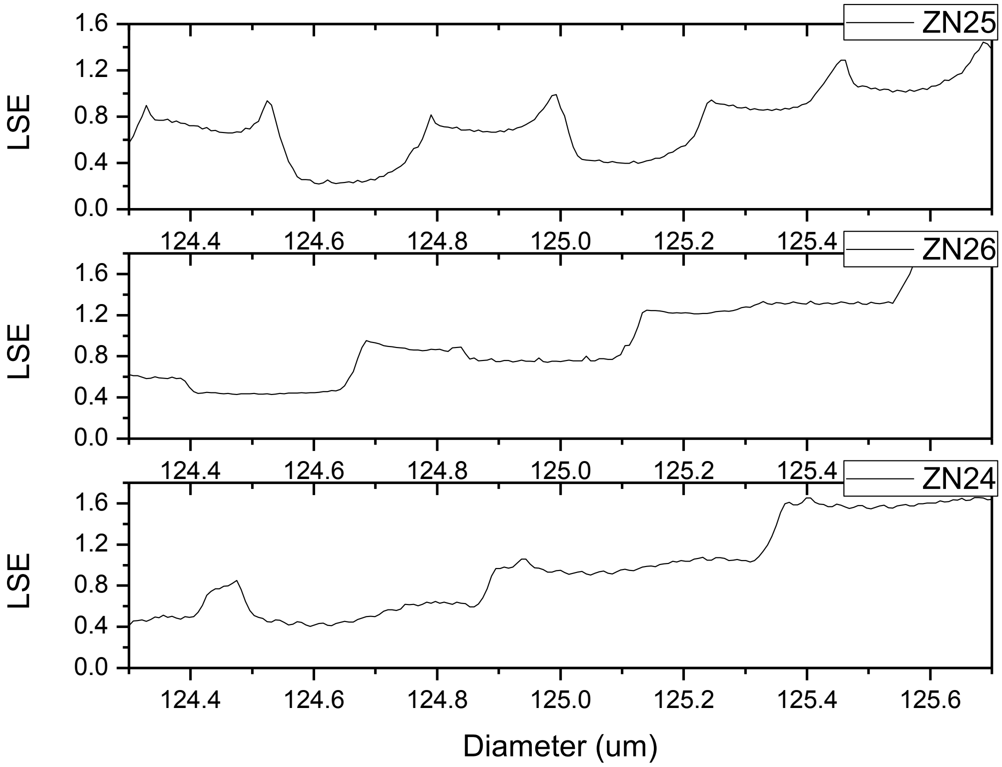

Figure 4.14: LSE vs Fiber Diameter for SiO_2 coated fibers.

The step-like LSE vs Diameter plot is significantly different from that of SiN_x which was periodic. Additionally the error is smaller than for SiN_x most likely due to similarity in the film RI and fiber RI. This is evident from Figure 4.15 showing the best fit patterns (red) superimposed on corresponding experimental scattering data (black).

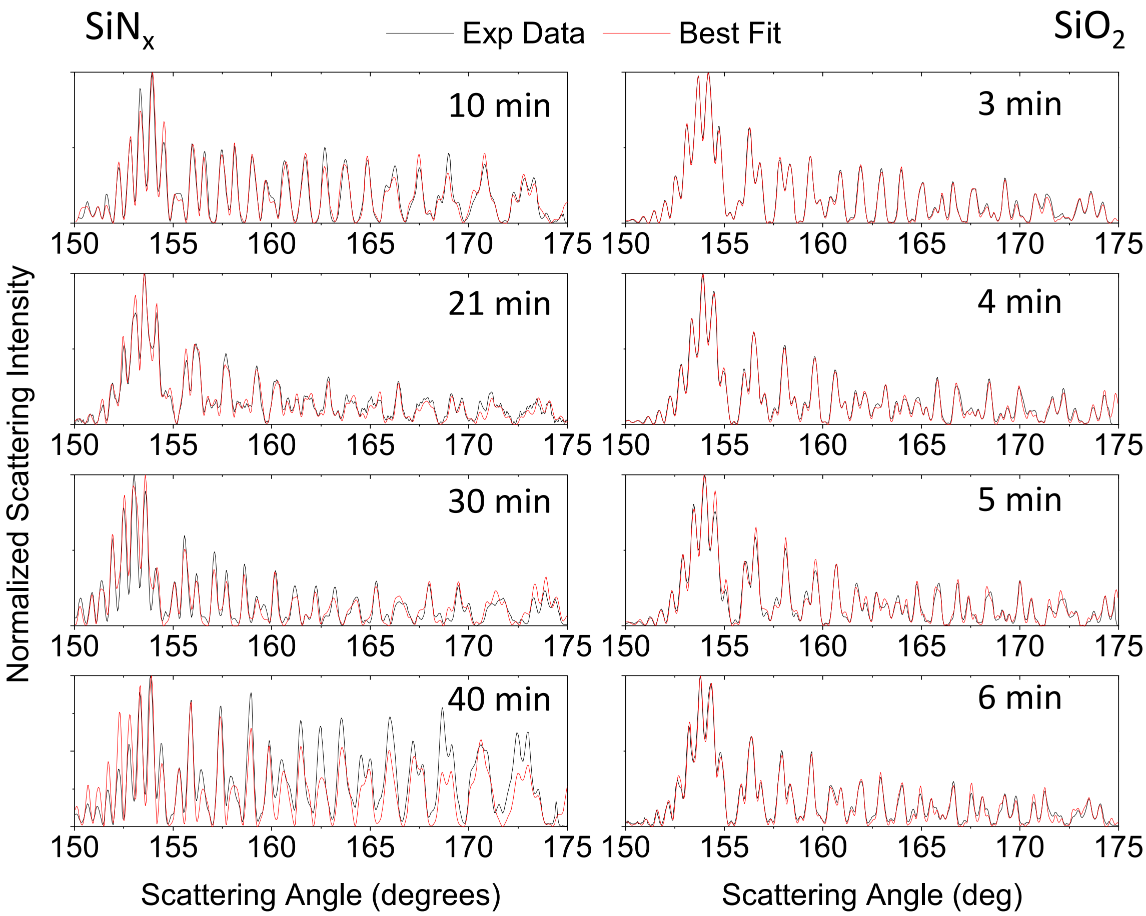

Figure 4.15: Experimental data and corresponding theoretical fit for backscattering patterns of coated fibers. Fiber ID's top to bottom: SiN$_x$- ZN19, ZN17, ZN20, ZN21 with deposition times 10, 21, 30 and 40 mins respectively; SiO$_2$- ZN25, ZN26, ZN18, ZN24 (deposition times: 3, 4, 5, and 6 mins respectively).

There is a very good agreement between theory and experiment for the case of SiO$_2$ compared to that of SiN$_x$ whose best-fit patterns deviate more with increasing layer thickness.

The retrieved best-fit values of film RI n_2 (black solid circles) and thickness t (blue solid squares) for the 4 SiN$_x$ and SiO$_2$ coated fibers are plotted in Figure 4.16 showing a linear growth of the films and almost constant refractive index. Equation of the line of best fit is y=293.65x-50.55 for SiO2 and y=25.98x+2.62 for SiN$_x$ implying a growth rate for

SiO_2 an order of magnitude greater than for SiN_x. These growth rates are higher than those obtained previously for stationary fiber on the platen [22] (Figure 4.17).

The refractive index of SiN_x (n=2.49) is also significantly higher than that on flat wafer. These observations are qualitatively in agreement with [24] as the fiber is at an elevation from the base where the wafer is placed in conventional usage of PECVD. In addition to elevation, rotation and geometry of our substrate also contribute to deviation from film growth characteristics on wafers. Note that these results were obtained under the assumption of perfect circular geometry, while in practice, the following factors are potential sources of error: 1) ellipticity of the fibers [25] 2) eccentricity of the 8 µm core, 3) surface roughness of film, film cracks/gaps if present, 4) any eccentricity of fiber and detector system.

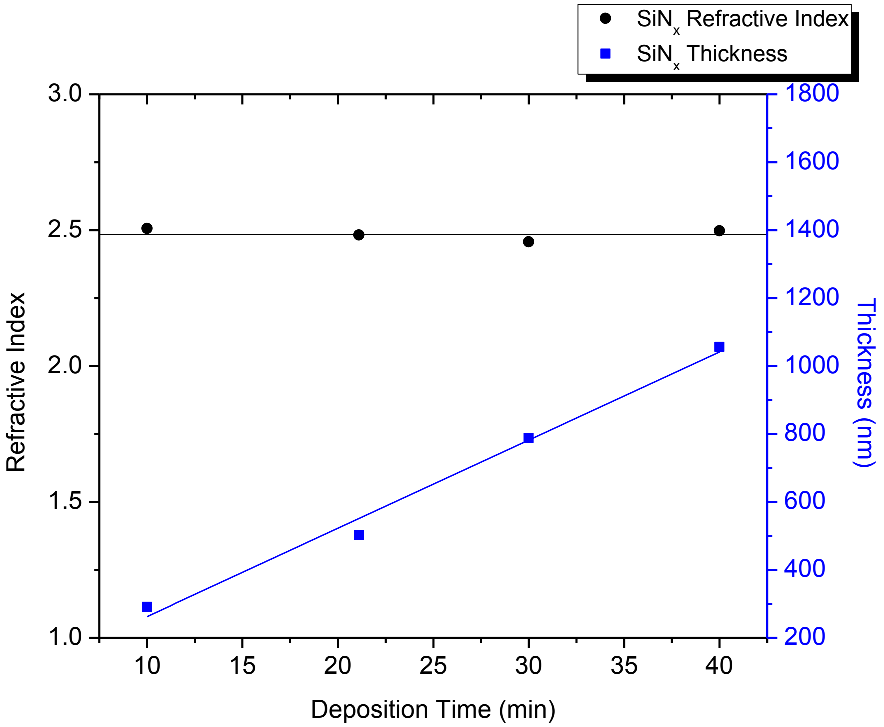

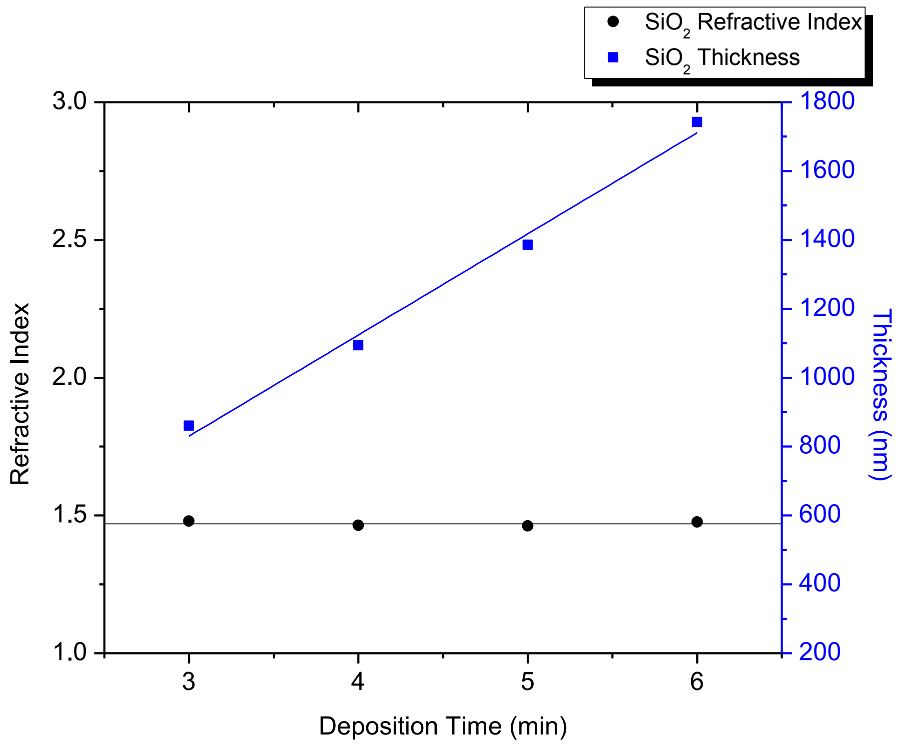

Figure 4.16: Refractive index and thickness as a function of deposition time retrieved from scattering pattern of the coated fibers. Blue line is the line of best fit while black line is located at the mean value of refractive index.

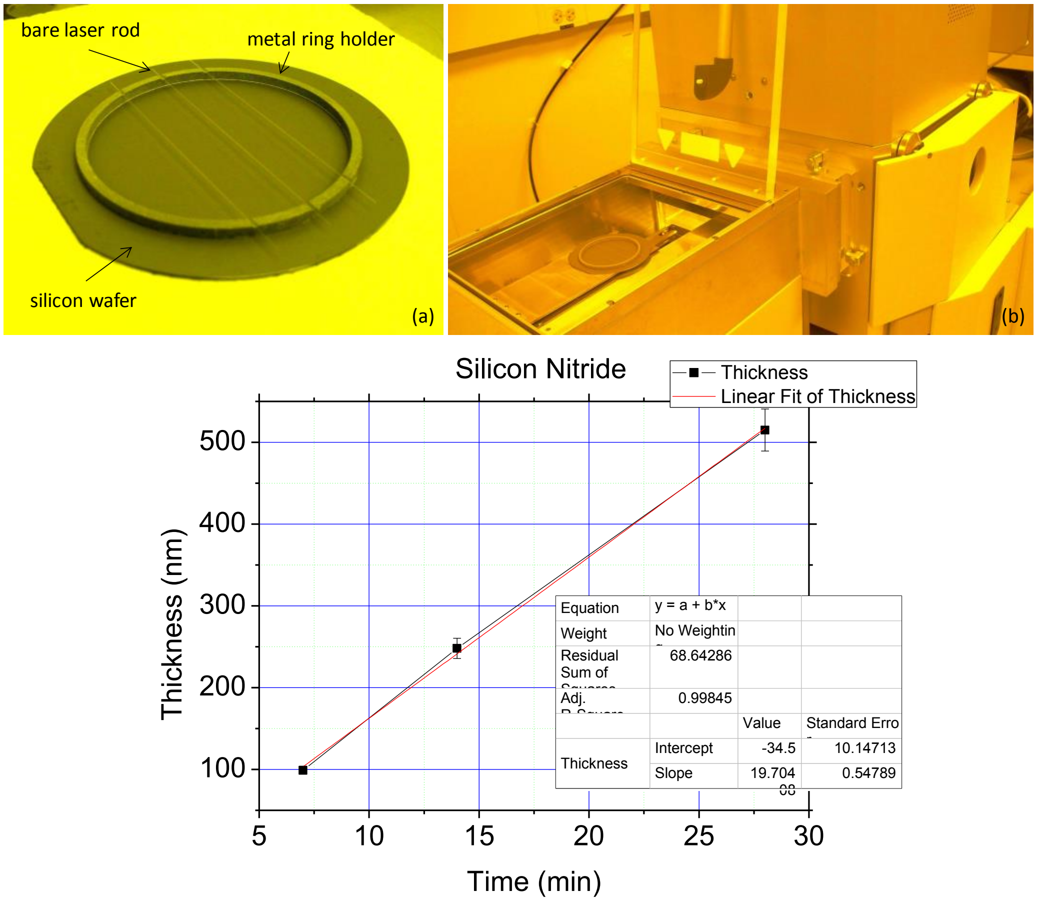

Equation	y = a + b*x		
Weight	No Weightin		
Residual Sum of	68.64286		
Adj.	0.99845		
		Value	Standard Erro
Thickness	Intercept	-34.5	10.14713
	Slope	19.704 08	0.54789

Figure 4.17: Silicon nitride growth rate curve on stationary fiber (a-b). Reproduced from [22].

A representative error bar was calculated using ZN9 (~11 min deposition of SiN_x). Scattering data at 90 degree intervals around the fiber were used to find the root at each orientation (Table 5). The mean refractive index is 2.49 and standard deviation is 0.0076 while the mean thickness is 259 nm and standard deviation is 2.4 nm. However with increasing thickness, the as we saw in Figure 4.15, the pattern starts to become more asymmetrical indicating increased non-uniformity which would mean higher error for thicker layers.

Table 5: Root search result for error bar calculation on ZN9

Orientation Angle [deg]	n_2	t [nm]
0	2.49	260
90	2.48	256
180	2.50	257
270	2.49	261
	$\langle n_2 \rangle = 2.49$, SD = 0.0076	$\langle t \rangle = 258.6$, SD = 2.4283

For validation of the results, thicknesses retrieved by scattering were compared to those obtained from SEM of coated fibers (Figure 4.18) fabricated using FT200EMT (APPENDIX C) [25].

In Figure 4.18 (a), SiN_x thicknesses retrieved by Mie scattering and SEM are plotted together. Fibers used for SEM are ZN9, ZN11, ZN12 and ZN13. The deposition time and measured thickness is tabulated in Table 6. These were made 2 years before the 4 fibers used for scattering based characterization. The values obtained from scattering are located close to the SEM calibration line in red. In fact, there is a small positive offset in the thicknesses obtained by scattering from the calibration line. This could be due to either different growth on FT200EMT (used for SEM) than on SMF28 or some other change in the calibration of the PECVD tool itself over the years which was stood unused for a long time.

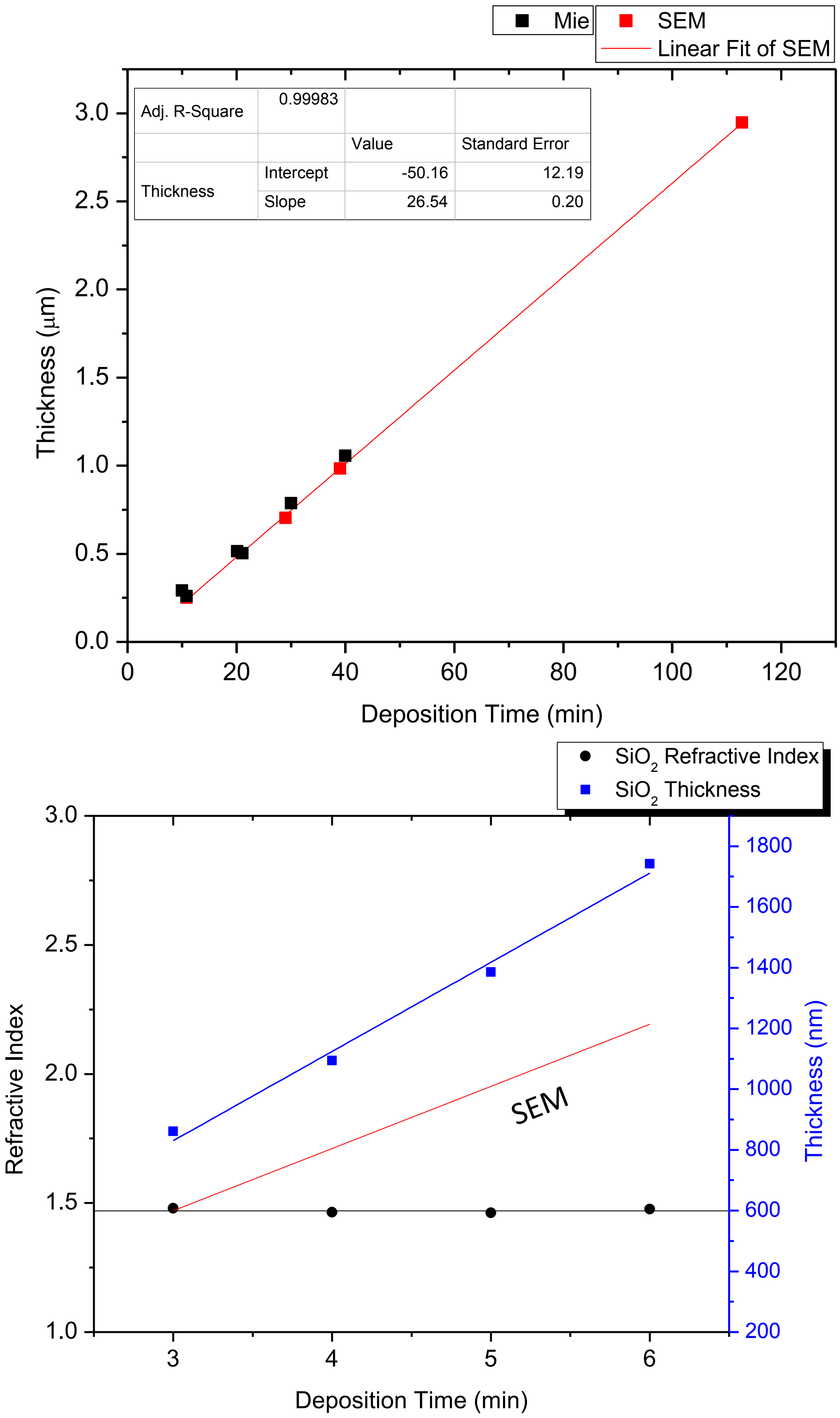

Figure 4.18: Growth rate obtained using Scattering compared to that obtained from SEM. Left: SiN_x; Right: SiO_2.

Table 6: Scattering vs SEM results for SiN_x

Deposition Time [min] (on SMF)	Thickness [nm] **Scattering**	Deposition Time [min] (on FT200EMT)	Thickness [nm] **SEM**
10 [ZN19]	291	10.82 [ZN9]	251
10.82 [ZN9]	260	29 [ZN11]	704
20.14 [ZN10]	515	39 [ZN12]	984
21.1 [ZN17]	502	112.81 [ZN13]	2947
30 [ZN20]	788		
40 [ZN21]	1056		

Table 7: Thickness characterization by scattering for SiO_2

Deposition Time [min]	Thickness [nm] **Scattering**
3 [ZN25]	861
4 [ZN26]	1094
5 [ZN18]	1386
6 [ZN24]	1742

As a sanity check, the fiber with deposition time 10.82 mins (ZN9) was also characterized by Mie scattering. The thickness obtained is 260 nm, deviating 4% from growth rate curve (red) obtained by SEM (APPENDIX C).

A similar comparison between SEM and scattering results for SiO_2 coated fibers is shown in Figure 4.18 (b). The SEM calibration line was obtained from a single multilayered fiber (Figure C.) with different deposition times of bilayers of SiN_x and SiO_2 unlike the case of SEM line for SiN_x obtained from single layered fibers. See **Error! eference source not found.** in Appendix C for the deposition time and corresponding layer thickness giving the calibration line. There is no agreement between the thickness obtained from SEM and scattering for SiO_2. A possible reason is that growth rate stabilizes after about 10-12 minutes of deposition – the reason for running a predep process before any deposition in PECVD. We cannot run predep before coating fibers as the fiber is not loaded from the loading dock, instead requires opening of chamber (see APPENDIX B for operation details). As given in Table 7 the deposition times for the 4 SiO_2 coated fibers used for scattering are well under 10 mins, whereas the 1 multilayered fiber used to obtain SEM calibration line has different chamber conditioning due to successive deposition. The very first layer of SiO_2 in this multilayered fiber was deposited after 10 mins of SiN_x growth (Figure C.1).

Fibers were also prepared at different speeds to study the effect of speed on refractive index and thickness. The results are presented in Appendix D.

4.5.3 Challenges using Backscattering

Using backscattering alone may be challenging to determine the root uniquely as cautioned by the periodic LSE plots of Figure 4.13. For certain combinations of $\{n_2, t, r_1\}$, backscattering pattern is almost degenerate. Experimental errors may make it difficult to detect this minor difference between these similar patterns especially for large fiber diameter to wavelength ratio. To lift the degeneracy, multiple wavelengths could be used along with full 0-180 scattering data [26]. The latter would be more computation intensive due to large size parameter (or multipoles to be calculated), an increase in data points and normalization of data to theory. In this section, degeneracy of backscattering patterns for bare fibers in investigated by displaying scattering patterns for first two diameter values that best fit the experimental data.

Methods & Parameters: Refractive index of bare fiber was fixed to 1.457 and search range for core diameter is chosen between 124.3 - 125.7 µm. First two local minima (1st-red, 2nd-black) are circled in Figure 4.19. Scattering patterns corresponding to these diameters are shown in the lower 2 subplots. These graphs are corresponding to data taken for two orthogonal orientations of the fiber. It is difficult to tell which diameter gives a closer fit to the experimental data. LSE is not a reliable indicator of similarity for such a close match. Even though the difference between these diameters is less than a micron, it matters when the fiber is coated with thin film. A diameter off by few hundred nanometers can lead to error in best fit film parameters.

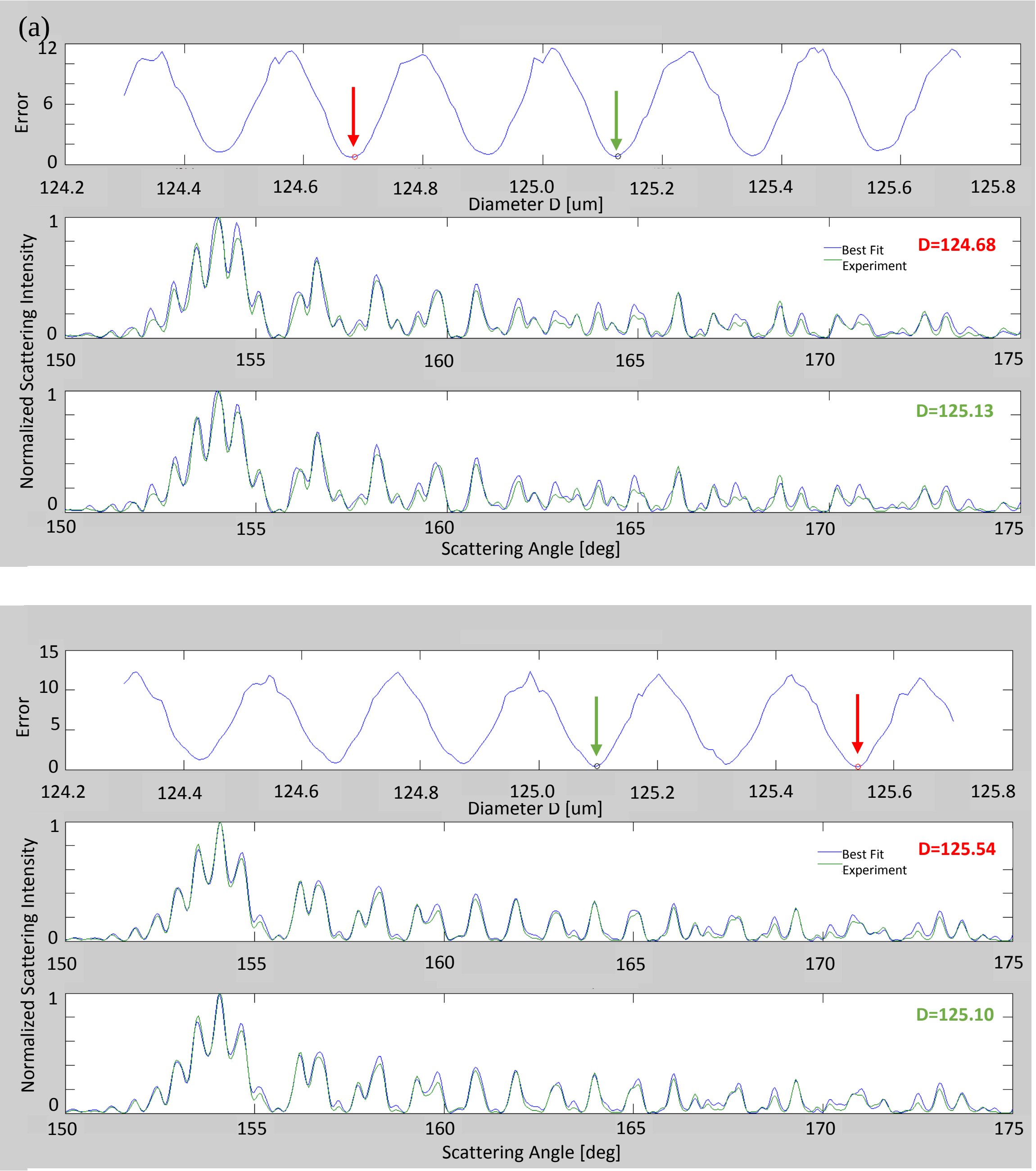

Figure 4.19: Apparent degeneracy in backscattering patterns of SMF28. (a) and (b) are for two orthogonal orientations of the fiber.

4.5.4 Alternatives

Due to the apparent degeneracy in the backscattering patterns, uniqueness of root using other scattering regions was investigated numerically. The simplest case of bare fiber was studied. Theoretical pattern for bare fiber with $2r_1$ = 125 µm and n_1 = 1.457 was assumed to be experimental data for which best fit parameters are to be found. Patterns for $2r_1$ in the range 125 ± 0.7 µm were compared to this. Error was plotted against $2r_1$ for 3 scattering regions: 1) backscattering ($150^0 – 180^0$), 2) forward scattering ($5^0 – 20^0$) and 3) entire pattern ($0^0 – 180^0$). As shown in the top plot of Figure 4.20, the error plot is periodic for backscattering with 7 valleys, while that of forward scattering (middle) has an unambiguous unique root though gives an impression of increased period of about 1.2 µm. In contrast, the bottom graph using entire scattering has no nuance of periodicity and also has a unique root.

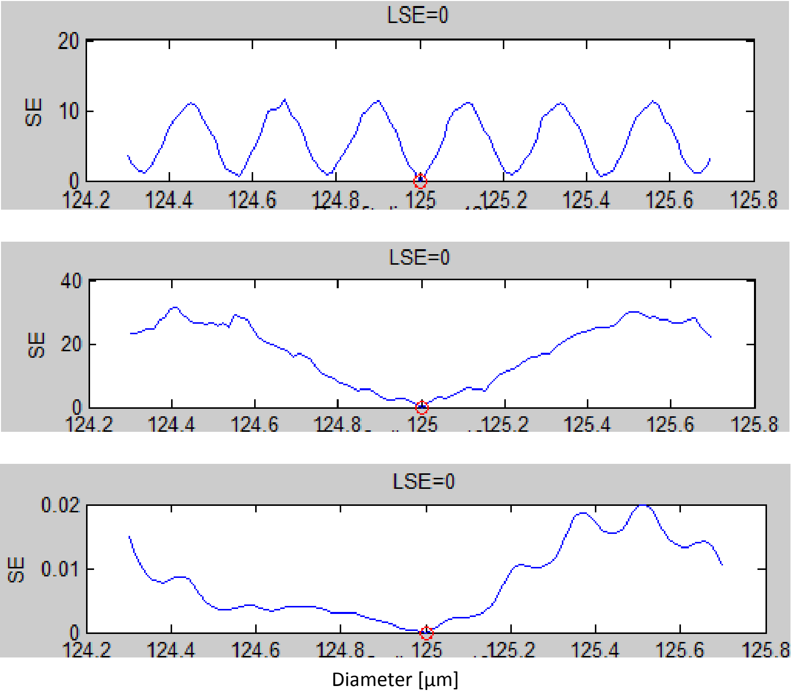

Figure 4.20: Error plot for different scattering regions. Top: $150^0 – 180^0$, Middle: $5^0 – 20^0$, Bottom: $0^0 – 180^0$.

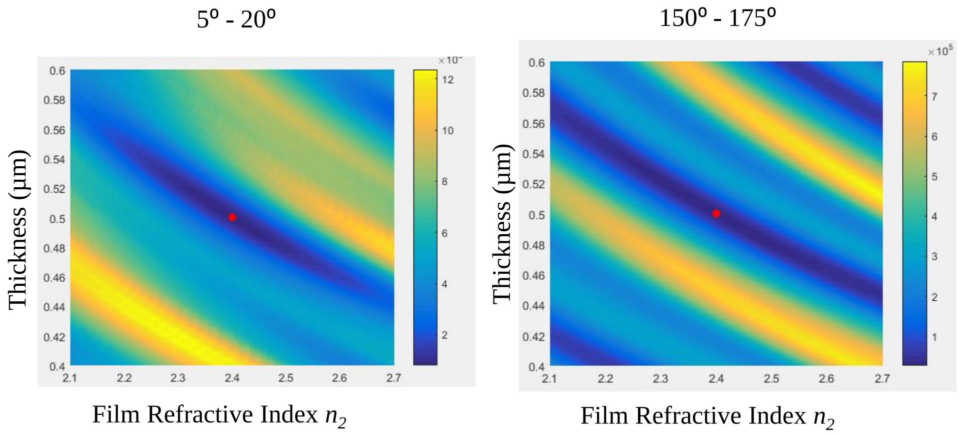

5^o - 20^o 150^o - 175^o

Figure 4.21: 2D error plot for coated fiber for forward and backscattering regions.

Similar analysis for coated fibers is shown in the form of 2D plots in Figure 4.21. It shows theoretical 2D error plot for a hypothetical coated fiber with diameter 125 µm, film RI = 2.4 and film thickness = 500 nm. Every point on the film thickness vs film RI plot is error between pattern of this hypothetical fiber and pattern of a fiber with same diameter but film parameters defined by that point. Lowest error is indicated by red dot which obviously occurs at RI = 2.4 and thickness = 500 nm. The error plot for backscattering (150^0 – 175^0) on the right has 3 long blue bands or valleys of minima within the search window. Also the central band containing the root is not as confined compared to 2D error plot of forward scattering (5^0 – 20^0) which has only one blue valley with a well confined root in the same search window.

The above analysis indicates that in order to obtain a unique root unambiguously, portion of forward scattering (e.g. 5^0 – 20^0) or entire scattering could be used. Next section presents full scattering data from 10^0 – 175^0 for fibers coated with SiN$_x$ followed by 3D root search for one of them to see if that helps.

4.5.4.1 Full Scattering Data

The data presented in the previous sections so far were limited to backscattering region i.e. from $150^0 – 175^0$. In this section, a collection of scattering data ranging from $10^0 – 175^0$ for both TM and TE polarizations are presented (Figure 4.22).

Immediately noticeable feature in these patterns is the symmetry. Corning SMF28e+ is far more symmetric than Thorlabs FT200EMT. Second is the difference in the backscattering tail. Pattern with TM polarization has a sharp tail while that for TE is more rounded off in accordance with observation by Marcuse and Presby [36] for bare fibers. In addition, coated fibers exhibit a larger backward to forward scattering ratio than the bare fiber counterparts. The fiber with thickest coating – ZN21 (see Figure 3.5 for image), has the most asymmetric and distorted pattern. It may be due to mechanical flaw in the thick coating.

<table>
<tr><th>TM (E || Fiber)</th><th>TE (E ⊥ Fiber)</th></tr>
<tr><td>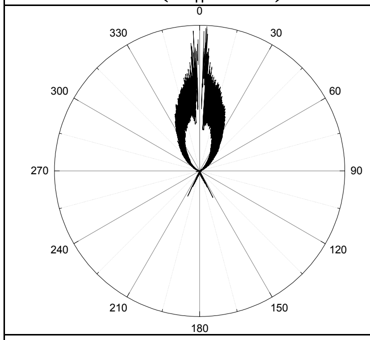
</td><td>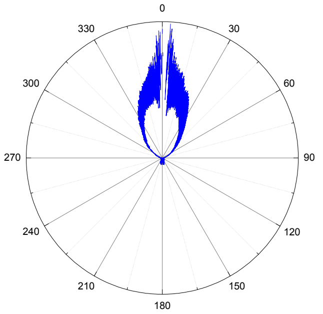
</td></tr>
<tr><td colspan="2">Uncoated FT200EMT</td></tr>
<tr><td>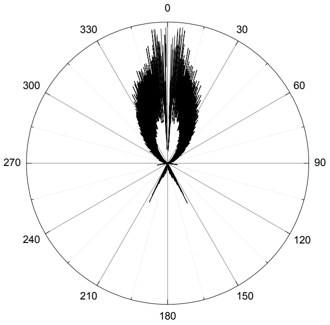
</td><td>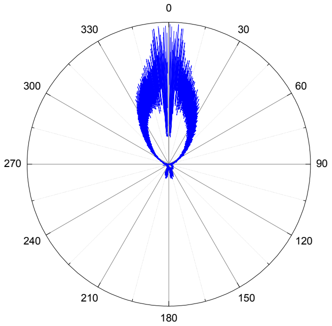
</td></tr>
<tr><td colspan="2">Uncoated SMF28e+</td></tr>
</table>

Figure 4.22, continued

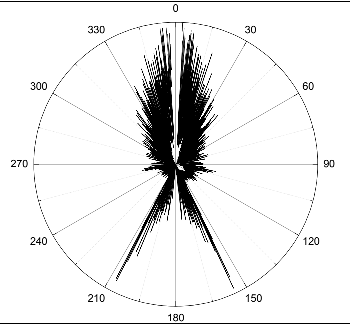

ZN19

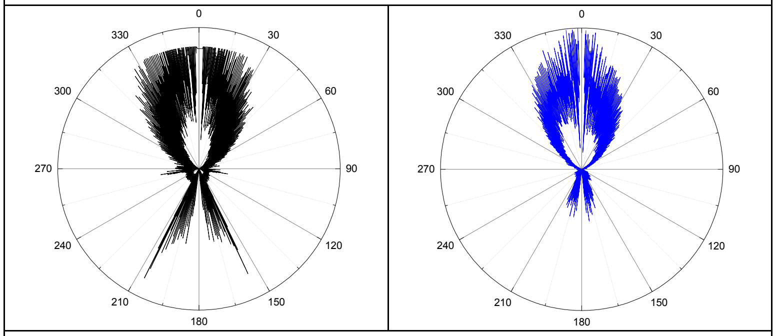

ZN17

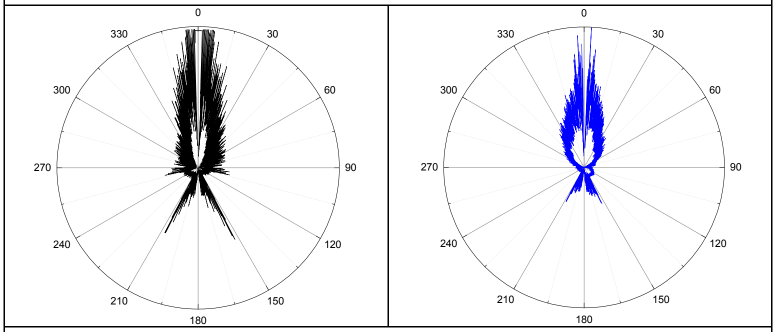

ZN20

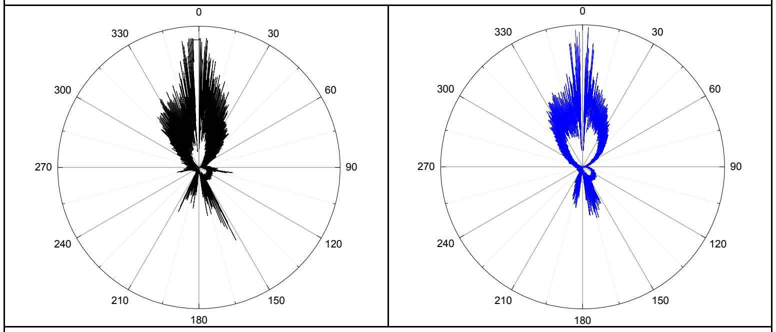

ZN21

Figure 4.22: Full Scattering Data for coated fibers. See Figure 3.5 for complete fiber recipes.

4.5.4.2 Data Analysis

In this section, results for 3D root search using full scattering data of ZN20 for TM polarization are presented. Ideally full scattering data should be available from 0^0 - 180^0. But due to very strong intensity close to 0^0 (|| incident beam) and blocking of $\mp 5^0$ of backscattering (anti || incident beam), we restrict the data to 10^0 - 175^0. This is also the region where 8 µm core has negligible effect on the pattern. Therefore theoretical scattering pattern $\{I_{ith}\}$ considered is also restricted to 10^0 – 175^0. The scale of the experimental and theoretical patterns is equalized by area normalization. Area of experiment/theory scattering pattern (A_e or A_t) = sum ($I_{iexp(th)}$ ($\theta \epsilon [10^0, 175^0]$))*$\Delta\theta$. Theoretical pattern was calculated for same $\{\theta_i\}$ as experimental. Hence $\Delta\theta$ is equal for both. Before calculating Least Square Error (LSE), the area of the theoretical pattern (A_t) is normalized to the area of experimental data (A_e): Normalized_I_{ith} = $I_{ith}/(A_t/A_e)$. A 3D root-search is conducted in the search space of parameters $\{n_{layer},t_{layer},d_{core}\}$ where n is refractive index, t is thickness and d is diameter. The search range $\{t_{layer}\}$ is dictated by SEM growth rate obtained from calibration fiber, while $\{d_{core}\}$ is given by tolerance spec of the fiber. Since RI has increased [37], we search in a range higher than *n* expected for flat wafer (*n* = 2 @ λ=632.8 nm).

Parameters:

Fiber used: ZN20

```
n0=2.5;                 %guess layer index
d0=125;                 %guess for variable core diameter (um)
t0=0.75;                %guess coating thickness (um)

%search range for each dimension
dd=0.7;                 %core diameter variation = +- dd um
dn=0.3;                 %delta index SiN
dt=10/100 * t0;         %SiN coating thickness variation = +- tt um

%resolution
Nd=201;                 % core dia
Nn=31;                  % layer index
Nt=51;                  % layer thickness
```

Results:

LSE vs diameter plot obtained from the 3D search: Each point on the graph is the

LSE of the 2D *n* vs *t* plot at a given diameter.

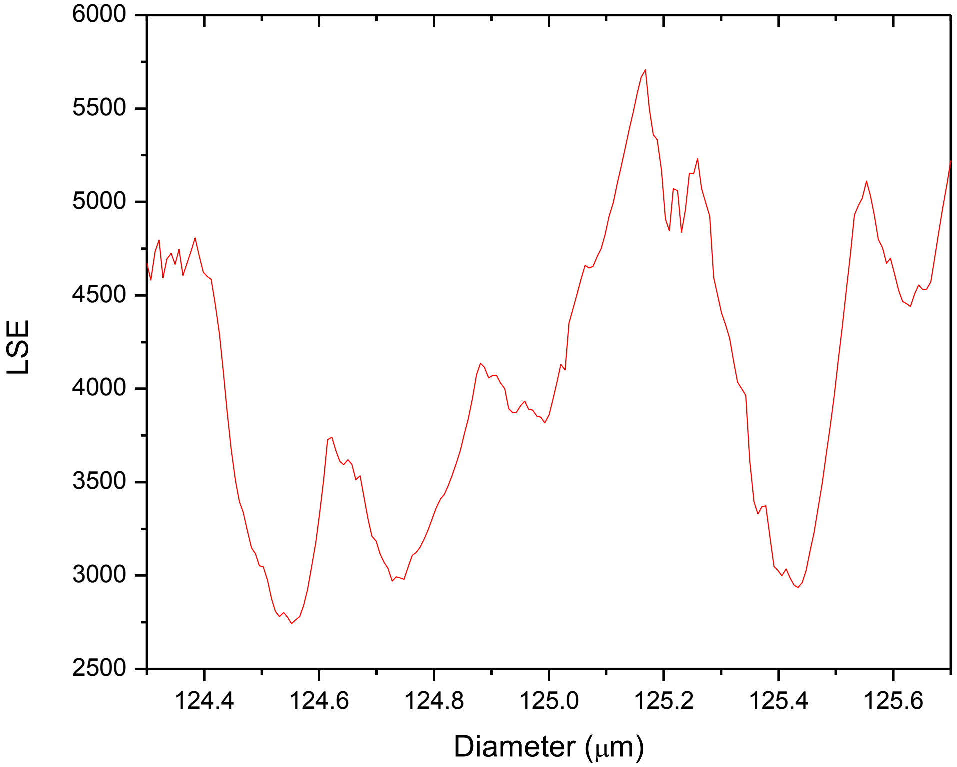

Figure 4.23: Least Square Error vs Fiber diameter plot for scattering range $10^0 – 175^0$.

Though not apparent immediately, the average difference between successive local minima is ~ 0.2 um in Figure 4.23, similar to that for bare fiber using backscattering (Figure 4.13). The local root (n_2, *t*) at each of these minima along diameter axis is given in Table 8 along with corresponding LSE.

Table 8: Root ($2r_1$, n_2, t) for 3D search using scattering data $10^0 – 175^0$.

$2r_1$ Core Diameter [μm]	n_2 (Film RI)	t [μm] (Film Thickness)	LSE
124.55	2.28	0.675	2743
124.73	2.42	0.774	2971
124.99	2.24	0.825	3816
125.23	2.78	0.675	4838
125.43	2.28	0.675	2936
125.63	2.52	0.741	4440

If guided solely by the LSE, the root should be (n_2, t) = (2.28, 0.675 µm). However 675 nm is at the edge of the search window t x n_2 while according to SEM based calibration, we expect a thickness around 750 nm. For a more detailed analysis, 2D t x n_2 error plots for the 6 local minima are shown in Figure 4.24. Each plot has a red dot located at the LSE for that particular plot.

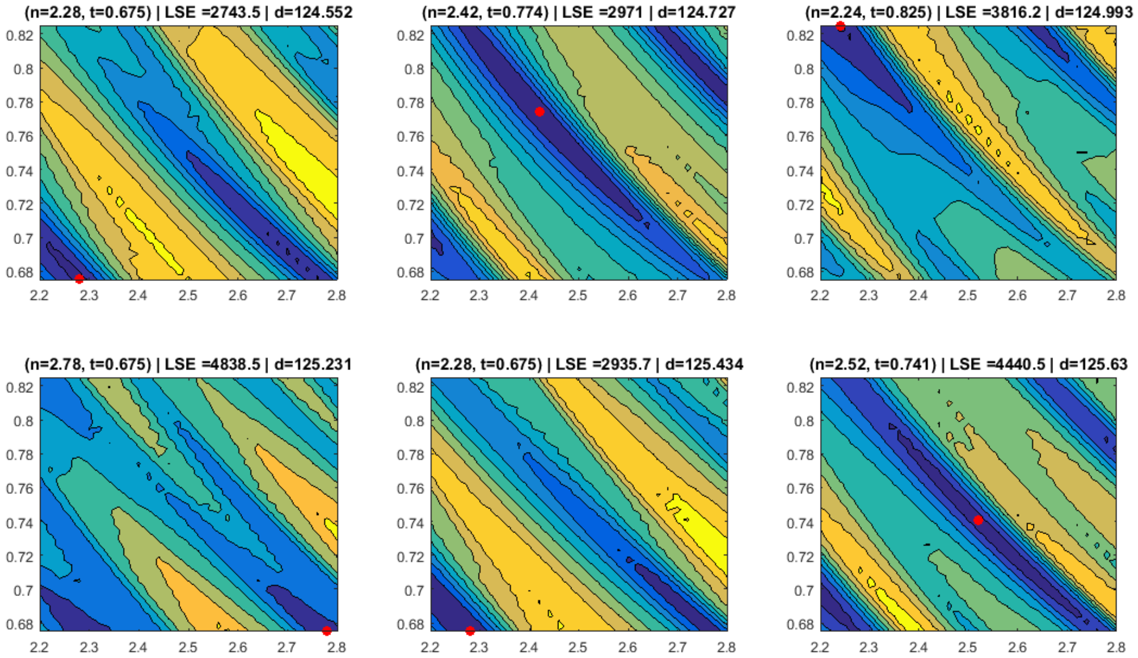

Figure 4.24: 2D error plots of (t x n_2) for each local minimum along the 3rd dimension of fiber diameter.

Of all the 6 plots, those with the red dot located at any edge of 2D search space can be discarded immediately. Thus roots with LSE = {2971, 4440} are the possible candidates. Out of these, 4440 can be rejected for 2 reasons: (a) LSE is significantly higher (b) lies at the edge of 3rd dimension – fiber diameter (close to 125.7 µm). Therefore the root ($2r_1$, n_2, t) = (124.73 µm, 2.42, 774 nm). Table 9 summarizes this analysis.

Table 9: Root ($2r_1$, n_2, t) for 3D search using scattering data 10^0 – 175^0.

$2r_1$ Core Diameter [µm]	n_2 (Film RI)	t [µm] (Film Thickness)	LSE	Accept/Reject	Reason
124.55	2.28	~~0.675~~	2743	Reject	*t* at lower edge
124.73	**2.42**	**0.774**	2971	Accept	
124.99	2.24	~~0.825~~	3816	Reject	*t* at upper edge
125.23	2.78	~~0.675~~	4838	Reject	*t* at lower edge
125.43	2.28	~~0.675~~	2936	Reject	*t* at lower edge
~~125.63~~	2.52	0.741	4440	Reject	$2r_1$ at higher edge

In conclusion, using scattering pattern from 10° – 175° is also not an independent method and needs information on thickness. Additionally, one cannot use global minimum. Valleys of minima occur along the diameter axis (period ~ 200 nm) as well as in *n* x *t* plots using entire scattering and area normalization. Pattern is too intricate to match well given imperfections deviating scattering from ideal theory for perfectly circular/concentric fiber.

CHAPTER 5 MIE SCATTERING OF BRAGG FIBERS

5.1 Introduction

Analysis of scattering of multilayered particles is of great interest for both military and civil applications. Scattering manipulation by designer particles for invisibility through scattering suppression [38] and mimicking that of another scatterer, is being studied extensively. Some theoretical efforts to improve our understanding of scattering from multilayered spheres include work of Liang et al. [39, 40], in which Mie scattering of Bragg onion resonators was investigated and Whispering Gallery Modes of the resonator were mapped to a peculiar scattering behavior. In another theoretical work on scattering of Bragg spheres [41], enhancement in backward to forward scattering ratio for large core spheres was reported. In this chapter, its cylindrical counterpart, a Bragg fiber, traditionally used for transmission, is studied as a scatterer both theoretically and experimentally. Scattering patterns were obtained for the Bragg fibers fabricated in PECVD. Peculiar features very different from that of bare fiber scattering were observed and a model was developed to explain these features.

Section 5.2 presents the experimental scattering data of Bragg fibers ZN4 and ZN5 followed by a model based on ray-tracing and scattering intensity in Section 5.3. A new scattering angle diagram based on this is presented in Section 5.4. Scattering pattern of bare fiber and Bragg fibers for both TE and TM polarizations is explained qualitatively with the help of these diagram.

5.2 Experimental Data

Scattering data collected for Bragg fibers ZN4 and ZN5 are shown in polar plots of Figure 5.1. Black plots are for TM polarization while blue for TE. Note that the pattern of

ZN4 (b) resembles that of bare fiber in Figure 4.22, reproduced in (a) for reference, with a dominant forward scattering lobe and tail like backscattering. However the forward scattering lobe is periodically spiky unlike the smooth lobe of bare fiber. The spikes are shallower for TE polarization. In contrast to the pattern of ZN4, ZN5 (c) exhibits drastic difference with scattering in the otherwise dead zone of the bare fiber and suppression in some regions of forward scattering. Pattern from a different point along the fiber axis of ZN5 (d) in the vicinity of that used for (c) is modified slightly while that taken from far away point (e) on the fiber that was closer to the chuck holding the fiber during deposition, is more like bare fiber though with apparent differences. The same spot probed with 532 nm laser instead of HeNe, shows quite a significant difference between the two polarizations (f). In the following sections, a model is developed to investigate origin of these difference.

TM	TE
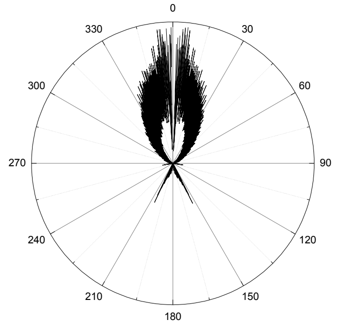	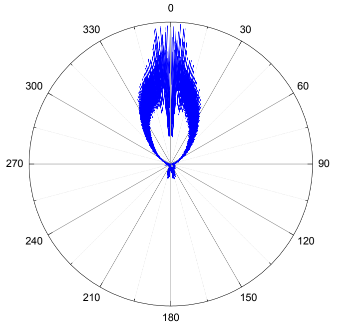
(a) SMF28e+ | λ = 632.8 nm	
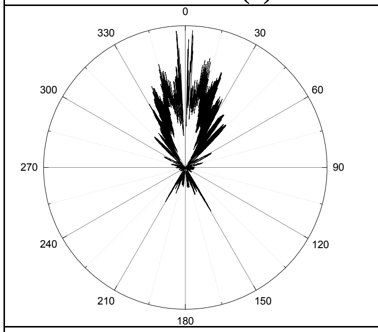	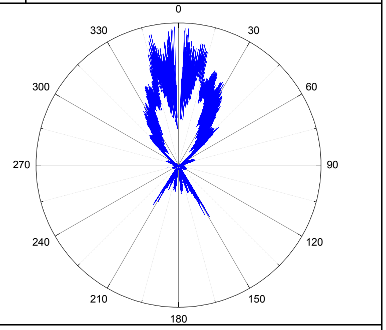
(b) ZN4 | λ = 632.8 nm	

Figure 5.1, continued

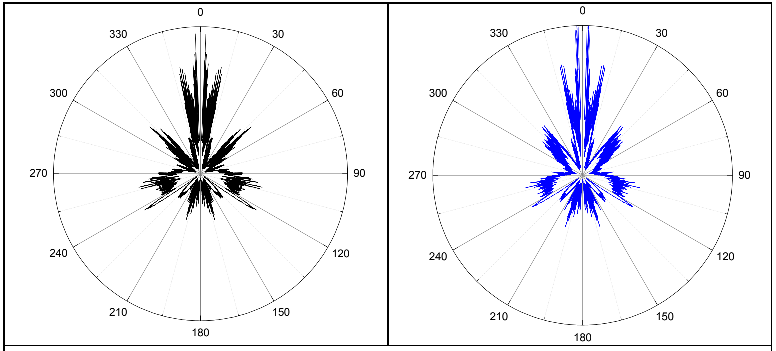

(c) ZN5 | $\lambda = 632.8$ nm

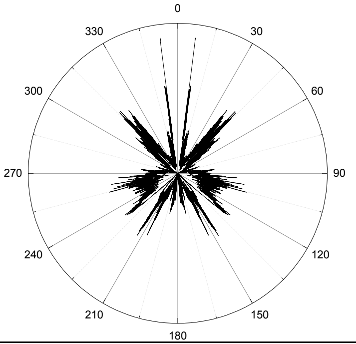

(d) ZN5 | $\lambda = 632.8$ nm | TM

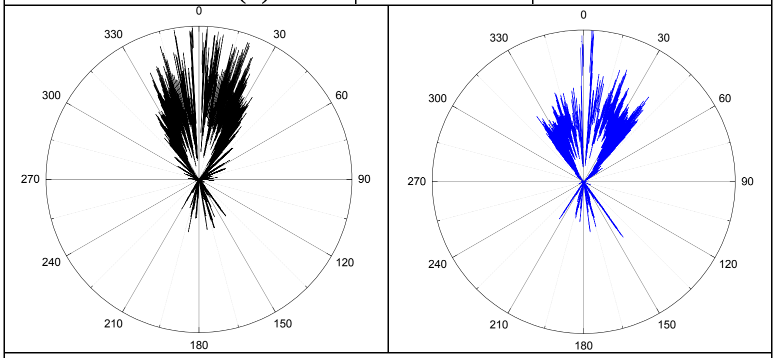

(e) ZN5 | $\lambda = 632.8$ nm | Close to chuck

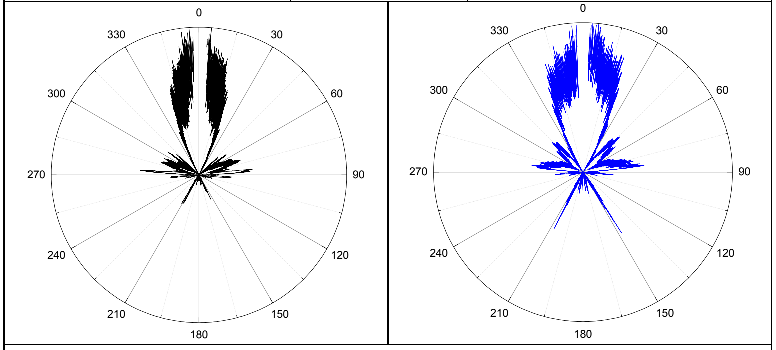

(f) ZN5 | $\lambda = 532$ nm | Close to chuck

Figure 5.1: Polar scattering plots for Bragg Fibers.

5.3 Theory and Comparison to Experimental Data

The scattering patterns at first glance seem complicated with high frequency fringes. However the broader profile of the pattern is simpler to analyze and contains significant information. To facilitate analysis, scattering data spread out in an XY graph format are shown in Figure 5.2 for a bare and Bragg fiber. The left and right columns correspond to TM (E || to fiber axis) and TE (E $\perp$ to fiber axis) polarizations respectively. The intensity on Y axis has been truncated to make the intricate pattern visible.

Bare fiber patterns (Figure 5.2 (a) and (b)) exhibit well-defined regions of forward and backscattering separated by a wide dark zone of negligible scattering intensity. The forward scattering decreases monotonically with scattering angle, while backscattering appears as a sudden increase in intensity after the dark zone. Patterns for the two polarizations differ in the sharpness of transition from dark zone to backscattering. TM is sharper than TE. Origin of these differences will be explained later.

In contrast to the bare fiber, data of the Bragg Fiber ZN5 (Figure 5.2 (c) and (d)) is apparently chaotic with no distinct forward and backscattering regions. The main distinctive features in these patterns are: 1) notches followed by drastic suppression in forward scattering in the band of 0^0 – 40^0, 2) enhanced scattering in the otherwise dark zone of bare fiber, 3) a bump between 130^0-150^0 4) modified backscattering and 5) narrow dip in scattering around 130^0.

To explain the origin of these features in Bragg Fiber scattering as well as the difference between patterns of the two polarizations, we first characterized the film properties by fitting method like in CHAPTER 4. However due to high number of concentric cylinders, best-fit pattern was found manually as the unique pattern of Bragg

Fiber made the search easier.

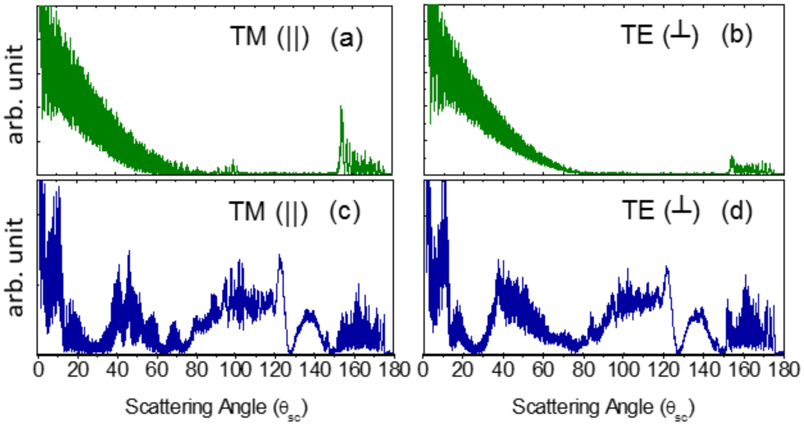

Figure 5.2: Scattering data for TM (left) and TE (right) polarizations for bare (green) and Bragg Fiber ZN5 (blue).

For Bragg fibers, the theoretical scattering pattern is not very sensitive to variation in core diameter and terminal layer thickness (Figure 5.3) except for minor differences. Therefore to reduce the search parameters, core diameter was fixed at 200 µm and terminal layer thickness to 1 µm, respectively, during the fitting.

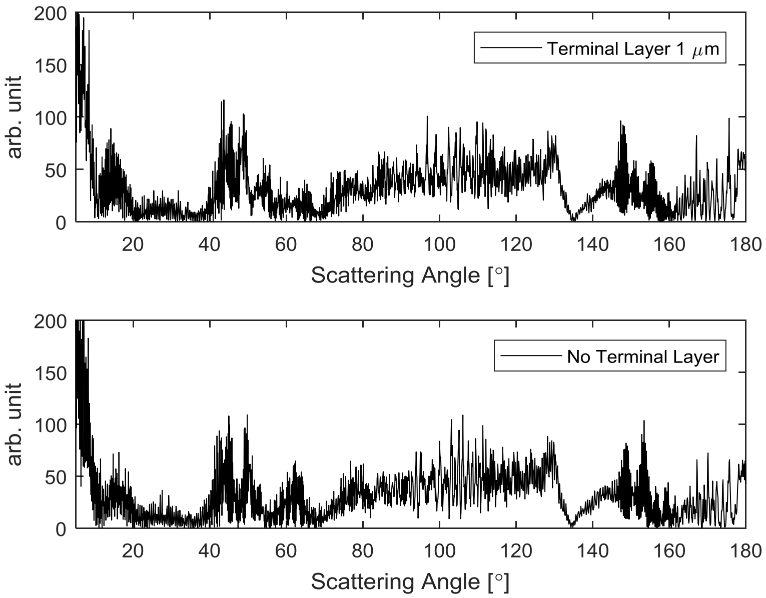

Figure 5.3: Effect of terminal layer on scattering of TM polarized HeNe from Bragg fiber assuming 12 pairs of SiN_x and SiO_2 with thicknesses 165 nm and 375 nm respectively while indexes assumed to be 2.49 and 1.6 respectively.

The best fit patterns obtainable by manual search shown in Figure 5.4 (b) and (d), match with the overall profile of experimental data in Figure 5.4 (a) and (c) reasonably well. The best-fitted layer thicknesses for SiN_x and SiO_2 are 166 nm and 375 nm, respectively, which are within the error bar of SEM based growth rate calibration curve [25]. The best fit refractive index values for SiN_x and SiO_2 are 2.495 and 1.608, respectively. These values will be used for theoretical investigation of the origin of these scattering patterns.

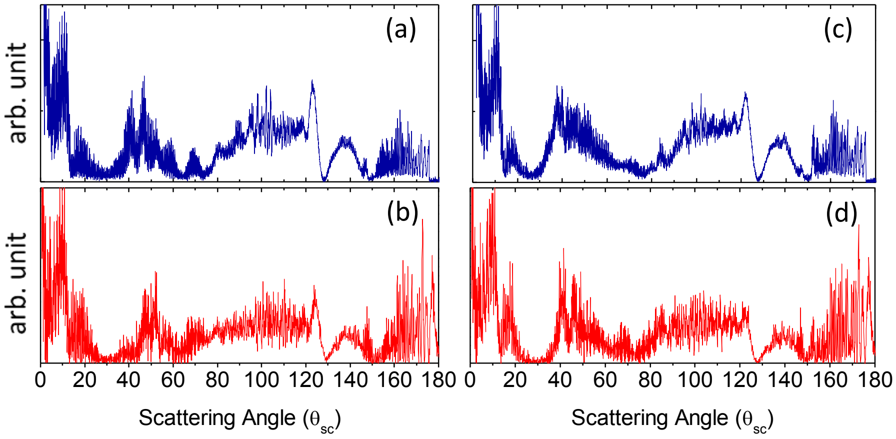

Figure 5.4: Experiment (blue) vs theoretical fit (red) for ZN5. (Left) TM; (Right) TE.

5.4 Scattering Angle Diagram

Now we develop a scattering angle (θ_{sc}) vs incidence angle (θ_{in}) diagram using ray tracing. Consider the partial ray diagram for the circular cross section in Figure 5.5. A pencil of rays is incident on the cross section normal to the fiber axis and reflects (blue) and transmits (green) through the circle obeying laws of reflection and refraction. Incidence angle of each ray depends on the lateral location from the central axis (black). The ray incident head on has $\theta_{in} = 0$ while that displaced from the center by radius has $\theta_{in} = 90^o$. Thus incidence angle of any ray in the bundle lies in the range $[0^0, 90^0]$ with respect to local normal at the air-fiber interface.

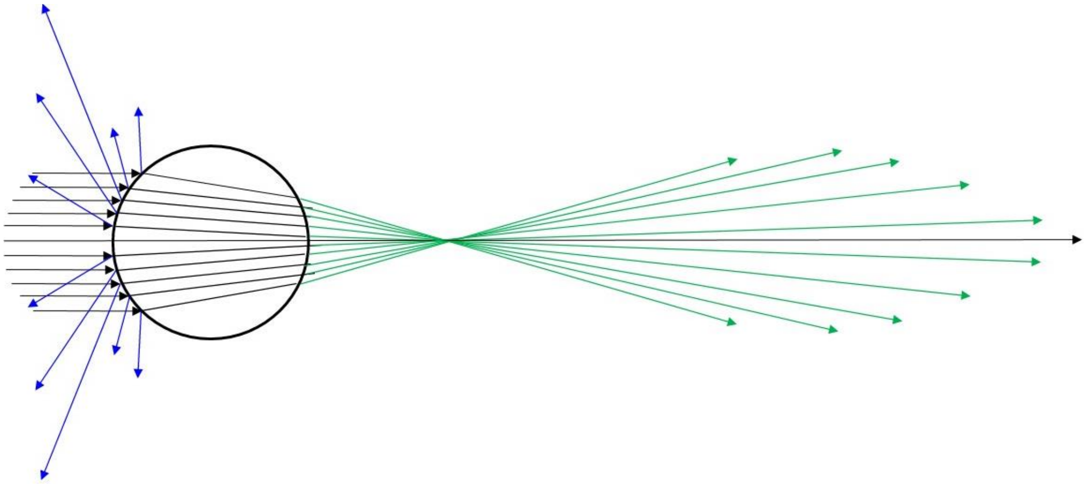

Figure 5.5: Ray diagram through fiber cross section showing only reflected and transmitted rays.

Out of the infinite scattered rays generated by a given incident ray, only the first three (Figure 5.7 (a)), marked as ray 1, 2, 3 at 1st, 2nd and 3rd interface respectively are considered. Scattering angle $\theta_{sc}^{(i)}$ of ray *i* is measured from the incidence direction and is given by

$$\theta_{sc}^{(1)} = 180 - 2\theta_{in}, \tag{5.1}$$

$$\theta_{sc}^{(2)} = 2\left(\theta_{in} - \theta_r\right), \tag{5.2}$$

$$\theta_{sc}^{(3)} = 180 + 2\theta_{in} - 4\theta_r \tag{5.3}$$

for each ray. Here θ_r is the refraction angle. The scattering angle diagram for the 3 rays as a function of incidence angle is plotted in Figure 5.7 (b). From this diagram it is easy to read out the rays contributing at a given scattering angle. Region of scattering angle 0^0 – 100^0 receives rays 1 with θ_{in} between ~50^0 – 90^0 and rays 2 with θ_{in} from 0^0 – 90^0, while $\theta_{sc} \in (100^0 – 150^0)$ receives only rays 1 with θ_{in} roughly between 17^0 – 40^0. Backscattering range 150^0 – 180^0 is formed by superposition of rays 1 and rays 3. Rays 3 with at least two incidence angles contribute at a given scattering angle, a point missed by Presby [30] but later corrected by Marcuse [42], elucidating the utility of these plots. Note the wrapping of the curve of ray 3 beyond $\theta_{in} \sim 85^0$ where θ_{sc} reaches 180^0. This cross-over incidence angle is inversely proportional to RI of fiber. Ray diagram in Figure 5.6 elucidates the cases where scattering angles is less or greater than 180^0.

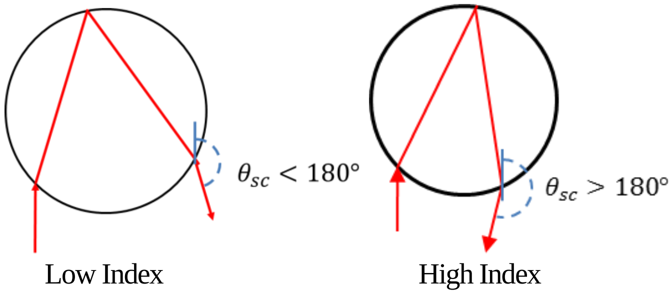

Figure 5.6: Scattering angle can exceed 180^0 for high refractive index.

This diagram is independent of radius of the fiber but depends on the refractive index. The curve of rays 3 as well as rays 2 depends on the index. The minimum θ_{sc} for rays 3 also called the cut-off angle, was used to characterize fiber index by Presby. The information about the fiber diameter is contained in interference between these rays. The separation between fringes was used to find the diameter of the fiber in [43]. However the matter at hand is scattering intensity distribution as a function of scattering angle. Neglecting interference, we simply include the information of intensity of each ray. We know from Fresnel reflection coefficients, that intensity I of the rays depends on θ_{in} and the number of interfaces on their trajectory. If $R_{af}(\theta_{in})$ is the angular reflectance of air-fiber interface, the scattering intensity of the three types of rays is as follows:

$$\begin{gathered} I_1 \propto R_{af}(\theta_{in}), \\ I_2 \propto \left(1-R_{af}(\theta_{in})\right)\left(1-R_{fa}(\theta_r)\right), \\ I_3 \propto \left(1-R_{af}(\theta_{in})\right)R_{fa}(\theta_r)\left(1-R_{fa}(\theta_r)\right). \end{gathered} \tag{5.4}$$

Here the subscript *af* and *fa* mean air-fiber and fiber-air respectively. Due to reciprocity of the system, $R_{af} = R_{fa} = R$ and equations 5.4 reduce to the following:

$$\begin{aligned} I_1 &\propto R(\theta_{in}), \\ I_2 &\propto \left(1-R(\theta_{in})\right)^2, \\ I_3 &\propto R(\theta_{in})\left(1-R(\theta_{in})\right)^2. \end{aligned} \tag{5.5}$$

We will augment the scattering angle diagram in Figure 5.7 (b) with the intensity information by making line thicknesses of rays 1 – 3 proportional to I_1, I_2 and I_3 respectively resulting in augmented scattering angle diagrams discussed in next sections for bare and Bragg fibers.

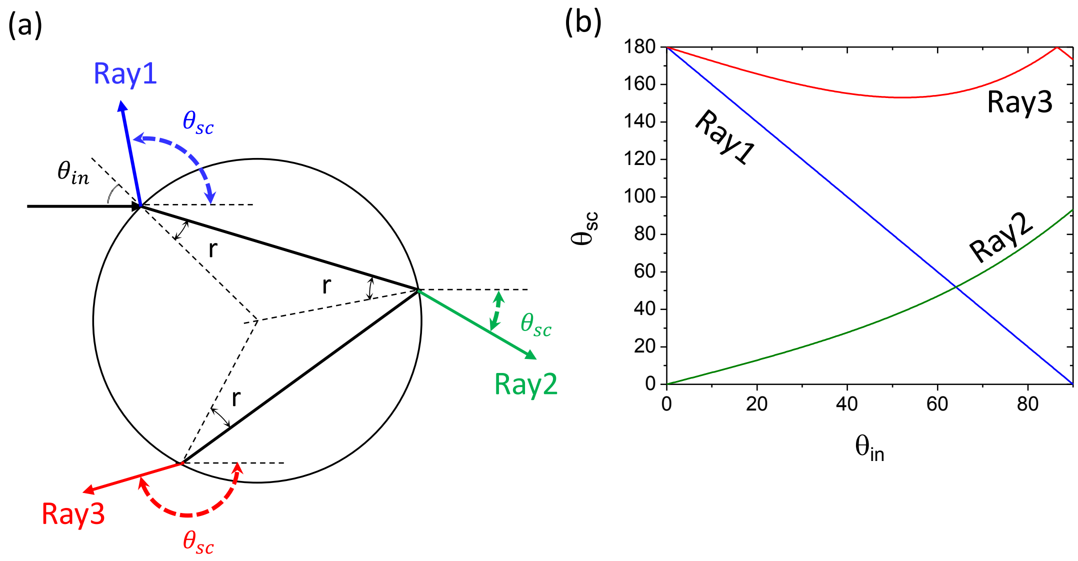

Figure 5.7: Ray diagram and corresponding scattering angle diagram.

5.4.1 Augmented Scattering Angle Diagram for Bare Fiber

We first consider diagram for bare fiber. Figure 5.8 shows augmented scattering angle diagram for a bare fiber for TM polarization on the left with reflectance $R(\theta_{in})$ plotted below θ_{in} axis and scattering signature of the bare fiber beside the θ_{sc} axis. From the line thicknesses of θ_{sc} vs θ_{in} diagram the origin of characteristics of forward-scattering, back-scattering and dead-zone become evident. For θ_{sc} ϵ (0,100), strongly scattered rays 1 at grazing incidence interfere with strong near-normally incident rays 2 that monotonically decrease in intensity (width of green line i.e. ray 2 is decreasing with incidence angle). This band forms the dominant forward scattering of bare fiber that reduces in intensity with scattering angle. For $\theta_{sc} \epsilon$ (100, 150) – the dead zone, only contribution is from the weakly scattered rays 1. Lastly, $\theta_{sc} \epsilon$ (150, 180) is the well-known backscattering region where only weak ray1 and ray3 contribute. Since the rays 3 are weakest due to 3 bounces, the line thickness has been scaled up 4 times relative to other 2 curves. Note that the minimum of ray3 curve at about θ_{sc} = 150 agrees well with the backscattering cutoff angle of the experimental data along the Y axis. A similar plot for TE polarization shown on the right, visualizes the effect of Brewster's angle clarifying the reason for difference in backscattering cut off.

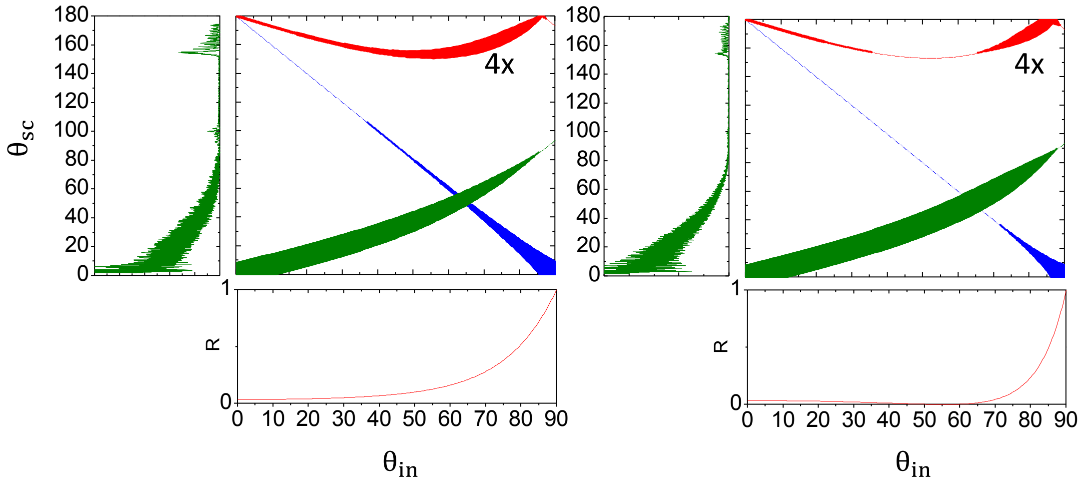

TM Polarization

TE Polarization

Figure 5.8: Augmented scattering angle diagrams of bare fiber for TM (left) and TE (right) polarizations. Red curve thickness has been scaled 4 times for visibility.

5.4.2 Augmented Scattering Angle Diagram for Bragg Fiber

Now we are ready to create augmented scattering angle diagram for Bragg fiber and understand its bizarre pattern. Two assumptions are made in this analysis for Bragg fiber. Firstly, since the thickness of the Bragg layer is much smaller than the core radius, we neglect its thickness for ray tracing and therefore the skeleton of the diagram remains the same as in Figure 5.7 and assume that the presence of the Bragg layer modifies only the local reflectance/transmittance at the air-fiber interface. Secondly, since the ratio of fiber diameter and wavelength (200/0.633) is very large, the Bragg layers can be assumed to be locally planar. The reflectance from the layers for the two polarizations can be calculated using best fit values obtained resulting in diagrams in Figure 5.9.

The presence of the wide stopband in reflectance curve, immediately explains the bizarre signature of the Bragg fiber. Stopband blocks corresponding incident rays from entering the fiber stripping a portion of forward scattering. These rays reflected with R=1 appear in otherwise dead zone of bare fiber. To facilitate understanding, dashed lines are drawn on the figure as eye guides while shaded bands have been drawn on the θ_{in} and θ_{sc} axes to trace the effect of stopband (hatched) and first reflectance peak (gray). Note the suppression of green (rays 2) leads to suppressed forward scattering while enhancement of blue (rays 1) curve leads to complementary enhancement of scattering, both marked with hatched shading and are due to complete stopband. Similar pair of suppression and enhancement can be observed arising from first reflectance peak highlighted traced by gray shading which is narrower and has R<1. Being narrower, it suppresses/enhances only narrow portions of scattering as depicted by gray shaded area on the θ_{sc} axis. The dip in reflectance curve lying between 20 – 30 degrees traces to spike around $\theta_{sc} = 19^{o}$ and dip at 130^{o}. Note that even though red curve (rays 3) is suppressed due to stopband, there is no significant effect of this on scattering intensity because it is not a monotonic curve. Therefore scattering arising from rays with incidence angles outside stopband, make up for the suppression.

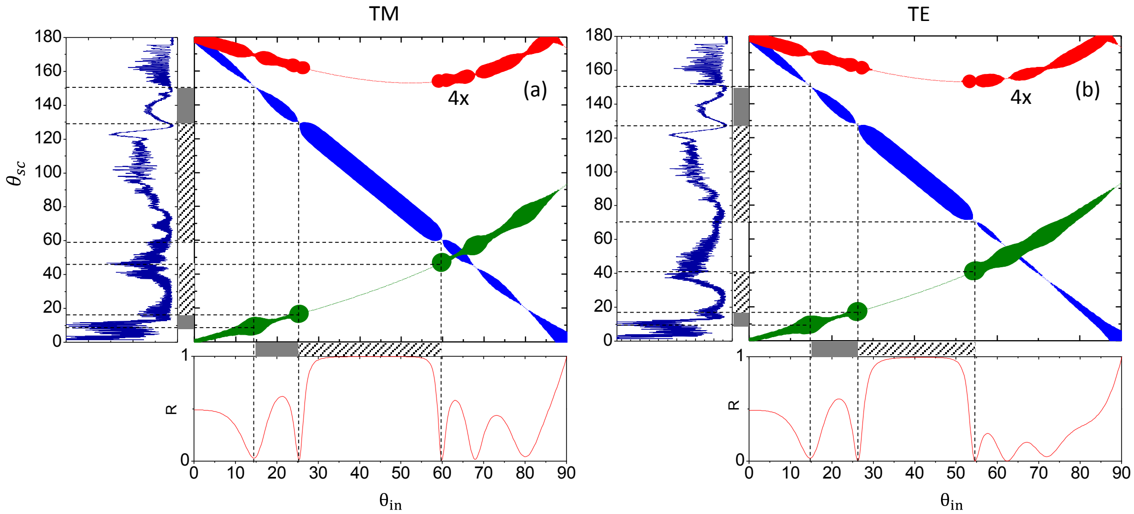

Figure 5.9: Scattering Angle Diagrams to explain Photonic Bandgap effect in Bragg Fiber ZN5. (a) TM, (b) TE.

This analysis shows that scattering can be manipulated by controlling stopband width and location. Enhancement and suppression of scattering at various angular ranges can be achieved thus. This is illustrated for several Bragg fibers in Figure 5.10. In particular, a wide stopband starting from zero degree can lead to enhanced backscattering as shown in first polar plot of Figure 5.10.

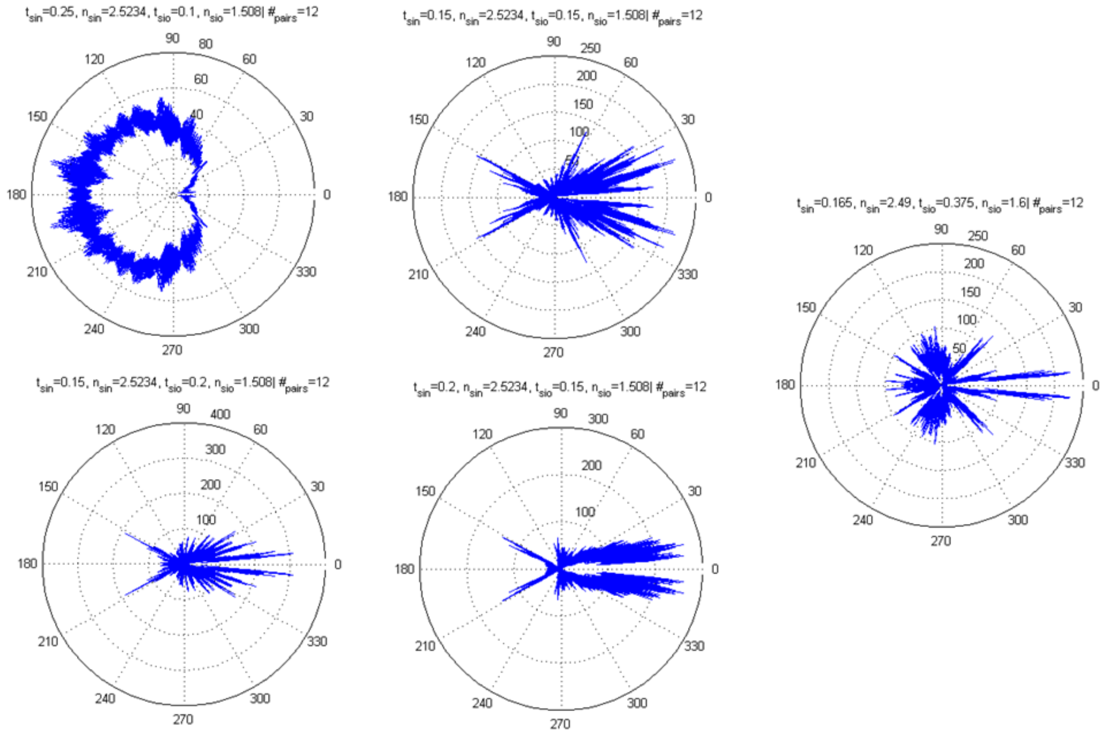

t_{sin}=0.25, n_{sin}=2.5234, t_{sio}=0.1, n_{sio}=1.508| $\#_{pairs}$=12

t_{sin}=0.15, n_{sin}=2.5234, t_{sio}=0.15, n_{sio}=1.508| $\#_{pairs}$=12

t_{sin}=0.165, n_{sin}=2.49, t_{sio}=0.375, n_{sio}=1.6| $\#_{pairs}$=12

t_{sin}=0.15, n_{sin}=2.5234, t_{sio}=0.2, n_{sio}=1.508| $\#_{pairs}$=12

t_{sin}=0.2, n_{sin}=2.5234, t_{sio}=0.15, n_{sio}=1.508| $\#_{pairs}$=12

Figure 5.10: Polar scattering patterns for several Bragg fiber designs.

No stopband in the reflectance leads to pattern similar to bare fiber with a forward and backscattering region separated by dead zone. Such is the case for ZN4 as seen in Figure 5.11. The reflectance curve is similar qualitatively to that of air-glass interface, however with some ripples and hence the pattern is similar to bare fiber except with some spikes which occur due to interference in the Bragg layer in passband.

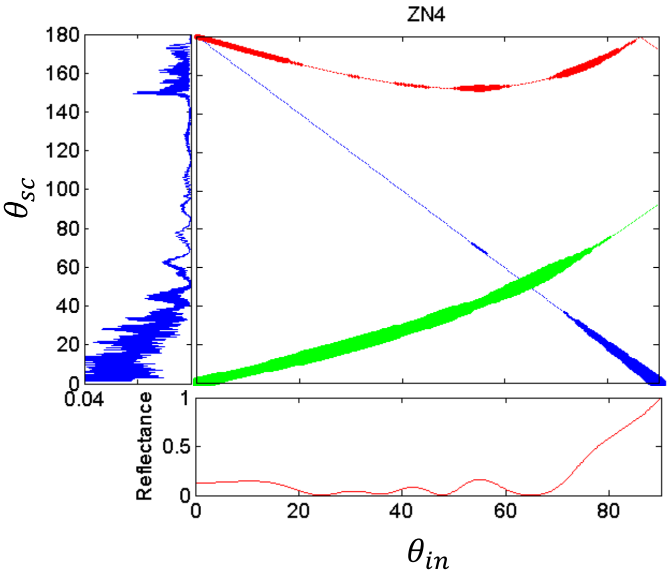

Figure 5.11: Scattering angle diagram for ZN4. Scattering data is for TM polarization. Parameters of Bragg layers are: nSiN=2.49, nSiO=1.6, tSiN=236 nm, tSiO=109 nm. Again, red curve has been scaled by a factor of 4 for visibility.

More accurate analysis can be done by including the phase of the rays in the model. Shift in the ray trajectories due to thickness of the coated Bragg layers, neglected in this study can further improve the accuracy.

CHAPTER 6 CONCLUSION AND FUTURE WORK

This work lays the foundation for coating the surface of axis-symmetric WGMRs in PECVD with layers with a wide range of refractive index, potentially expanding the capabilities of the current WGMRs in sensing, mode shaping, spectral and dispersion engineering. The fabrication method is applicable to resonators shaped out of fibers such as bottle microresonator [44] and SNAP [45] and other cylindrically symmetric geometries such as NIST's microrod resonator as demonstrated experimentally in Section 3.3.4. Microsphere at the tip of a short large-core fiber may also be coated. The Q-factors of resultant stratified WGMRs can be further improved by lowering H content of SiN_x due to NH_3 as suggested in [46] or operating away from the absorption peaks of different bonds or using N_2 instead of NH_3.

The focus of this thesis is the simplified case of axis-symmetric WGMR – an optical fiber. Fibers were coated uniformly in PECVD chamber by rotating them about axis during deposition. Single layers were deposited for characterization of the films and multiple layers for fabricating Bragg fibers – the simplest photonic bandgap fibers.

Mie scattering of single layered fibers was used to determine the refractive index and thickness of the thin films. It is concluded that characterizing thin films on fibers by scattering alone is challenging due to experimentally indistinguishable patterns periodically recurring for various combinations of film refractive index and physical dimensions of the coated fiber. Moreover, scattering is very sensitive to deviation from ideal circular geometry. Practically fibers can be elliptical, non-concentric if SMF, axially non-uniform in diameter or all factors present together. Layer coated on such a fiber adds to the challenge.

Most of the work in this dissertation employs backscattering as used in the pioneering work of Presby. However, regardless of which scattering region one uses – backscatter, forward or entire pattern, above factors add complexity to finding best fit pattern. The problem is that different angular regions of the scattering pattern may match well for different set of fiber parameters yielding same least square error. This makes it difficult to uniquely characterize the film unless additional information is available to lift the apparent degeneracy. Therefore prior knowledge of thickness from SEM was used as a ball-park to guide the root-search for film parameters in this work.

Refractive index obtained thus from scattering of fibers coated with single layer of silicon nitride with different deposition times was 2.49 for λ = 632.8nm. The experimental pattern had a remarkable correlation with theoretical pattern for n=2.49, thickness in agreement with SEM and fiber diameter within tolerance specification. Silicon nitride deposited by PECVD (a-SiN_x:H) using SiH_4/NH_3 mixture can have refractive index exceeding 2 – the typical value for stoichiometric Si_3N_4 at the same wavelength, depending on NH_3 concentration in the mixture. A 20% Ammonia concentration in NH_3/SiH_4 mixture has been reported to have RI exceeding 2.5 at 1550 nm [14]. Even though this work uses gas ratios for regular silicon nitride, other factors such as substrate temperature, fiber cycling in the chamber, affect the composition and morphology of the films changing RI as a result. The dynamic substrate cycling through the gradient of temperature can affect the sticking coefficient of the heavier Si containing radicals. If Si is retained in the film more than N compared to the case of stationary wafer, the refractive index will be high. Whether Si content has increased, can be verified by techniques such as micro-Raman or X-ray photoelectron spectroscopy.

The growth rate of silicon nitride were found higher than that on flat wafers using same recipe. This could be due to changed growth kinetics at the fiber substrate due to rotation and sample elevation.

For pure scattering based characterization, pattern should be obtained at multiple close-by wavelengths. The root will be the one with same thickness and fiber diameter at all wavelengths and approximately the same refractive index. Theoretically Mie scattering pattern of a coated fiber may be unique for a tuple of [nCore, nLayer, Core diameter, Layer thickness], however experimental errors make it non-trivial. It will be interesting to study theoretically if two coated cylinders with different values for any subset of this tuple have same scattering signature.

Further, scattering of fabricated Bragg fibers was studied and compared to that of bare fiber. Pattern is dependent on Bragg layer design. The designs with no stopband for the wavelength have pattern similar to that of bare fiber while those with a wide stopband have a radically different pattern. The location of the stopband can be used to steer the scattering suppression in different directions. With tunable PBG, the visibility at an angle may be controlled.

To use these coated fibers as WGM resonators requires axial confinement despite theoretical proofs of high Q factors in a cylinder [47]. Sustaining a WGM of high Q factor in coated fiber without axial confinement is made difficult by the intrinsic non-uniformity in commercial optical fibers which already reduces the Q factor to a few thousands. Additional trace of non-uniformity of coated layer will make it more difficult to have a WGM with respectable Q factor. Therefore, it is imperative to shape the fiber by either CO_2 laser [45] or splicer [44]or some other means before coating it, a subject of future work.

In summary, PECVD tool was adapted for the first time to coat optical fibers uniformly to make single layered and Bragg fibers. The deposited films were characterized non-invasively using Mie scattering of films coated on fibers. Additionally, first experimental data on Mie scattering of Bragg fibers has been reported, only relevant work on Bragg coatings being [39] on spheres but limited to theory. Furthermore, anomalous scattering suppression and enhancement from Bragg fiber has been demonstrated and explained, which can be controlled by the design of the Bragg layers. A change in the PBG of the Bragg layers would change the scattering pattern. Backward to forward scattering ratio can also be drastically increased for wide stopband designs as predicted by numerical results. Further, a method for depositing films with speed-dependent refractive index has been introduced. It would be interesting to investigate the chemical composition of the film as a function of rotation speed of the fiber in PECVD to better understand the modified growth kinetics.

REFERENCES

[1] L. G. Guimaraes and H. M. Nussenzveig, "THEORY OF MIE RESONANCES AND RIPPLE FLUCTUATIONS," *Optics Communications,* vol. 89, pp. 363-369, May 1992.

[2] B. R. Johnson, "Theory of morphology-dependent resonances: shape resonances and width formulas," *Journal of the Optical Society of America A,* vol. 10, pp. 343-352, 1993/02/01 1993.

[3] *Practical Applications of Microresonators in Optics and Photonics* vol. 146. Boca Raton: Crc Press-Taylor & Francis Group, 2009.

[4] R. Yang, A. Yun, Y. Zhang, and X. Pu, "Quantum theory of whispering gallery modes in a cylindrical optical microcavity," *Optik - International Journal for Light and Electron Optics,* vol. 122, pp. 900-909, 2011/05/01/ 2011.

[5] I. Teraoka and S. Arnold, "Enhancing the sensitivity of a whispering-gallery mode microsphere sensor by a high-refractive-index surface layer," *Journal of the Optical Society of America B,* vol. 23, pp. 1434-1441, 2006/07/01 2006.

[6] D. Zhu, Y. Zhou, X. Yu, P. Shum, and F. Luan, "Radially graded index whispering gallery mode resonator for penetration enhancement," *Optics Express,* vol. 20, pp. 26285-26291, 2012/11/19 2012.

[7] V. S. Ilchenko, A. A. Savchenkov, A. B. Matsko, and L. Maleki, "Dispersion compensation in whispering-gallery modes," *Journal of the Optical Society of America A,* vol. 20, pp. 157-162, 2003/01/01 2003.

[8] I. Teraoka and S. Arnold, "Coupled whispering gallery modes in a multilayer-coated microsphere," *Optics Letters,* vol. 32, pp. 1147-1149, 2007/05/01 2007.

[9] A. Yariv, Y. Xu, R. K. Lee, and A. Scherer, "Coupled-resonator optical waveguide:?a proposal and analysis," *Optics Letters,* vol. 24, pp. 711-713, 1999/06/01 1999.

[10] J. Scheuer and A. Yariv, "Sagnac Effect in Coupled-Resonator Slow-Light Waveguide Structures," *Physical Review Letters,* vol. 96, p. 053901, 02/06/ 2006.

[11] E. Guillermain, V. Lysenko, R. Orobtchouk, T. Benyattou, S. Roux, A. Pillonnet, *et al.*, "Bragg surface wave device based on porous silicon and its application for sensing," *Applied Physics Letters,* vol. 90, p. 241116, 2007.

[12] P. Yeh, A. Yariv, and A. Y. Cho, "Optical surface waves in periodic layered media," *Applied Physics Letters,* vol. 32, pp. 104-105, 1978.

[13] D. Ristić, A. Chiappini, M. Mazzola, D. Farnesi, G. Nunzi-Conti, G. C. Righini, *et al.*, "Whispering gallery mode profiles in a coated microsphere," *The European Physical Journal Special Topics,* vol. 223, pp. 1959-1969, 2014/09/01 2014.

[14] W. Qiu, Y. M. Kang, and L. L. Goddard, "Quasicontinuous refractive index tailoring of SiNx and SiOxNy for broadband antireflective coatings," *Applied Physics Letters,* vol. 96, p. 141116, 2010.

[15] L. Prkna, J. Čtyroký, and M. Hubálek, "Ring microresonator as a photonic structure with complex eigenfrequency," *Optical and Quantum Electronics,* vol. 36, pp. 259-269, 2004// 2004.

[16] S. D. Hart, G. R. Maskaly, B. Temelkuran, P. H. Prideaux, J. D. Joannopoulos, and Y. Fink, "External Reflection from Omnidirectional Dielectric Mirror Fibers," *Science,* vol. 296, p. 510, 2002.

[17] T. Katagiri, Y. Matsuura, and M. Miyagi, "Photonic bandgap fiber with a silica core and multilayer dielectric cladding," *Optics Letters,* vol. 29, pp. 557-559, 2004/03/15 2004.

[18] S. Jacques, H. Vincent, C. Vincent, A. Lopez-Marure, and J. Bouix, "Multilayered BN Coatings Processed by a Continuous LPCVD Treatment onto Hi-Nicalon Fibers," *Journal of Solid State Chemistry,* vol. 162, pp. 358-363, 2001/12/01 2001.

[19] G. R. Hadley, J. G. Fleming, and S.-Y. Lin, "Bragg fiber design for linear polarization," *Optics Letters,* vol. 29, pp. 809-811, 2004/04/15 2004.

[20] S. Chaudhuri, J. Sparks, R. He, and J. Badding, "Hollow Core Silicon-Silica Bragg Fiber," in *CLEO: 2015,* San Jose, California, 2015, p. STu1N.5.

[21] J. C. Knights, R. A. Lujan, M. P. Rosenblum, R. A. Street, D. K. Bieglesen, and J. A. Reimer, "Effects of inert gas dilution of silane on plasma ‐ deposited a ‐ Si:H films," *Applied Physics Letters,* vol. 38, pp. 331-333, 1981/03/01 1981.

[22] L. Zhao, 2011.

[23] B. Michalak, M. Koba, and M. Smietana, "Silicon Nitride Overlays Deposited on Optical Fibers with RF PECVD Method for Sensing Applications: Overlay Uniformity Aspects," *Acta Physica Polonica A*, vol. 127, pp. 1587-1590, Jun 2015.

[24] K. R. Williams, K. Gupta, and M. Wasilik, "Etch Rates for Micromachining ProcessingPart II," *Journal of Microelectromechanical Systems,* vol. 12, 2003.

[25] M. Green, Z. Naqvi, K. Smith, and T. H. Her, "Fabrication and characterization of uniform conformal thin films of SiO<inf>2</inf> and SiN<inf>x</inf> on optical fibers," in *2014 11th Annual High Capacity Optical Networks and Emerging/Enabling Technologies (Photonics for Energy)*, 2014, pp. 229-233.

[26] Del, apos, P. Haye, S. A. Diddams, and S. B. Papp, "Laser-machined ultra-high-Q microrod resonators for nonlinear optics," *Applied Physics Letters,* vol. 102, p. 221119, 2013.

[27] Accurion, "The next generation in imaging ellipsometry: nanofilm_ep4," 2017.

[28] S. Munteanu, N. Garraud, J. P. Roger, F. Amiot, J. Shi, Y. Chen*, et al.*, "In Situ, Real Time Monitoring of Surface Transformation: Ellipsometric Microscopy Imaging of Electrografting at Microstructured Gold Surfaces," *Analytical Chemistry,* vol. 85, pp. 1965-1971, 2013/02/19 2013.

[29] Christian Negara, "Thickness Measurement of Thin Films on Curved Surfaces with Ellipsometry," 2014.

[30] H. M. Presby, "Refractive index and diameter measurements of unclad optical fibers," *Journal of the Optical Society of America,* vol. 64, pp. 280-284, 1974/03/01 1974.

[31] F. Tajima, Y. Nishiyama, N. Hiroi, and Y. Hashimoto, "Standard optical coaxial double fiber diameter and refractive index measurement, accuracy, and precision

using light scattering at normal incidence," *Journal of the Optical Society of America A,* vol. 27, pp. 1-5, 2010/01/01 2010.

[32] M. Kerker and E. Matijević, "Scattering of Electromagnetic Waves from Concentric Infinite Cylinders*," *Journal of the Optical Society of America*, vol. 51, pp. 506-508, 1961/05/01 1961.

[33] M. Kerker, "The Scattering Light and Other Electrmagnetic Radiation," 1969.

[34] J.-P. Schaefer, "Implementierung und Anwendung analytischer und numerischer Verfahren zur Lösung der Maxwellgleichungen für die Untersuchung der Lichtausbreitung in biologischem Gewebe. Open Access Repositorium der Universität Ulm. Dissertation. ," PhD, Ulm, 2011.

[35] Thorlabs, "Step-Index, Multimode Fiber."

[36] D. Marcuse and H. M. Presby, "Light scattering from optical fibers with arbitrary refractive-index distributions," *Journal of the Optical Society of America,* vol. 65, pp. 367-375, 1975/04/01 1975.

[37] Z. Naqvi, M. Green, C. Wang, and T.-H. Her, "Characterization of Bragg Fibers by Mie scattering," in *Conference on Lasers and Electro-Optics*, San Jose, California, 2016, p. JTu5A.112.

[38] A. Mirzaei, A. E. Miroshnichenko, I. V. Shadrivov, and Y. S. Kivshar, "All-Dielectric Multilayer Cylindrical Structures for Invisibility Cloaking," *Scientific Reports,* vol. 5, p. 9574, 04/10

[39] W. Liang, Y. Xu, Y. Huang, A. Yariv, J. G. Fleming, and S.-Y. Lin, "Mie scattering analysis of spherical Bragg "onion" resonators," *Optics Express,* vol. 12, pp. 657-669, 2004/02/23 2004.

[40] Y. Xu, W. Liang, A. Yariv, J. G. Fleming, and S.-Y. Lin, "Modal analysis of Bragg onion resonators," *Optics Letters,* vol. 29, pp. 424-426, 2004/03/01 2004.

[41] D. D. Smith and K. A. Fuller, "Photonic bandgaps in Mie scattering by concentrically stratified spheres," *Journal of the Optical Society of America B,* vol. 19, pp. 2449-2455, 2002/10/01 2002.

[42] D. Marcuse, "Light scattering from unclad fibers: ray theory," *Applied Optics,* vol. 14, pp. 1528-1532, 1975/07/01 1975.

[43] H. M. Presby and D. Marcuse, "Refractive Index and Diameter Determinations of Step Index Optical Fibers and Preforms," *Applied Optics,* vol. 13, pp. 2882-2885, 1974/12/01 1974.

[44] G. S. Murugan, J. S. Wilkinson, and M. N. Zervas, "Selective excitation of whispering gallery modes in a novel bottle microresonator," *Optics Express,* vol. 17, pp. 11916-11925, 2009/07/06 2009.

[45] M. Sumetsky and J. M. Fini, "Surface nanoscale axial photonics," *Optics Express,* vol. 19, pp. 26470-26485, 2011/12/19 2011.

[46] H. Albers, L. T. N. Hilderink, E. Szilagyi, F. Paszti, P. V. Lambeck, and T. J. A. Popma, "Reduction of hydrogen induced losses in PECVD-SiO_xN_y optical waveguides in the near infrared," in *Lasers and Electro-Optics Society Annual Meeting, 1995. 8th Annual Meeting Conference Proceedings, Volume 1., IEEE,* 1995, pp. 88-89 vol.2.

[47] M. Sumetsky, "Mode localization and the Q-factor of a cylindrical microresonator," *Optics Letters,* vol. 35, pp. 2385-2387, 2010/07/15 2010.

[48] T. Karabacak, Y. P. Zhao, G. C. Wang, and T. M. Lu, "Growth front roughening in silicon nitride films by plasma-enhanced chemical vapor deposition," *Physical Review B,* vol. 66, p. 075329, 08/22/ 2002.

[49] M. Copel, P. R. Varekamp, D. W. Kisker, F. R. McFeely, K. E. Litz, and M. M. Banaszak Holl, "Nucleation of chemical vapor deposited silicon nitride on silicon dioxide," *Applied Physics Letters,* vol. 74, pp. 1830-1832, 1999/03/29 1999.

[50] M. J. K. Junqing Lu, "Control of uniformity in capacitively coupled plasmas considering edge effects," 2004.

[51] H. Dun, P. Pan, F. R. White, and R. W. Douse, "Mechanisms of Plasma ‐ Enhanced Silicon Nitride Deposition Using SiH4 / N 2 Mixture," *Journal of The Electrochemical Society,* vol. 128, pp. 1555-1563, July 1, 1981 1981.

APPENDIX A Matlab Code for WGM in Bragg Fibers

This GUI code is to find the resonant frequencies of cylindrical Bragg resonator using transfer matrix method. The approach used is that of complex frequency instead of complex azimuthal index. See Prkna's paper for details. Propagation constant can be made complex with complex refractive index (which makes azimuthal index complex) or complex frequency. Here we use frequency approach in accordance with Prkna. However instead of frequency, we use complex valued wavelength avoiding dealing with very large numbers. If complex frequency is written as $\tilde{\omega} = \omega' - i\omega''$, ω'' models the temporal decay since $e^{-i\tilde{\omega}t} = e^{-i(\omega' - i\omega'')t} = e^{-i\omega' t} e^{-\omega'' t}$. Note that this is different from the way loss was incorporated in dispersion relation for waveguide with transverse component of wavevector becoming imaginary.

A.1 Program Structure

The basic program structure is as follows. Only necessary functions are shown.

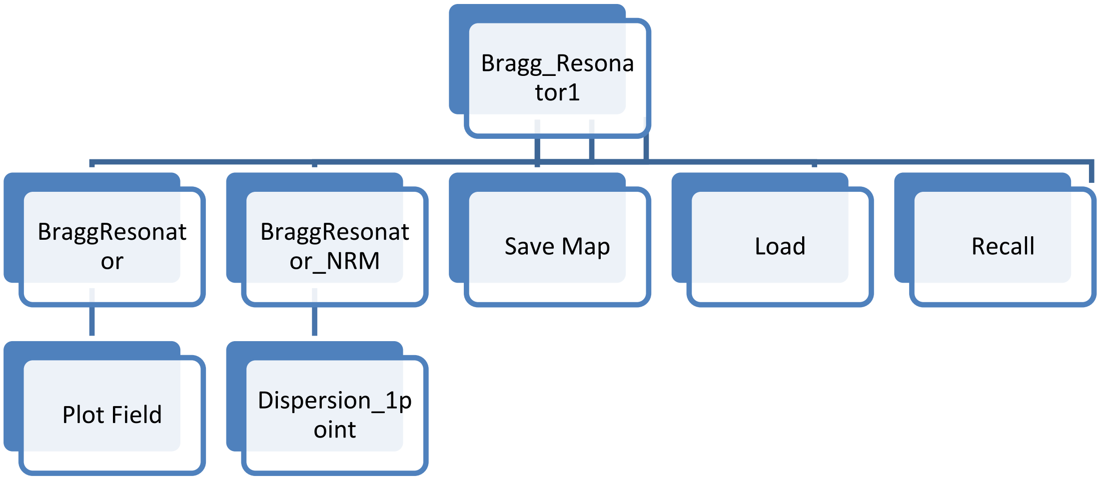

A.2 Instructions to Run the GUI

Start parallelpool with as many cores as possible as the code uses parfor. Use command “Matlabpool open local 2” for 2 cores. To run the GUI, run Bragg_Resonator1.m and not the figure file. This will display the Matlab GUI. Provide the values in all the fields in the left input panel and press Root Search to get the dispersion map. Zoom into the desired root making sure there is preferably only 1 root at the center of the map. To get the precise value and field due to the wavelength at the root, press FineSearch(NRM) button. This gives field plots at the bottom of GUI panel, effective index and peak location. To get the initial map back, press Recall. In order to save a map at any instant, provide filename in the ‘filename’ field and press the Save button. To load a saved map, use Load button. For very cases, if FineSearch(NRM) gives NaN, use FineSearch instead which will take longer to execute. The necessary functions that execute on interacting with the GUI buttons are explained in the next section.

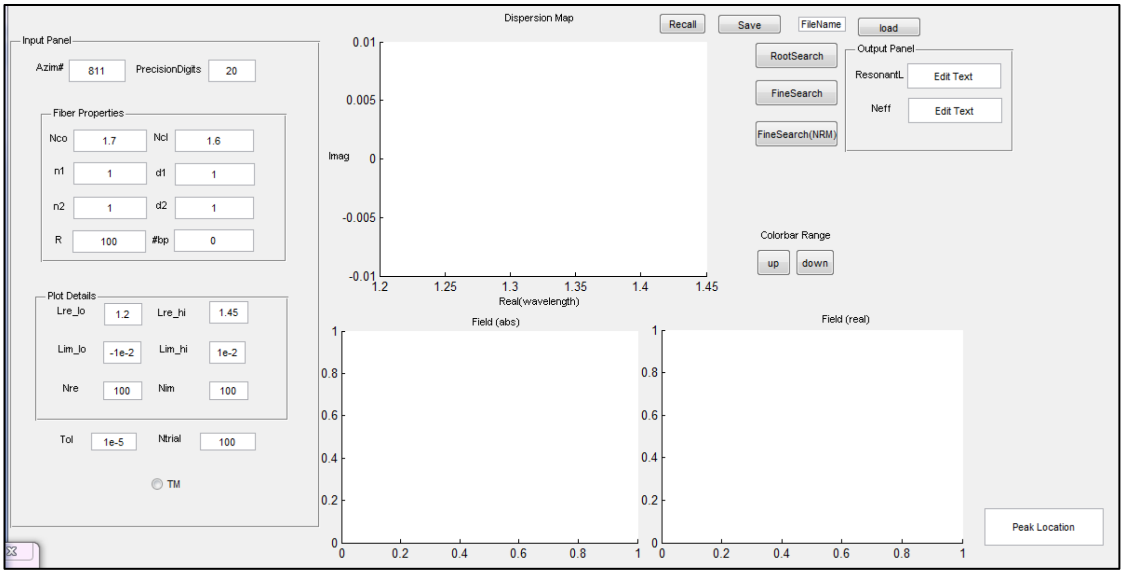

Azim# 811
PrecisionDigits 20
Nco 1.7
Ncl 1.6
n1 1
d1 1
n2 1
d2 1
R 100
#bp 0
Lre_lo 1.2
Lre_hi 1.45
Lim_lo -1e-2
Lim_hi 1e-2
Nre 100
Nim 100
Tol 1e-5
Ntrial 100
ResonantL Edit Text
Neff Edit Text

A.3 Dispersion Map Calculation

To calculate the dispersion map for the cylinder parameters provided on the input panel, click 'Root Search' button. This calls the function BraggResonator.m given below.

A.3.1 BraggResonator.m

Variable	**Purpose**
Lambda_res	Resonant wavelength (real part of lambda at root)
Neff	Effective refractive index. (from 2*m*PI=k0*neff*2*PI*R)
N	#layers
m	Azimuthal order
n	Vector containing indexes all layers
k	Wavevector at the minimum of dispersion value
r	Vector containing radii
mode	TM or TE
NR	#points on real lambda axis
NI	#points on imag lambda axis

Disk and multilayer have been treated separately. Disk uses the analytical expression while TMM has been used for multilayer.

```
function
[lambda_res,neff,Real_lambda0,Imag_lambda0,dif1,N,m,n,k,r,mode]=BraggRe
sonator(R,Nco,d1,n1,d2,n2,Ncl,N,m,Real_lambda0_low,Real_lambda0_high,Im
ag_lambda0_low,Imag_lambda0_high,precisionNum,mode,NR,NI,handles)
digits(precisionNum);

Real_lambda0=linspace(Real_lambda0_low,Real_lambda0_high,NR); % search
wavelength range (real part)
Imag_lambda0=linspace(Imag_lambda0_low,Imag_lambda0_high,NI); % search
wavelength range (imag part)
```

```
Minv1 = @(M) [M(2,2) -M(1,2);-M(2,1) M(1,1)];
lambda0=zeros(NR,NI);k0=zeros(NR,NI);dif1=zeros(NR,NI);
if N~=0 % for Bragg Resonator, I seperate disk with Bragg
r=zeros(2*N+1,1); % radius of each interface
n=zeros(2*N+2,1); % refractive index of each layer
r(1)=R;n(1)=Nco;n(2*N+2)=Ncl;
for jj=1:N
r(2*jj)=R+(jj-1)*(d1+d2)+d1;
r(2*jj+1)=R+jj*(d1+d2);
n(2*jj)=n1;n(2*jj+1)=n2;
end
r(2*N+2)=r(2*N+1)+50*(d1+d2);

for mm=1:NR
parfor nn=1:NI
    lambda0(mm,nn)=Real_lambda0(mm)+1i*Imag_lambda0(nn);
    k0(mm,nn)=2*pi./lambda0(mm,nn);
    T=[1;0];
    if mode==1 %TM
    for jj=(2*N+1):-1:1
    M1=[besselh(m,1,k0(mm,nn)*n(jj)*r(jj))
besselh(m,2,k0(mm,nn)*n(jj)*r(jj));n(jj)/2*(besselh(m-
1,1,k0(mm,nn)*n(jj)*r(jj))-besselh(m+1,1,k0(mm,nn)*n(jj)*r(jj)))
n(jj)/2*(besselh(m-1,2,k0(mm,nn)*n(jj)*r(jj))-
besselh(m+1,2,k0(mm,nn)*n(jj)*r(jj)))];
    M2=[besselh(m,1,k0(mm,nn)*n(jj+1)*r(jj))
besselh(m,2,k0(mm,nn)*n(jj+1)*r(jj));n(jj+1)/2*(besselh(m-
1,1,k0(mm,nn)*n(jj+1)*r(jj))-besselh(m+1,1,k0(mm,nn)*n(jj+1)*r(jj)))
n(jj+1)/2*(besselh(m-1,2,k0(mm,nn)*n(jj+1)*r(jj))-
besselh(m+1,2,k0(mm,nn)*n(jj+1)*r(jj)))];

    if isequal(M1,M2)%M1==M2
        MM=[1 0;0 1];
    else
    MM=vpa(Minv1(M1)*M2);
    end
    T=vpa(MM)*T;
    end
    else %TE
    for jj=(2*N+1):-1:1
    M1=[besselh(m,1,k0(mm,nn)*n(jj)*r(jj))
besselh(m,2,k0(mm,nn)*n(jj)*r(jj));1/n(jj)/2*(besselh(m-
1,1,k0(mm,nn)*n(jj)*r(jj))-besselh(m+1,1,k0(mm,nn)*n(jj)*r(jj)))
1/n(jj)/2*(besselh(m-1,2,k0(mm,nn)*n(jj)*r(jj))-
besselh(m+1,2,k0(mm,nn)*n(jj)*r(jj)))];
    M2=[besselh(m,1,k0(mm,nn)*n(jj+1)*r(jj))
besselh(m,2,k0(mm,nn)*n(jj+1)*r(jj));1/n(jj+1)/2*(besselh(m-
1,1,k0(mm,nn)*n(jj+1)*r(jj))-besselh(m+1,1,k0(mm,nn)*n(jj+1)*r(jj)))
1/n(jj+1)/2*(besselh(m-1,2,k0(mm,nn)*n(jj+1)*r(jj))-
besselh(m+1,2,k0(mm,nn)*n(jj+1)*r(jj)))];
    if isequal(M1,M2)%M1==M2
        MM=[1 0;0 1];
    else
    MM=vpa(Minv1(M1)*M2);
    end
```

```
    T=vpa(MM)*T;
    end
    end
    dif1(mm,nn)=abs(T(2)/T(1)-1);
end
end
%dif1=eval(dif1);
[i1,j1]=find(min(min(dif1))==dif1);
lambda_res=2*pi./real(k0(i1(1),j1(1))); % resonant wavelength
neff=m/R./k0(i1(1),j1(1)); % effective index
k=k0(i1(1),j1(1));
[X,Y]=meshgrid(Real_lambda0,Imag_lambda0); % root plot
axes(handles.axes1)
pcolor(X,Y,-dif1')
shading interp
colorbar
set(handles.edit23,'string',num2str(lambda_res,10))
set(handles.edit24,'string',num2str(neff,10))
```

```
else % for disk resonator
    n(1)=Nco;n(2)=Ncl;r(1)=R;
    if mode==1 % TM
      for mm=1:NR
      for nn=1:NI
       lambda0(mm,nn)=Real_lambda0(mm)+1i*Imag_lambda0(nn);
       k0(mm,nn)=2*pi./lambda0(mm,nn);
       M1=Nco/2*(besselj(m-1,k0(mm,nn)*Nco*R)-
besselj(m+1,k0(mm,nn)*Nco*R))/besselj(m,k0(mm,nn)*Nco*R);
       M2=Ncl/2*(besselh(m-1,1,k0(mm,nn)*Ncl*R)-
besselh(m+1,1,k0(mm,nn)*Ncl*R))/besselh(m,1,k0(mm,nn)*Ncl*R);
       dif1(mm,nn)=abs(M1/M2-1);
      end
      end
   else % TE
    for mm=1:NR
    for nn=1:NI
    lambda0(mm,nn)=Real_lambda0(mm)+1i*Imag_lambda0(nn);
    k0(mm,nn)=2*pi./lambda0(mm,nn);
    M1=Ncl/2*(besselj(m-1,k0(mm,nn)*Nco*R)-
besselj(m+1,k0(mm,nn)*Nco*R))/besselj(m,k0(mm,nn)*Nco*R);
    M2=Nco/2*(besselh(m-1,1,k0(mm,nn)*Ncl*R)-
besselh(m+1,1,k0(mm,nn)*Ncl*R))/besselh(m,1,k0(mm,nn)*Ncl*R);
    dif1(mm,nn)=abs(M1/M2-1);
    end
```

```
    end
   end
% No need for finding minimum when doing first dispersion map with
multiple roots. Needed only during Fine search. That fine search
doesn't zoom into the map and recalculate.
[i1,j1]=find(min(min(dif1))==dif1);
lambda_res=2*pi./real(k0(i1(1),j1(1)));
neff=m/R./k0(i1(1),j1(1));
k=k0(i1(1),j1(1));
[X,Y]=meshgrid(Real_lambda0,Imag_lambda0);
axes(handles.axes1)
pcolor(X,Y,-dif1')%-dif1')
```

```
shading interp
colorbar
%caxis([0 1])
set(handles.edit23,'string',num2str(lambda_res,10))
set(handles.edit24,'string',num2str(neff,10))
end
```

To check for mode condition for particular value of complex lambda.

A.3.2 disperion_1point.m

Variable	Description
d	Dispersion value (complex)
Lr,Li	Real and imag parts of wavelength
Minv	Technically an inline function, not a variable for finding inverse skipping divsion by determinant which could be too small
k0	Wavevector at the that lambda

This function is to check for mode condition at only one point instead of entire map as in BraggResonator.m. In that way this code is no different, just a reduction of BraggResonator. Note that it doesn't use analytical expression for N=0 case. If you want, use dispersion_1point_ .m given next. However result was the same with both probably for the precision we specified. Play with it to see if there is any significant difference.

```
function [ d ] = dispersion_1point( Lr,Li,mode,r,n,N,m,precisionNum,~ )
%"dispersion_1point" calculates dispersion at a given point on the map
ie
%for given real and imaginary parts of lambda
%   Detailed explanation goes here
digits(precisionNum);
Minv = @(matr) [matr(2,2) -matr(1,2);-matr(2,1) matr(1,1)];%earlier
matr=M.  changed just because since I added Minv, an error occurs
saying besselh is not defined for symbolic variables. may be itis
expecting m to be sym
k0=2*pi/(Lr+1i*Li);
T=[1;0];
if mode==1 %TM
    for jj=(2*N+1):-1:1
        M1=[besselh(m,1,k0*n(jj)*r(jj))
besselh(m,2,k0*n(jj)*r(jj));n(jj)/2*(besselh(m-1,1,k0*n(jj)*r(jj))-
besselh(m+1,1,k0*n(jj)*r(jj))) n(jj)/2*(besselh(m-1,2,k0*n(jj)*r(jj))-
besselh(m+1,2,k0*n(jj)*r(jj)))];
        M2=[besselh(m,1,k0*n(jj+1)*r(jj))
besselh(m,2,k0*n(jj+1)*r(jj));n(jj+1)/2*(besselh(m-
1,1,k0*n(jj+1)*r(jj))-besselh(m+1,1,k0*n(jj+1)*r(jj)))
```

```
n(jj+1)/2*(besselh(m-1,2,k0*n(jj+1)*r(jj))-
besselh(m+1,2,k0*n(jj+1)*r(jj)))];

        if isequal(M1,M2)%M1==M2
            MM=[1 0;0 1];
        else
            MM=(Minv(M1)*M2);%MM=vpa(M1\M2);
        end
            T=(MM)*T;%T=vpa(MM)*T;
    end
else %TE
    for jj=(2*N+1):-1:1
        M1=[besselh(m,1,k0*n(jj)*r(jj))
besselh(m,2,k0*n(jj)*r(jj));1/n(jj)/2*(besselh(m-1,1,k0*n(jj)*r(jj))-
besselh(m+1,1,k0*n(jj)*r(jj))) 1/n(jj)/2*(besselh(m-
1,2,k0*n(jj)*r(jj))-besselh(m+1,2,k0*n(jj)*r(jj)))];
        M2=[besselh(m,1,k0*n(jj+1)*r(jj))
besselh(m,2,k0*n(jj+1)*r(jj));1/n(jj+1)/2*(besselh(m-
1,1,k0*n(jj+1)*r(jj))-besselh(m+1,1,k0*n(jj+1)*r(jj)))
1/n(jj+1)/2*(besselh(m-1,2,k0*n(jj+1)*r(jj))-
besselh(m+1,2,k0*n(jj+1)*r(jj)))];
        if isequal(M1,M2)%M1==M2
            MM=[1 0;0 1];
        else
            MM=Minv(M1)*M2;%MM=vpa(M1\M2);
        end
            T=(MM)*T;%T=vpa(MM)*T;
    end
end
  d=(T(2)/T(1)-1);%dispersion
end
```

A.3.3 dispersion_1point_

```
function [ d ] = dispersion_1point( Lr,Li,mode,r,n,N,m,precisionNum,~ )
%"dispersion_1point" calculates dispersion at a given point on the map
ie
%for given real and imaginary parts of lambda
%   Detailed explanation goes here
digits(precisionNum);
Minv = @(matr) [matr(2,2) -matr(1,2);-matr(2,1) matr(1,1)];%earlier
matr=M.  changed just because since I added Minv, an error occurs
saying besselh is not defined for symbolic variables. may be itis
expecting m to be sym
k0=2*pi/(Lr+1i*Li);
T=[1;0];
if N~=0
if mode==1 %TM
    for jj=(2*N+1):-1:1
        M1=[besselh(m,1,k0*n(jj)*r(jj))
besselh(m,2,k0*n(jj)*r(jj));n(jj)/2*(besselh(m-1,1,k0*n(jj)*r(jj))-
besselh(m+1,1,k0*n(jj)*r(jj))) n(jj)/2*(besselh(m-1,2,k0*n(jj)*r(jj))-
besselh(m+1,2,k0*n(jj)*r(jj)))];
```

```
        M2=[besselh(m,1,k0*n(jj+1)*r(jj))
besselh(m,2,k0*n(jj+1)*r(jj));n(jj+1)/2*(besselh(m-
1,1,k0*n(jj+1)*r(jj))-besselh(m+1,1,k0*n(jj+1)*r(jj)))
n(jj+1)/2*(besselh(m-1,2,k0*n(jj+1)*r(jj))-
besselh(m+1,2,k0*n(jj+1)*r(jj)))];

        if isequal(M1,M2)%M1==M2
            MM=[1 0;0 1];
        else
            MM=(Minv(M1)*M2);%MM=vpa(M1\M2);
        end
            T=(MM)*T;%T=vpa(MM)*T;
    end
else %TE
    for jj=(2*N+1):-1:1
        M1=[besselh(m,1,k0*n(jj)*r(jj))
besselh(m,2,k0*n(jj)*r(jj));1/n(jj)/2*(besselh(m-1,1,k0*n(jj)*r(jj))-
besselh(m+1,1,k0*n(jj)*r(jj))) 1/n(jj)/2*(besselh(m-
1,2,k0*n(jj)*r(jj))-besselh(m+1,2,k0*n(jj)*r(jj)))];
        M2=[besselh(m,1,k0*n(jj+1)*r(jj))
besselh(m,2,k0*n(jj+1)*r(jj));1/n(jj+1)/2*(besselh(m-
1,1,k0*n(jj+1)*r(jj))-besselh(m+1,1,k0*n(jj+1)*r(jj)))
1/n(jj+1)/2*(besselh(m-1,2,k0*n(jj+1)*r(jj))-
besselh(m+1,2,k0*n(jj+1)*r(jj)))];
        if isequal(M1,M2)%M1==M2
            MM=[1 0;0 1];
        else
            MM=Minv(M1)*M2;%MM=vpa(M1\M2);
        end
            T=(MM)*T;%T=vpa(MM)*T;
    end
end
  d=(T(2)/T(1)-1);%dispersion
else
    Nco=n(1);Ncl=n(2);R=r(1);
    if mode==1 % TM


       %lambda0(mm,nn)=Real_lambda0(mm)+1i*Imag_lambda0(nn);
       %k0(mm,nn)=2*pi./lambda0(mm,nn);
       M1=Nco/2*(besselj(m-1,k0*Nco*R)-
besselj(m+1,k0*Nco*R))/besselj(m,k0*Nco*R);
       M2=Ncl/2*(besselh(m-1,1,k0*Ncl*R)-
besselh(m+1,1,k0*Ncl*R))/besselh(m,1,k0*Ncl*R);
        d=(M1/M2-1);



   else % TE
    %lambda0(mm,nn)=Real_lambda0(mm)+1i*Imag_lambda0(nn);
    %k0(mm,nn)=2*pi./lambda0(mm,nn);
    M1=Ncl/2*(besselj(m-1,k0*Nco*R)-
besselj(m+1,k0*Nco*R))/besselj(m,k0*Nco*R);
    M2=Nco/2*(besselh(m-1,1,k0*Ncl*R)-
besselh(m+1,1,k0*Ncl*R))/besselh(m,1,k0*Ncl*R);
    d=(M1/M2-1);
```

```
    end
end
```

A.3.4 BraggResonator_NRM.m

Variable	**Purpose**
hx,hy	Delta x and delta y for a derivative
nIter	No. of max iterations, just to give additional control over breaking the loop
dx	Correction vector
n0	Counter for iterations
Dx1	Partial derivative of real part of disp wrt real lambda
Dy1	Partial derivative of real part of disp wrt imag lambda
Dx2	Partial derivative of imag part of disp wrt real lambda
Dy2	Partial derivative of imag part of disp wrt imag lambda
jac	Jacobian formed by these derivatives
de	Determinant of jacobian
xnew	Corrected location on the map closer to the root

The initial location to start with is the midpoint of the map as it is expected that the user zoomed into the root location such that minimum is very close to the center of the map.

```
function
[lambda_res,neff,k,n,r]=BraggResonator_NRM(x,y,tol,nIter,R,Nco,d1,n1,d2
,n2,Ncl,N,m,Real_lambda0_low,Real_lambda0_high,Imag_lambda0_low,Imag_la
mbda0_high,precisionNum,mode,NR,NI,handles)
digits(precisionNum);
format longEng

hx=1e-10;
hy=1e-10;

r=zeros(2*N+1,1); % radius of each interface
n=zeros(2*N+2,1); % refractive index of each layer
r(1)=R;n(1)=Nco;n(2*N+2)=Ncl;
%no check if N > 0. may cause error if N =0
for jj=1:N
r(2*jj)=R+(jj-1)*(d1+d2)+d1;
r(2*jj+1)=R+jj*(d1+d2);
n(2*jj)=n1;n(2*jj+1)=n2;
end
r(2*N+2)=r(2*N+1)+50*(d1+d2);

%n(1)=Nco;n(2)=Ncl;r(1)=R;
ntrial=nIter;
dx=[1;1];n0=0;
while(n0<ntrial || (dx(1)+dx(2))>tol)
    n0=n0+1;
    %partial derivative
```

```
    Dx1=((real(dispersion_1point(x+hx,y,mode,r,n,N,m,precisionNum))-
real(dispersion_1point(x,y,mode,r,n,N,m,precisionNum)))/hx);
    Dy1=((real(dispersion_1point(x,y+hy,mode,r,n,N,m,precisionNum))-
real(dispersion_1point(x,y,mode,r,n,N,m,precisionNum)))/hy);
    Dx2=((imag(dispersion_1point(x+hx,y,mode,r,n,N,m,precisionNum))-
imag(dispersion_1point(x,y,mode,r,n,N,m,precisionNum)))/hx);
    Dy2=((imag(dispersion_1point(x,y+hy,mode,r,n,N,m,precisionNum))-
imag(dispersion_1point(x,y,mode,r,n,N,m,precisionNum)))/hy);
    jac=([Dx1,Dy1;Dx2,Dy2])
    de=(det(jac));
    dx=-(([Dy2 -Dy1; -Dx2
Dx1])*[real(dispersion_1point(x,y,mode,r,n,N,m,precisionNum));imag(disp
ersion_1point(x,y,mode,r,n,N,m,precisionNum))]);
    %dx=-jac^-
1*[real(dispersion_1point(x,y,mode,r,n,N,m,precisionNum));imag(dispersi
on_1point(x,y,mode,r,n,N,m,precisionNum))];
%     xnew=[x;y]+dx;
dx=(dx/de)
xnew=([x;y]+dx);%changed line
    x=xnew(1);
    y=xnew(2);
end
lambda_res=x;
k=2*pi/(x+1i*y);
neff=m/R/(2*pi/(x+1i*y));
set(handles.edit23,'string',num2str(lambda_res,10))
set(handles.edit24,'string',num2str(neff,10))
end
```

A.4 Algorithm for Quick Root Search

A.4.1 Newton Raphson Method in 2D

To determine the root on the dispersion map to desired precision, Newton Raphson method was employed. The basic idea of this method is to move closer to the root by a correction factor determined by the Taylor series expansion. Or simply, as shown for the situation in the figure below, move back by δx from the current position whose value should be δx = F(x)/F’(x), since F(x)/ δx=F’(x). So move from the current location where the derivative is being calculated by δx in –ve direction or x_new= x_current - δx. Repeat the process at this new location until the error is below a lower limit you provide.

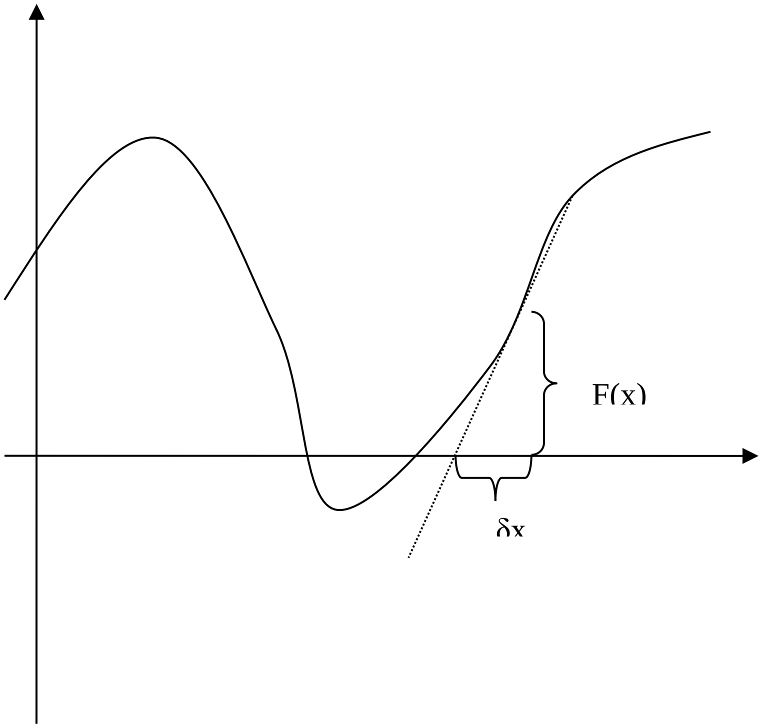

The generalization of this method to 2 functions, which is what we are concerned with, is as follows. For two functions $F_1(x_1, x_2)$ and $F_2(x_1, x_2)$, Taylor series expansion in the vicinity of a point X, neglecting higher order terms , can be written as

$$F_j(X+\delta X) \approx F_j(X) + \sum_i \frac{\partial F_j}{\partial x_i}\delta x_i$$

As the functions at $X+\delta X$ should approach 0 simultaneously, since we are looking for a root, equating the above to 0 for both functions can be written in matrix form as

$$\begin{bmatrix} F_1(x_1,x_2) \\ F_2(x_1,x_2) \end{bmatrix} + \begin{bmatrix} \frac{\partial F_1}{\partial x_1} & \frac{\partial F_1}{\partial x_2} \\ \frac{\partial F_2}{\partial x_1} & \frac{\partial F_2}{\partial x_2} \end{bmatrix} \begin{bmatrix} \delta x_1 \\ \delta x_2 \end{bmatrix} = 0$$

Therefore the correction factor for the real and imaginary parts of lambda is given by

$$\begin{bmatrix} \delta x_1 \\ \delta x_2 \end{bmatrix} = -\begin{bmatrix} \dfrac{\partial F_1}{\partial x_1} & \dfrac{\partial F_1}{\partial x_2} \\ \dfrac{\partial F_2}{\partial x_1} & \dfrac{\partial F_2}{\partial x_2} \end{bmatrix}^{-1} \begin{bmatrix} F_1(x_1, x_2) \\ F_2(x_1, x_2) \end{bmatrix}$$

This correction is then added to the current coordinates on the map, moving to a new location closer to the root and the process is repeated.

In our case for finding the root on a 2D plot, real and imag axes of wavelength serve as the 2 independent variables x_1 and x_2 while $F_1(x_1, x_2)$ and $F_2(x_1, x_2)$ are extracted from the complex value of dispersion ($d = a + i\,b$) at that complex wavelength ($x_1 + i\,x_2$). $F_1(x_1, x_2)$ is a and $F_2(x_1, x_2)$ is b. This complex dispersion value d is given by dispersion_1point(). Derivatives are calculated numerically using steps of hx for derivative wrt x and hy for y. To avoid 'matrix close to singular' warning, jacobian^-1 operation has not been used. Instead elements of the matrix have been swapped and negated as done for a 2x2 matrix inverse. You can play with the step size for calculating the derivative (hx and hy). I have used 1e-10. Tol is the tolerance for the error. Ntrial is the upper limit on iterations for reaching the root to a precision given by tol.

A.5 The GUI Code Explained

Bragg_Resonator1

There is a lot of redundancy you can find in this code and in many places in BraggResonator. Remove it to have a cleaner code. To make your life easy, only useful lines have been distilled out here. Once I had tried to rename the functions to have self-evident names. Some error had occurred after which I dropped the idea to save time and continued with edit23 etc. type of names adding just a comment to show what the function is doing. Blocks of coherent code are to improve readability.

```
function varargout = Bragg_Resonator1(varargin)
gui_Singleton = 1;
gui_State = struct('gui_Name',       mfilename, ...
                   'gui_Singleton',  gui_Singleton, ...
                   'gui_OpeningFcn', @Bragg_Resonator1_OpeningFcn, ...
                   'gui_OutputFcn',  @Bragg_Resonator1_OutputFcn, ...
                   'gui_LayoutFcn',  [] , ...
                   'gui_Callback',   []);
if nargin && ischar(varargin{1})
    gui_State.gui_Callback = str2func(varargin{1});
end

if nargout
    [varargout{1:nargout}] = gui_mainfcn(gui_State, varargin{:});
else
    gui_mainfcn(gui_State, varargin{:});
end
% End initialization code - DO NOT EDIT
```

```
% --- Executes just before Bragg_Resonator1 is made visible.
function Bragg_Resonator1_OpeningFcn(hObject, eventdata, handles,
varargin)
% This function has no output args, see OutputFcn.
handles.output = hObject;
handles.map=zeros(10);
% Update handles structure
guidata(hObject, handles);
function varargout = Bragg_Resonator1_OutputFcn(hObject, eventdata,
handles)
% hObject    handle to figure
varargout{1} = handles.output;
% --- Executes on button press in pushbutton2.
```

```
%%RootSearch%gives the map
function pushbutton2_Callback(hObject, eventdata, handles)
R=str2num(get(handles.edit1,'String'));
Nco=str2num(get(handles.edit2,'String'));
d1=str2num(get(handles.edit5,'String'));
n1=str2num(get(handles.edit4,'String'));
d2=str2num(get(handles.edit7,'String'));
n2=str2num(get(handles.edit6,'String'));
Ncl=str2num(get(handles.edit3,'String'));
N=str2num(get(handles.edit17,'String'));
m=str2num(get(handles.edit18,'String'));
Real_lambda0_low=str2num(get(handles.edit8,'String'));
Real_lambda0_high=str2num(get(handles.edit9,'String'));
Imag_lambda0_low=str2num(get(handles.edit10,'String'));
Imag_lambda0_high=str2num(get(handles.edit11,'String'));
NR=str2num(get(handles.edit19,'String'));
```

```
NI=str2num(get(handles.edit20,'String'));
precisionNum=str2num(get(handles.edit16,'String'));
mode=get(handles.radiobutton1,'Value');

[lambda_res,neff,Real_lambda0,Imag_lambda0,dif1,N,m,n,k,r,mode]=BraggRe
sonator(R,Nco,d1,n1,d2,n2,Ncl,N,m,Real_lambda0_low,Real_lambda0_high,Im
ag_lambda0_low,Imag_lambda0_high,precisionNum,mode,NR,NI,handles);
handles.map=-dif1';
%xlswrite('Map',handles.map);
guidata(hObject,handles);%updates the object to include
map values
```

```
% --- Executes on button press in pushbutton3.
```

%%FineSearch

```
%not a very different function. Doesn’t zoom in. Just calculates the map again in the region you
manually zoomed into and gives the minimum.%%

function pushbutton3_Callback(hObject, eventdata, handles)
R=str2num(get(handles.edit1,'String'));
Nco=str2num(get(handles.edit2,'String'));
d1=str2num(get(handles.edit5,'String'));
n1=str2num(get(handles.edit4,'String'));
d2=str2num(get(handles.edit7,'String'));
n2=str2num(get(handles.edit6,'String'));
Ncl=str2num(get(handles.edit3,'String'));
N=str2num(get(handles.edit17,'String'));
m=str2num(get(handles.edit18,'String'));
x_range=get(handles.axes1,'Xlim');
y_range=get(handles.axes1,'Ylim');
Real_lambda0_low=x_range(1);
Real_lambda0_high=x_range(2);
Imag_lambda0_low=y_range(1);
Imag_lambda0_high=y_range(2);
NR=str2num(get(handles.edit19,'String'));
NI=str2num(get(handles.edit20,'String'));
precisionNum=str2num(get(handles.edit16,'String'));
mode=get(handles.radiobutton1,'Value');

[lambda_res,neff,Real_lambda0,Imag_lambda0,dif1,N,m,n,k,r,mode]=BraggRe
sonator(R,Nco,d1,n1,d2,n2,Ncl,N,m,Real_lambda0_low,Real_lambda0_high,Im
ag_lambda0_low,Imag_lambda0_high,precisionNum,mode,NR,NI,handles);
plotabs(N,m,n,k,r,mode,handles)
plotreal(N,m,n,k,r,mode,handles)
```

```
% --- Executes on button press in pushbutton4.
```

%%FineSearch(NRM)

```
function pushbutton4_Callback(hObject, eventdata, handles)
R=str2num(get(handles.edit1,'String'));
Nco=str2num(get(handles.edit2,'String'));
```

```
d1=str2num(get(handles.edit5,'String'));
n1=str2num(get(handles.edit4,'String'));
d2=str2num(get(handles.edit7,'String'));
n2=str2num(get(handles.edit6,'String'));
Ncl=str2num(get(handles.edit3,'String'));
N=str2num(get(handles.edit17,'String'));
m=str2num(get(handles.edit18,'String'));
tol=str2num(get(handles.edit21,'String'));
nIter=str2num(get(handles.edit22,'String'));
x_range=get(handles.axes1,'Xlim');
y_range=get(handles.axes1,'Ylim');
Real_lambda0_low=x_range(1);
Real_lambda0_high=x_range(2);
Imag_lambda0_low=y_range(1);
Imag_lambda0_high=y_range(2);
x=(Real_lambda0_low+Real_lambda0_high)/2;y=(Imag_lambda0_low+Imag_lambd
a0_high)/2;
NR=str2num(get(handles.edit19,'String'));
NI=str2num(get(handles.edit20,'String'));
precisionNum=str2num(get(handles.edit16,'String'));
mode=get(handles.radiobutton1,'Value');
[lambda_res,neff,k,n,r]=BraggResonator_NRM(x,y,tol,nIter,R,Nco,d1,n1,d2
,n2,Ncl,N,m,Real_lambda0_low,Real_lambda0_high,Imag_lambda0_low,Imag_la
mbda0_high,precisionNum,mode,NR,NI,handles);
plotabs(N,m,n,k,r,mode,handles)
plotreal(N,m,n,k,r,mode,handles)
```

```
function edit23_Callback(hObject, eventdata, handles)
%        str2double(get(hObject,'String')) returns contents of edit23
as a double
% --- Executes during object creation, after setting all properties.
function edit23_CreateFcn(hObject, eventdata, handles)
% Hint: edit controls usually have a white background on Windows.
%       See ISPC and COMPUTER.
if ispc && isequal(get(hObject,'BackgroundColor'),
get(0,'defaultUicontrolBackgroundColor'))
    set(hObject,'BackgroundColor','white');
end
```

```
function edit24_Callback(hObject, eventdata, handles)
% --- Executes during object creation, after setting all properties.
function edit24_CreateFcn(hObject, eventdata, handles)
if ispc && isequal(get(hObject,'BackgroundColor'),
get(0,'defaultUicontrolBackgroundColor'))
    set(hObject,'BackgroundColor','white');
end
function edit16_Callback(hObject, eventdata, handles)
% --- Executes during object creation, after setting all properties.
function edit16_CreateFcn(hObject, eventdata, handles)
if ispc && isequal(get(hObject,'BackgroundColor'),
get(0,'defaultUicontrolBackgroundColor'))
```

```
    set(hObject,'BackgroundColor','white');
end
function edit18_Callback(hObject, eventdata, handles)
function edit18_CreateFcn(hObject, eventdata, handles)
if ispc && isequal(get(hObject,'BackgroundColor'),
get(0,'defaultUicontrolBackgroundColor'))
    set(hObject,'BackgroundColor','white');
end
function edit21_Callback(hObject, eventdata, handles)
function edit21_CreateFcn(hObject, eventdata, handles)
if ispc && isequal(get(hObject,'BackgroundColor'),
get(0,'defaultUicontrolBackgroundColor'))
    set(hObject,'BackgroundColor','white');
end
function edit22_Callback(hObject, eventdata, handles)
function edit22_CreateFcn(hObject, eventdata, handles)
if ispc && isequal(get(hObject,'BackgroundColor'),
get(0,'defaultUicontrolBackgroundColor'))
    set(hObject,'BackgroundColor','white');
end
function radiobutton1_Callback(hObject, eventdata, handles)
function edit8_Callback(hObject, eventdata, handles)
function edit8_CreateFcn(hObject, eventdata, handles)
if ispc && isequal(get(hObject,'BackgroundColor'),
get(0,'defaultUicontrolBackgroundColor'))
    set(hObject,'BackgroundColor','white');
end
function edit9_Callback(hObject, eventdata, handles)
function edit9_CreateFcn(hObject, eventdata, handles)
if ispc && isequal(get(hObject,'BackgroundColor'),
get(0,'defaultUicontrolBackgroundColor'))
    set(hObject,'BackgroundColor','white');
end
function edit10_Callback(hObject, eventdata, handles)
function edit10_CreateFcn(hObject, eventdata, handles)
if ispc && isequal(get(hObject,'BackgroundColor'),
get(0,'defaultUicontrolBackgroundColor'))
    set(hObject,'BackgroundColor','white');
end
function edit11_Callback(hObject, eventdata, handles)
function edit11_CreateFcn(hObject, eventdata, handles)
if ispc && isequal(get(hObject,'BackgroundColor'),
get(0,'defaultUicontrolBackgroundColor'))
    set(hObject,'BackgroundColor','white');
end
function edit19_Callback(hObject, eventdata, handles)
function edit19_CreateFcn(hObject, eventdata, handles)
if ispc && isequal(get(hObject,'BackgroundColor'),
get(0,'defaultUicontrolBackgroundColor'))
    set(hObject,'BackgroundColor','white');
end
function edit20_Callback(hObject, eventdata, handles)
function edit20_CreateFcn(hObject, eventdata, handles)
if ispc && isequal(get(hObject,'BackgroundColor'),
get(0,'defaultUicontrolBackgroundColor'))
    set(hObject,'BackgroundColor','white');
end
```

```
function edit2_Callback(hObject, eventdata, handles)
function edit2_CreateFcn(hObject, eventdata, handles)
if ispc && isequal(get(hObject,'BackgroundColor'),
get(0,'defaultUicontrolBackgroundColor'))
    set(hObject,'BackgroundColor','white');
end
function edit3_Callback(hObject, eventdata, handles)
function edit3_CreateFcn(hObject, eventdata, handles)
if ispc && isequal(get(hObject,'BackgroundColor'),
get(0,'defaultUicontrolBackgroundColor'))
    set(hObject,'BackgroundColor','white');
end
```

```
function edit4_Callback(hObject, eventdata, handles)
function edit4_CreateFcn(hObject, eventdata, handles)
if ispc && isequal(get(hObject,'BackgroundColor'),
get(0,'defaultUicontrolBackgroundColor'))
    set(hObject,'BackgroundColor','white');
end
function edit5_Callback(hObject, eventdata, handles)
function edit5_CreateFcn(hObject, eventdata, handles)
if ispc && isequal(get(hObject,'BackgroundColor'),
get(0,'defaultUicontrolBackgroundColor'))
    set(hObject,'BackgroundColor','white');
end
function edit6_Callback(hObject, eventdata, handles)
function edit6_CreateFcn(hObject, eventdata, handles)
if ispc && isequal(get(hObject,'BackgroundColor'),
get(0,'defaultUicontrolBackgroundColor'))
    set(hObject,'BackgroundColor','white');
end
function edit7_Callback(hObject, eventdata, handles)
function edit7_CreateFcn(hObject, eventdata, handles)
if ispc && isequal(get(hObject,'BackgroundColor'),
get(0,'defaultUicontrolBackgroundColor'))
    set(hObject,'BackgroundColor','white');
end
function edit1_Callback(hObject, eventdata, handles)
function edit1_CreateFcn(hObject, eventdata, handles)
if ispc && isequal(get(hObject,'BackgroundColor'),
get(0,'defaultUicontrolBackgroundColor'))
    set(hObject,'BackgroundColor','white');
end
function edit17_Callback(hObject, eventdata, handles)
function edit17_CreateFcn(hObject, eventdata, handles)
if ispc && isequal(get(hObject,'BackgroundColor'),
get(0,'defaultUicontrolBackgroundColor'))
    set(hObject,'BackgroundColor','white');
end
```

%Recall

```
function pushbutton6_Callback(hObject, eventdata, handles)
color_range=get(handles.axes1,'Clim');
```

```
newcolor_range=[color_range(1)*2 0];
set(handles.axes1,'Clim',newcolor_range)
function pushbutton7_Callback(hObject, eventdata, handles)
color_range=get(handles.axes1,'Clim');
newcolor_range=[color_range(1)/2 0];
set(handles.axes1,'Clim',newcolor_range)
function pushbutton8_Callback(hObject, eventdata, handles)
Real_lambda0_low=str2num(get(handles.edit8,'String'));
Real_lambda0_high=str2num(get(handles.edit9,'String'));
Imag_lambda0_low=str2num(get(handles.edit10,'String'));
Imag_lambda0_high=str2num(get(handles.edit11,'String'));
NR=str2num(get(handles.edit19,'String'));
NI=str2num(get(handles.edit20,'String'));
Real_lambda0=linspace(Real_lambda0_low,Real_lambda0_high,NR); % search wavelength range (real part)
Imag_lambda0=linspace(Imag_lambda0_low,Imag_lambda0_high,NI); % search wavelength range (imag part)
[X,Y]=meshgrid(Real_lambda0,Imag_lambda0);
 axes(handles.axes1)
x1=handles.map;
 pcolor(X,Y,x1)
 shading interp
 colorbar
```

```
% --- Executes on button press in pushbutton9.
```

% Save map

```
function pushbutton9_Callback(hObject, eventdata, handles)
R=str2num(get(handles.edit1,'String'));
Nco=str2num(get(handles.edit2,'String'));
d1=str2num(get(handles.edit5,'String'));
n1=str2num(get(handles.edit4,'String'));
d2=str2num(get(handles.edit7,'String'));
n2=str2num(get(handles.edit6,'String'));
Ncl=str2num(get(handles.edit3,'String'));
N=str2num(get(handles.edit17,'String'));
m=str2num(get(handles.edit18,'String'));
Real_lambda0_low=str2num(get(handles.edit8,'String'));
Real_lambda0_high=str2num(get(handles.edit9,'String'));
Imag_lambda0_low=str2num(get(handles.edit10,'String'));
Imag_lambda0_high=str2num(get(handles.edit11,'String'));
NR=str2num(get(handles.edit19,'String'));
NI=str2num(get(handles.edit20,'String'));
precisionNum=str2num(get(handles.edit16,'String'));
mode=get(handles.radiobutton1,'Value');
dt={R;Nco;d1;n1;d2;n2;Ncl;N;m;Real_lambda0_low;Real_lambda0_high;Imag_lambda0_low;Imag_lambda0_high;NR;NI;precisionNum;mode};
nm=get(handles.edit25,'String');%edit25 is filename
xlswrite(nm,dt);
xlsappend(nm,handles.map);
```

```
function edit25_Callback(hObject, eventdata, handles)
```

%FileName

```
function edit25_CreateFcn(hObject, eventdata, handles)
if ispc && isequal(get(hObject,'BackgroundColor'),
get(0,'defaultUicontrolBackgroundColor'))
    set(hObject,'BackgroundColor','white');
end
```

%Load

```
function load_button_Callback(hObject, eventdata, handles)

map_=xlsread(filename,'A18:CV117');
params_=xlsread(filename,'A1:A17');
R=params_(1);
Nco=params_(2);
d1=params_(3);
n1=params_(4);
d2=params_(5);
n2=params_(6);
Ncl=params_(7);
N=params_(8);
m=params_(9);
Real_lambda0_low=params_(10);
Real_lambda0_high=params_(11);
Imag_lambda0_low=params_(12);
Imag_lambda0_high=params_(13);
NR=params_(14);
NI=params_(15);
precisionNum=params_(16);
mode=params_(17);
Real_lambda0=linspace(Real_lambda0_low,Real_lambda0_high,NR); % search
wavelength range (real part)
Imag_lambda0=linspace(Imag_lambda0_low,Imag_lambda0_high,NI); % search
wavelength range (imag part)
[X,Y]=meshgrid(Real_lambda0,Imag_lambda0); % root plot
axes(handles.axes1)
pcolor(X,Y,map_)
shading interp
colorbar
set(handles.edit1,'string',num2str(R))
set(handles.edit2,'string',num2str(Nco))
set(handles.edit3,'string',num2str(Ncl))
set(handles.edit4,'string',num2str(n1))
set(handles.edit5,'string',num2str(d1))
set(handles.edit6,'string',num2str(n2))
set(handles.edit7,'string',num2str(d2))
set(handles.edit8,'string',num2str(Real_lambda0_low))
set(handles.edit9,'string',num2str(Real_lambda0_high))
set(handles.edit10,'string',num2str(Imag_lambda0_low))
set(handles.edit11,'string',num2str(Imag_lambda0_high))
set(handles.edit16,'string',num2str(precisionNum))
set(handles.edit17,'string',num2str(N))
set(handles.edit18,'string',num2str(m))
set(handles.edit19,'string',num2str(NR))
set(handles.edit20,'string',num2str(NI))
set(handles.radiobutton1,'Value',mode)
```

```
handles.map=map_;
guidata(hObject,handles);
```

```
function peak_location_Callback(hObject, eventdata, handles)
function peak_location_CreateFcn(hObject, eventdata, handles)
if ispc && isequal(get(hObject,'BackgroundColor'),
get(0,'defaultUicontrolBackgroundColor'))
    set(hObject,'BackgroundColor','white');
end
```

APPENDIX B PECVD Operation for Fiber Coating

B.1 Operating Instructions for Fabrication of Coated Fiber

1- Vent the PECVD chamber to atmosphere.

2- Unscrew the 3 screws on the front port (glass window) to attach the MDC rotary feedthrough (RFT) along with the stepper motor and then screw them back. Note: Due to mechanical issues in the alignment of metal scaffold with the motor and RFT, you cannot tighten the screws on the scaffold fully. Leave them a little loose to allow room for the motor to adjust during motion. I used rubber bands to secure the motor as in the picture. To avoid slippage between the motor wheel and RFT and prevent wearing, slip on a rubber tubing onto the portion of RFT in contact with the wheel. I used a bicycle tire tube, not in the picture. The glue remains can be noticed in that region.

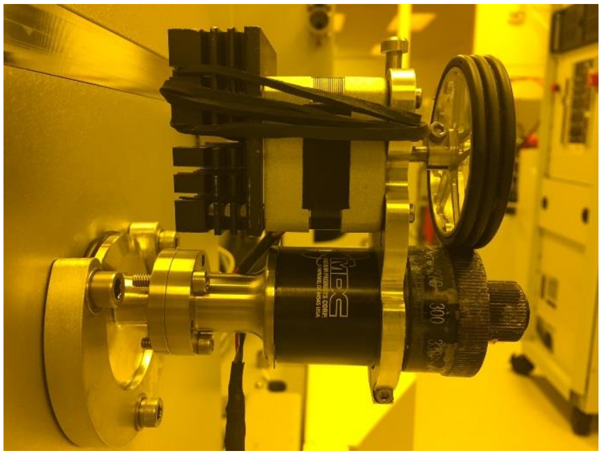

Figure B.1: Side view of rotary feedthrough with stepper motor attached.

3- Now open up the chamber lid on the top. It is quite heavy so be careful.

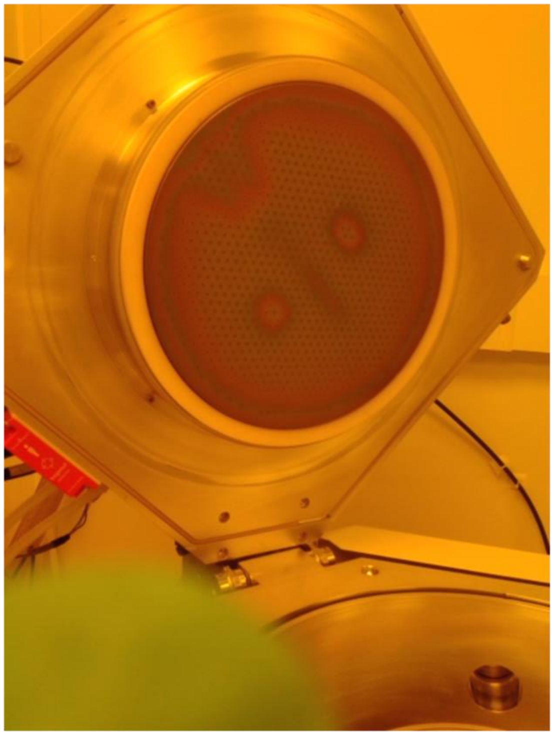

Figure B.2: PECVD chamber lid opened for loading substrates directly into the chamber instead of through loading dock. Here, the chuck with the fiber is mounted into the rotary shaft and place the glass holder with long groove.

4- Place the fiber holding groove on the platen and load the fiber chuck with fiber preloaded into the shaft of RFT. Apply vacuum grease on the chuck if it feels loose in the shaft. Fiber height was kept 4 mm from the platen surface. To repeat the results, use the same height, otherwise growth conditions might change. Cover the groove with another glass piece to secure the fiber.

Figure B.3: Inside view of the chamber showing glass holder placed on the platen and fiber chuck holding the fiber inside rotary shaft.

5- Test the rotation of fiber before closing the lid to make sure fiber is not slipping. The fiber should rotate smoothly without any jerks.

6- Now close the lid and pump to base pressure.

7- It takes about 3 hours to reach chamber leak rate of 1mTorr/min. You can perform a Leak Check of the chamber to find the rate. You will see the APC close on the process module tab on starting leak check. The test will take 6 minutes. Leak Check result should be 1mTorr/min. After the test is over ‘Pump to Base’ will start automatically. If you stop the leak check before 6 mins, you’ll have to run ‘Pump to Base’ manually.

8- Turn the motor on. Adjust the speed to the desired value with the potentiometer inside the control box.

9- Run the recipe. Watch for the plasma to strike through one of the viewing windows. If you don’t see the glow, there is some issue and report to the cleanroom manager. Also watch out for alarms on the Process Module tab.

Sometimes the gas supply is disrupted for some reason. Report that and get it fixed.

10- Occasionally check if all is going fine for long recipes. You don't want to pay for the lost time.

B.2 Software Interface

On logging into the FOM account, access to the software interface is enabled. The main screen is shown below. Since we are not loading the sample through the loading dock, 'Transport Module' is irrelevant. The photo below is of the Process Module showing schematic of the PECVD tool with gas ports, RF generators, electrodes, APC, pressure gauges etc. When plasma is supposed to strike, it shows a pink cloud between the electrodes.

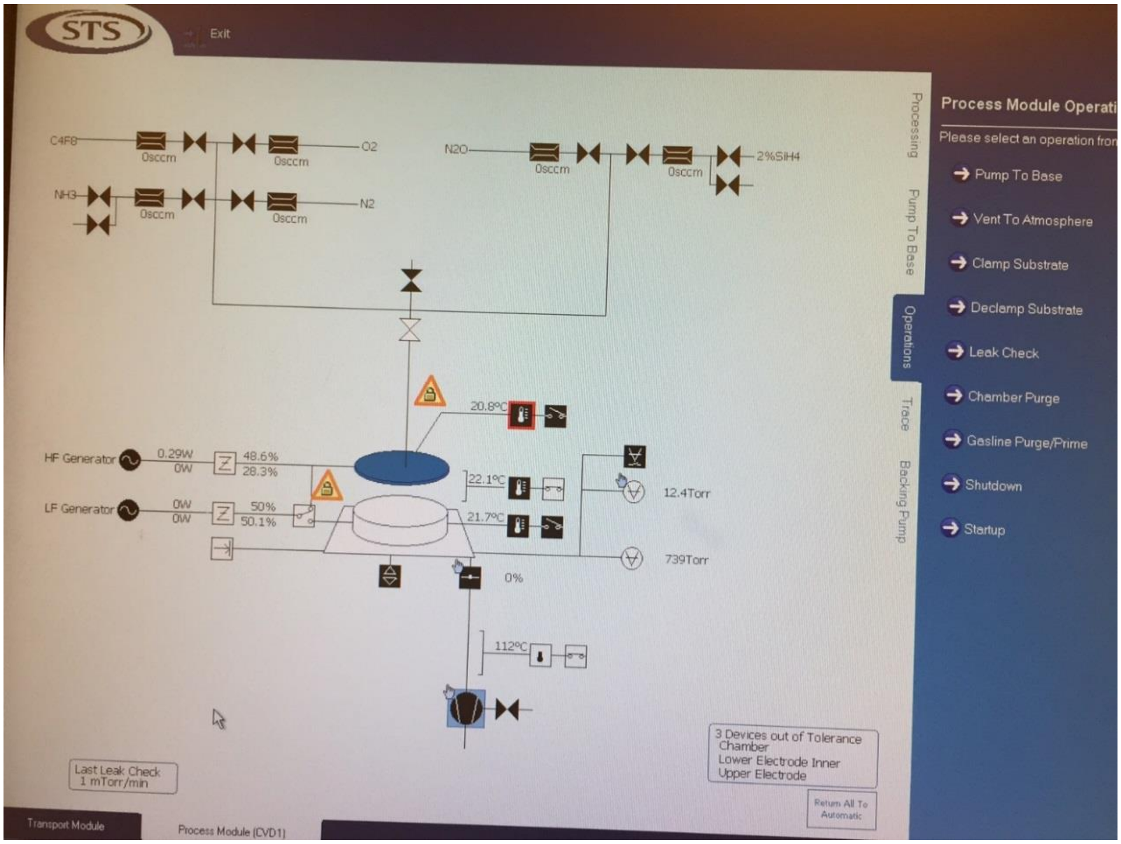

Last Leak Check
1 mTorr/min

3 Devices out of Tolerance
Chamber
Lower Electrode Inner
Upper Electrode

Figure B.4: Process Module interface.

On the right hand side in the picture, Operations tab is selected and Process Module Operations are seen listed. Clicking an operation opens its menu. To select a recipe to run, go to Processing tab and select the recipe and click ‘Start’.

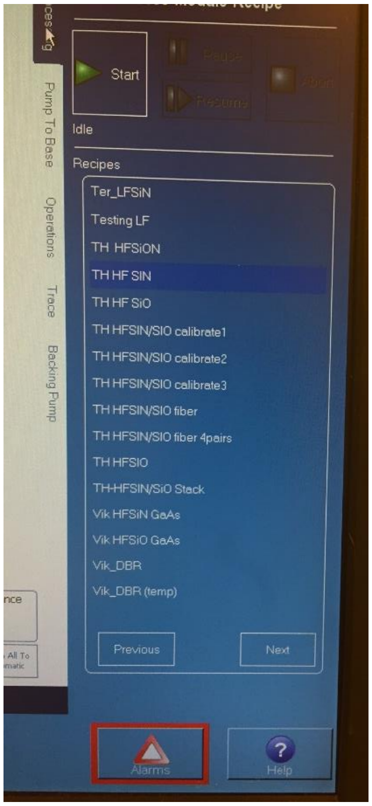

Figure B.5: Recipe selection panel.

B.2.1 Recipes for Silicon Nitride and Silica

All stored recipes starting with ‘TH HF’ are made by THRG members. Here HF stands for High Frequency as 13.56 MHz generator is employed in these recipes. HFSiN and HFSiO are the stored recipes for silicon nitride and silica. The process parameters for each can be seen in the screenshots below.

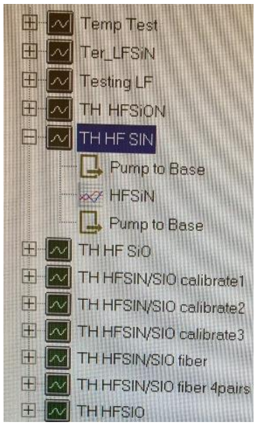

Figure B.6: Menu of recipes. 'Pump to Base' necessary before and after each deposition of a material.

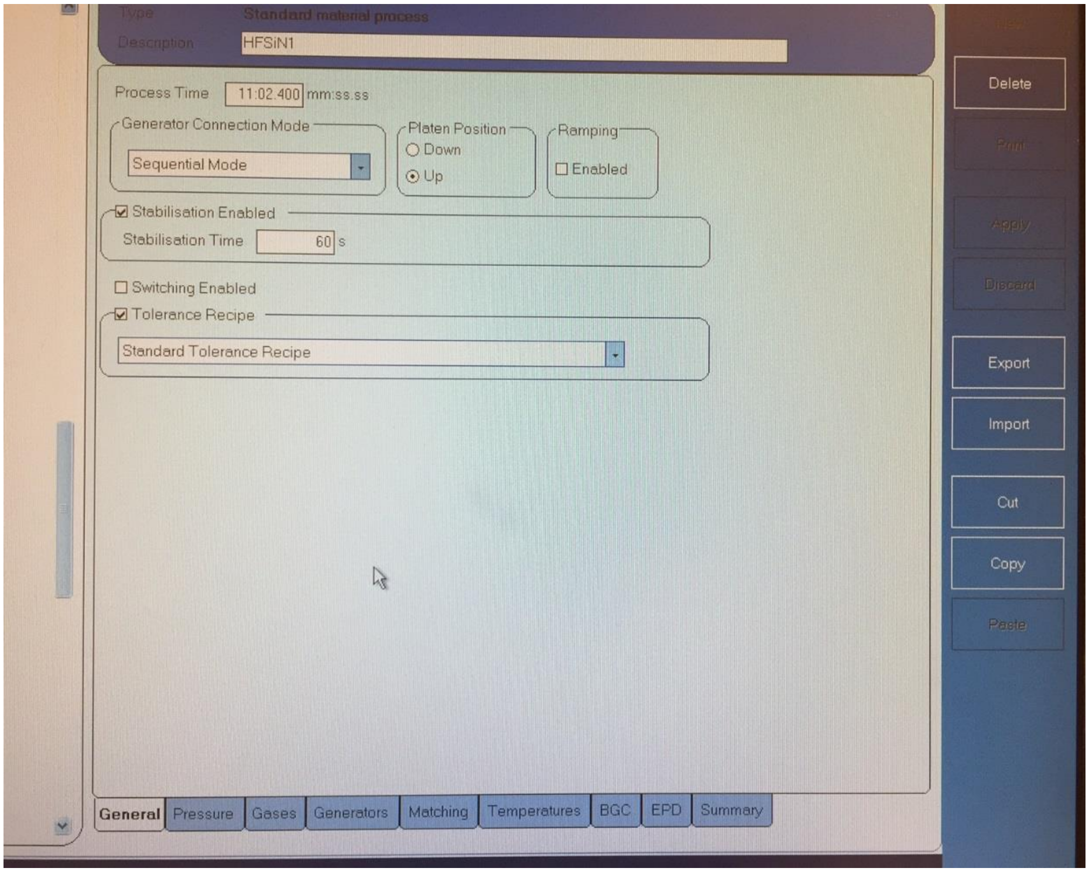
Type Standard material process

Description HFSiN1

Process Time 11:02.400 mm:ss.ss

Generator Connection Mode: Sequential Mode

Platen Position: ○ Down ● Up

Ramping: ☐ Enabled

☑ Stabilisation Enabled

Stabilisation Time 60 s

☐ Switching Enabled

☑ Tolerance Recipe

Standard Tolerance Recipe

Figure B.7: Tabs to define a recipe for material deposition. Appear on clicking 'HFSiN'

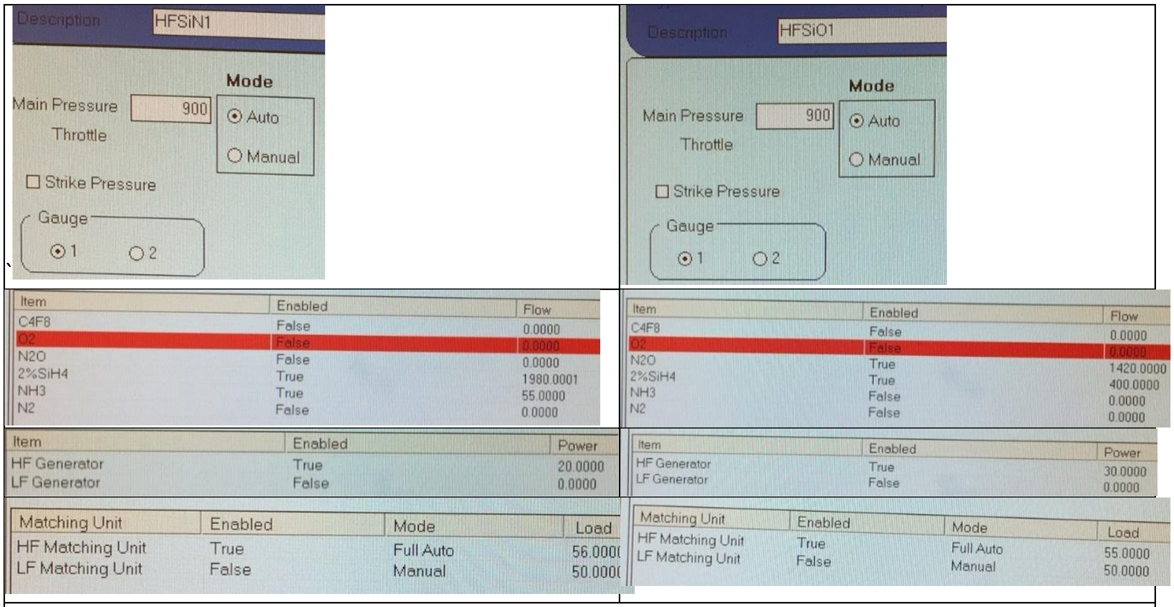

Description HFSiN1

Main Pressure 900

Throttle

Mode

● Auto

○ Manual

☐ Strike Pressure

Gauge ● 1 ○ 2

Item	Enabled	Flow
C4F8	False	0.0000
O2	False	0.0000
N2O	False	0.0000
2%SiH4	True	1980.0001
NH3	True	55.0000
N2	False	0.0000

Item	Enabled	Power
HF Generator	True	20.0000
LF Generator	False	0.0000

Matching Unit	Enabled	Mode	Load
HF Matching Unit	True	Full Auto	56.000
LF Matching Unit	False	Manual	50.000

Description HFSiO1

Main Pressure 900

Throttle

Mode

● Auto

○ Manual

☐ Strike Pressure

Gauge ● 1 ○ 2

Item	Enabled	Flow
C4F8	False	0.0000
O2	False	0.0000
N2O	True	1420.0000
2%SiH4	True	400.0000
NH3	False	0.0000
N2	False	0.0000

Item	Enabled	Power
HF Generator	True	30.0000
LF Generator	False	0.0000

Matching Unit	Enabled	Mode	Load
HF Matching Unit	True	Full Auto	55.0000
LF Matching Unit	False	Manual	50.0000

Figure B.8: Settings for Pressure, Gase Flow rate (sccm), Generator and matching unit for Silicon Nitride (left) and Silica (right).

APPENDIX C SEM of Films Deposited by PECVD

C.1 Calibration of Deposition Rate by SEM

To calibrate the deposition rate of the SiN_x and SiO_2 films, two methods were adopted. In the first one, a single multilayered fiber was fabricated with alternating layers of SiN_x and SiO_2 with increasing deposition times. Later, several fibers were coated with single layer of either SiN_x or SiO_2. SEM images of the coated films were processed to obtain the deposition rate.

C.1.1 Single Fiber with Multiple Layers

The SEM micrograph of the multilayered fiber fabricated for calibration is shown in Figure C.1 and layer sequence is given in Table 10. To create the calibration graph, each material (SiN_x / SiO_2) was deposited for 6 increasing deposition times spaced by 4 minutes while SiO_2 deposition times were spaced by 10 seconds. To have an extra data point, each deposition was repeated once forming a total of 24 layers. The SEM shows the 24 films consisting of 12 the pairs of SiN_x/SiO_2. The thinner layers are of SiO_2.

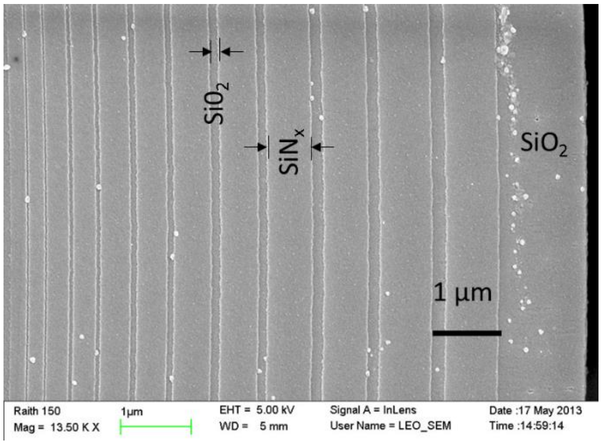

Figure C.1: SEM micrograph of a multilayered fiber coating. Substrate fiber (FT200EMT), not shown in the image lies on the left side followed by 6 pairs of bilayers of SiN_x and SiO_2 layers making the 24 layers in the image. The 6 deposition times for SiN_x are 10, 14, 18, 22, 26 and 30 minutes, while those for SiO_2 are 10, 20, 30, 40, 50 and 60 seconds. The last layer is terminated by a thick layer of SiO_2 deposited for 360 sec.

Closer images were taken as seen in Figure C.2 and processed in Matlab (code given in this section) to obtain the sum of intensity from top to bottom of the image giving peaks (Figure C.3) at the location of interface between layers of SiN_x and SiO_2. The width of the peaks gives the error bar.

Table 10: Layer sequence for multilayered fiber for growth rate calibration.

Layer #	Material	Deposition Time
1	SiN_x	10 min
2	SiO_2	10 sec
3	SiN_x	10 min
4	SiO_2	10 sec
5	SiN_x	14 min
6	SiO_2	20 sec
7	SiN_x	14 min
8	SiO_2	20 sec
9	SiN_x	18 min
10	SiO_2	30 sec
11	SiN_x	18 min
12	SiO_2	30 sec
13	SiN_x	22 min
14	SiO_2	40 sec
15	SiN_x	22 min
16	SiO_2	40 sec
17	SiN_x	26 min
18	SiO_2	50 sec
19	SiN_x	26 min
20	SiO_2	50 sec
21	SiN_x	30 min
22	SiO_2	60 sec
23	SiN_x	30 min
24	SiO_2	60 sec
25	SiO_2	360 sec

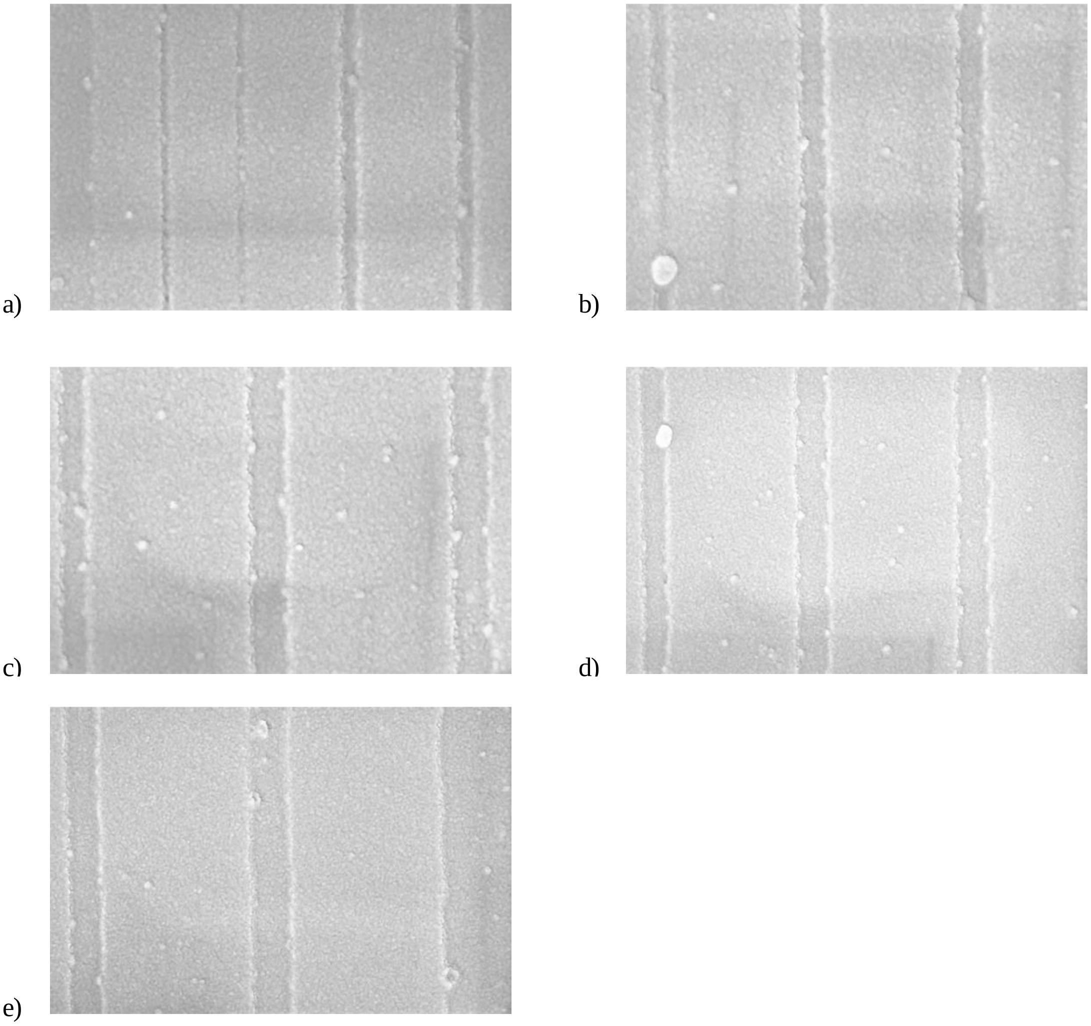

Figure C.2: Zoomed-in SEM images of alternating layers of SiN_x and SiO_2 used to extract thicknesses of the layers. The information bar has been cropped out to convert the image to grayscale. Layers 1-8, 8-12, 12-16, 16-20, 20-23.

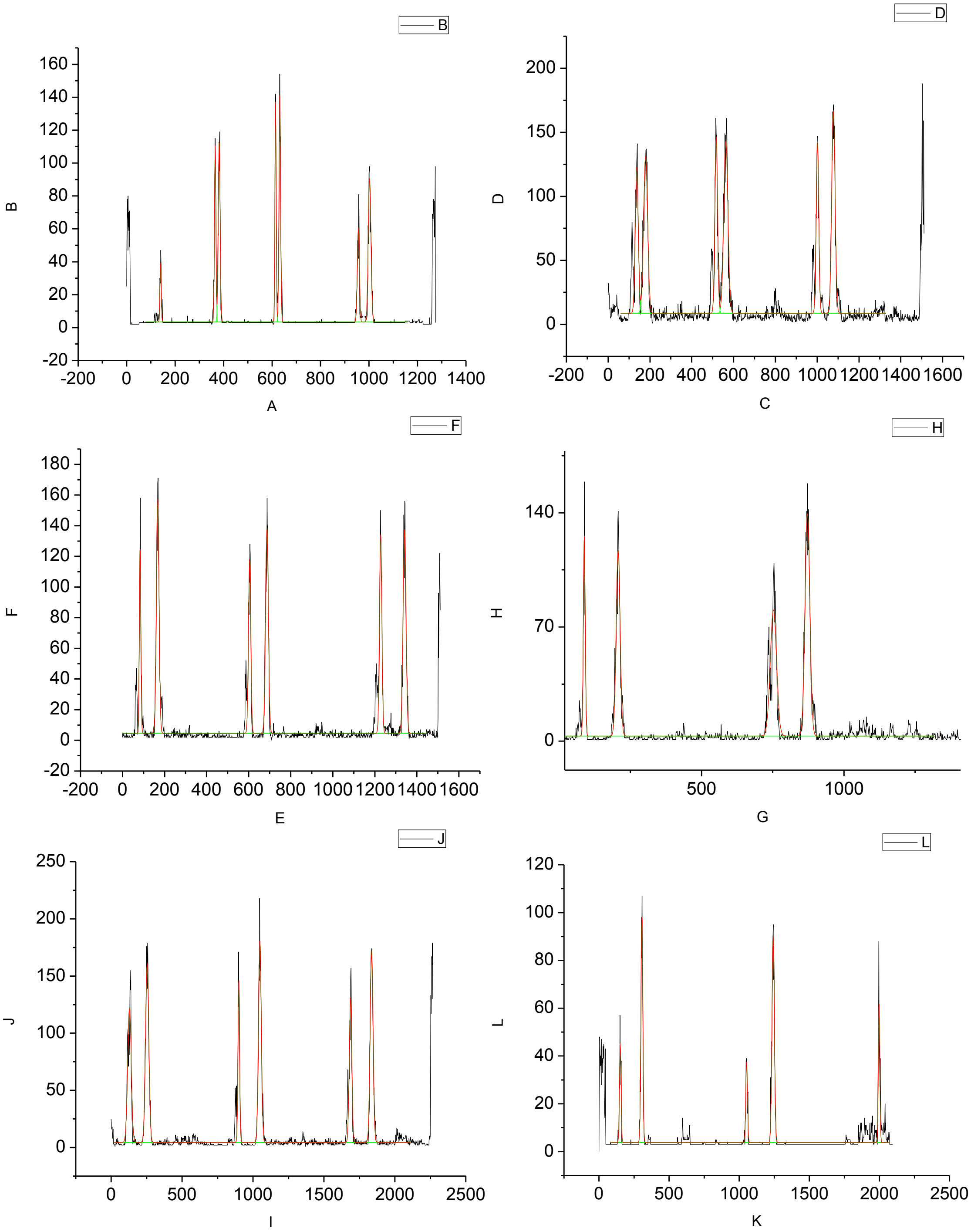

Figure C.3: SEM image intensity summed top to bottom. Layers 1-6, 6-10, 10-14, 14-16, 16-20, 20-23

Calibration curves obtained from three such points around the fiber cross section are given in Figure C.4 and values of thicknesses are tabulated in Table 11. The slopes of these curves is about 26 nm/min differing only at the scale of Angstroms.

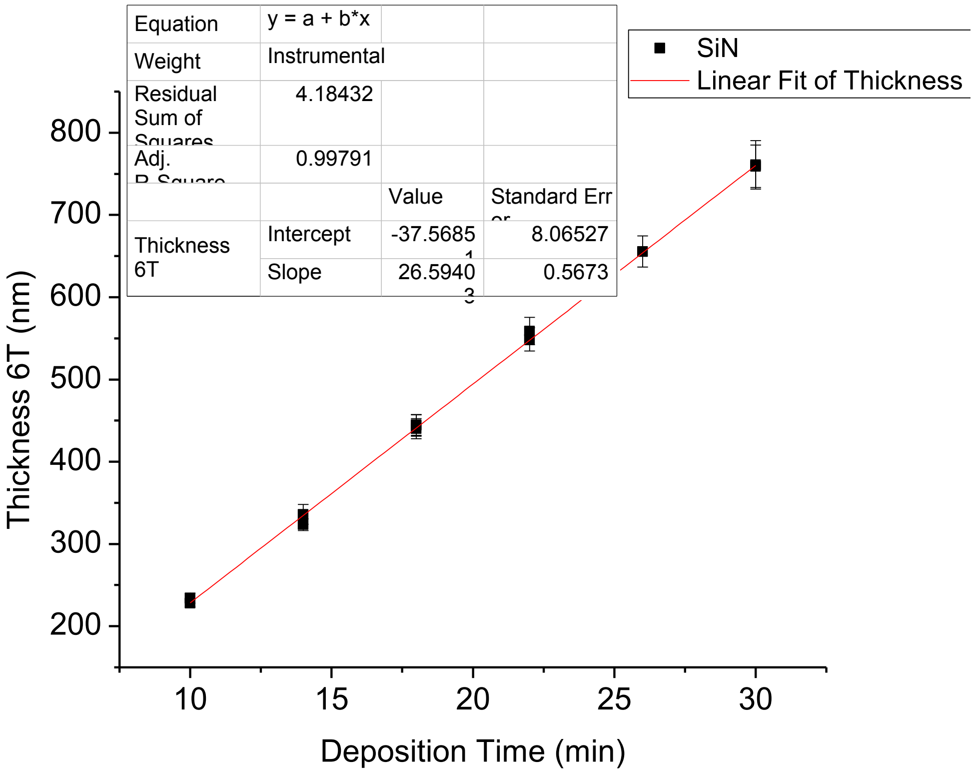
Equation
y = a + b*x
Weight
Instrumental
Residual Sum of Squares
4.18432
Adj. R-Square
0.99791
Value
Standard Error
Thickness 6T
Intercept
-37.56851
8.06527
Slope
26.59403
0.5673
SiN
Linear Fit of Thickness
Thickness 6T (nm)
200
300
400
500
600
700
800
10
15
20
25
30
Deposition Time (min)

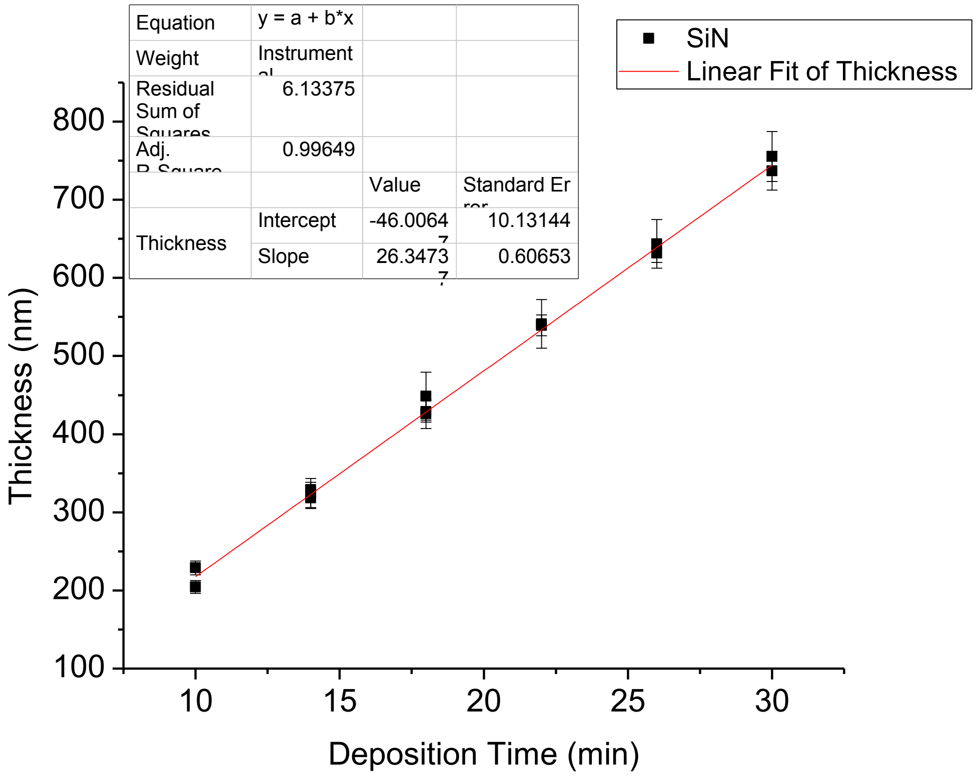
Equation
y = a + b*x
Weight
Instrumental
Residual Sum of Squares
6.13375
Adj. R-Square
0.99649
Value
Standard Error
Thickness
Intercept
-46.00647
10.13144
Slope
26.34737
0.60653
SiN
Linear Fit of Thickness
Thickness (nm)
100
200
300
400
500
600
700
800
10
15
20
25
30
Deposition Time (min)

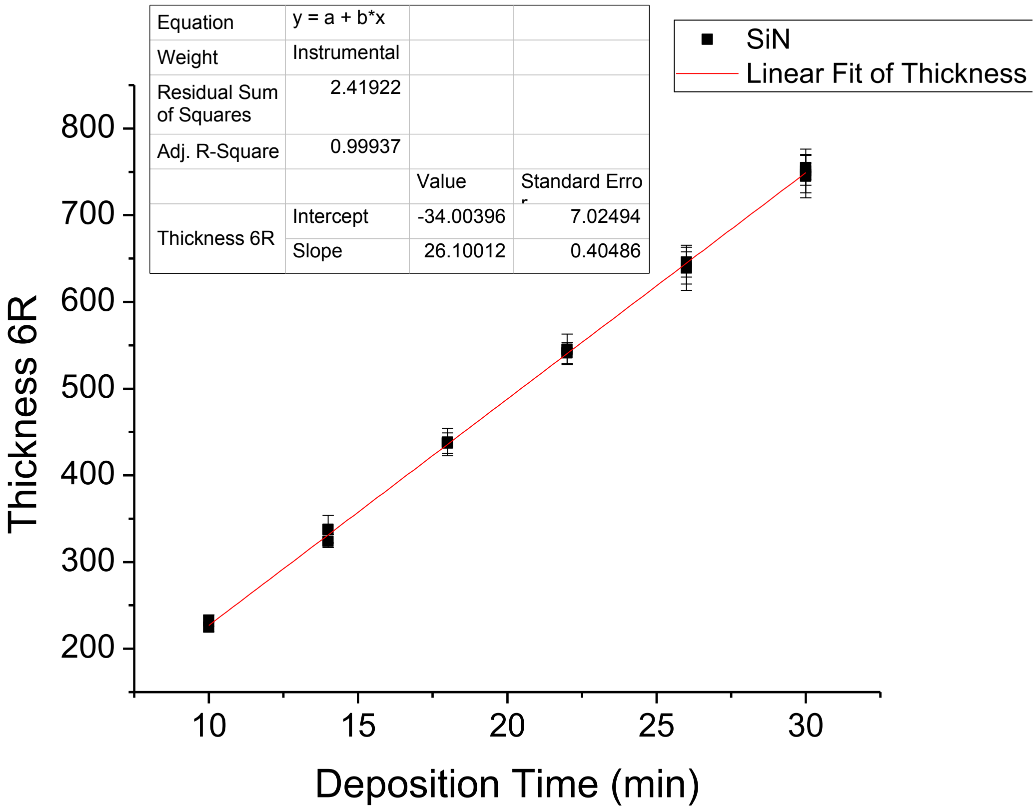

Equation	y = a + b*x		
Weight	Instrumental		
Residual Sum of Squares	2.41922		
Adj. R-Square	0.99937		
		Value	Standard Error
Thickness 6R	Intercept	-34.00396	7.02494
	Slope	26.10012	0.40486

Figure C.4: Growth Rate curve from three points around the fiber cross section.

Matlab code for processing of SEM images

```
clc;
I= imread('SEM_FileName.tif');
%If image when cropped becomes m X n X 4 instead of m X n X 3, then
include I=I(:,:,1:3)

im=rgb2gray(I);
%im=imrotate(im,0.5);
figure, imshow(im), title('original image');
im=imadjust(im);imshow(im)
% im=medfilt2(im,[3 3]);
% h = fspecial('average');
% im = imfilter(im,h);
% imshow(im), title('averaged');

im = wiener2(im,[12 12]);%wiener filter working good for 100kx images
% figure, imshow(im)
% im=im2bw(im,0.01);%could be very helping or very harmful..depends on
image.
% try removing or including it in the code to see the effect..and play
with
% param
% figure, imshow(im)
[junk threshold] = edge(im, 'sobel');
fudgeFactor = .5;
```

```
BWs = edge(im,'sobel', threshold * fudgeFactor);
figure, imshow(BWs), title('binary gradient mask');

e=im2double(BWs);
e1=e(1,:);
for d=1:size(e,1)
    e1=e1+e(d,:);
end
figure
 subplot(2,1,1)
plot(e1)
data=[1:size(e,2) ; e1]';
xlim([0 size(e,2)]);
 subplot(2,1,2)

imshow(e),title('edge detect');
axis normal

se90 = strel('line', 3, 90);
se0 = strel('line', 1, 0);
BWsdil = imdilate(BWs, [se90 se0]);
figure, imshow(BWsdil), title('dilated gradient mask');

e=im2double(BWsdil);
e1=e(1,:);
for d=1:size(e,1)
    e1=e1+e(d,:);
end
figure
 subplot(2,1,1)
plot(e1)
xlim([0 size(e,2)]);
 subplot(2,1,2)

 imshow(e),title('dilated');
axis normal

seD = strel('diamond',1);
BWfinal = imerode(BWsdil,seD);
BWfinal = imerode(BWfinal,seD);
e=im2double(BWfinal);
e1=e(1,:);
% Summing intensity
for d=1:size(e,1)
    e1=e1+e(d,:);
end
figure
 subplot(2,1,1)
plot(e1)

xlim([0 size(e,2)]);
 subplot(2,1,2)

 imshow(e),title('Eroded');
axis normal
figure, imshow(BWfinal), title('segmented image');
```

```
BWoutline = bwperim(BWfinal);
Segout = I;
Segout(BWoutline) = 255;
figure, imshow(Segout), title('outlined original image');
```

Table 11: Thicknesses obtained from SEM images of layers for the 3 points around the cross section.

Time (min)	Thickness1 (nm)	Error1 (nm)	Time (min)	Thickness2 (nm)	Error2 (nm)	Time (min)	Thickness3 (nm)	Error3 (nm)
10	225	5.5	10	228	4.5	10	204.5	8.1
10	232.5	6.5	10	234.2	6.1	10	228.9	8.8
14	324.1	7.6	14	323.4	6.9	14	318.4	12.5
14	337.8	15.9	14	335.8	12	14	323.9	19.3
18	438.3	15.8	18	440.3	12.3	14	328.9	9.5
18	437.2	11.8	18	444.2	13.2	18	429.1	13.6
22	541	12.1	18	444.6	12.3	18	448.4	30.7
22	545.3	17.7	22	548.8	14.1	18	426.1	18.8
26	645.7	17.2	22	558.7	16.7	22	541	31.1
26	639	18.5	26	655.5	18.9	22	539.3	13.2
26	639.3	26	30	759.2	25.8	26	631.7	11.7
30	745	24.9	30	761.1	29.5	26	643.6	31
30	751	25.2				30	737.1	24.7
30	747.3	12.7				30	755.4	32
30	754.9	14.2						

SiO$_2$		
Time (s)	Thickness (nm)	Error (nm)
10	16.8	6.8
10	17.5	5.9
20	46.4	9.7
20	42.2	16.8
20	46.1	16.1
30	76.2	14.0
30	83.5	9.8
30	82.5	12.0
40	113.4	12.4
40	118.7	10.1
40	119.4	19.3
40	124.9	23.6
50	156.9	27.8
50	154.8	25.4
50	149.1	15.7
50	148.4	18.9

50	154.2	12.2
60	189.4	14.6
60	191.6	26.2
360	1245	27.9

C.1.2 Multiple Fibers with Single Layer Deposition

One layer of silicon nitride with different deposition time was deposited on 4 fibers and SEM was performed to obtain the deposition rate. SEM was taken at only one point unlike for the multilayered fiber. The slope is in agreement with the multilayer fiber.

Table 12: Thickness obtained from SEM of 4 single layered fibers.

Fiber ID	Deposition Time	Thickness [nm]	Error [nm]
ZN9	10:49	251	14
ZN11	29	704	5
ZN12	39:1	984	9
ZN13	112:48	2947	21

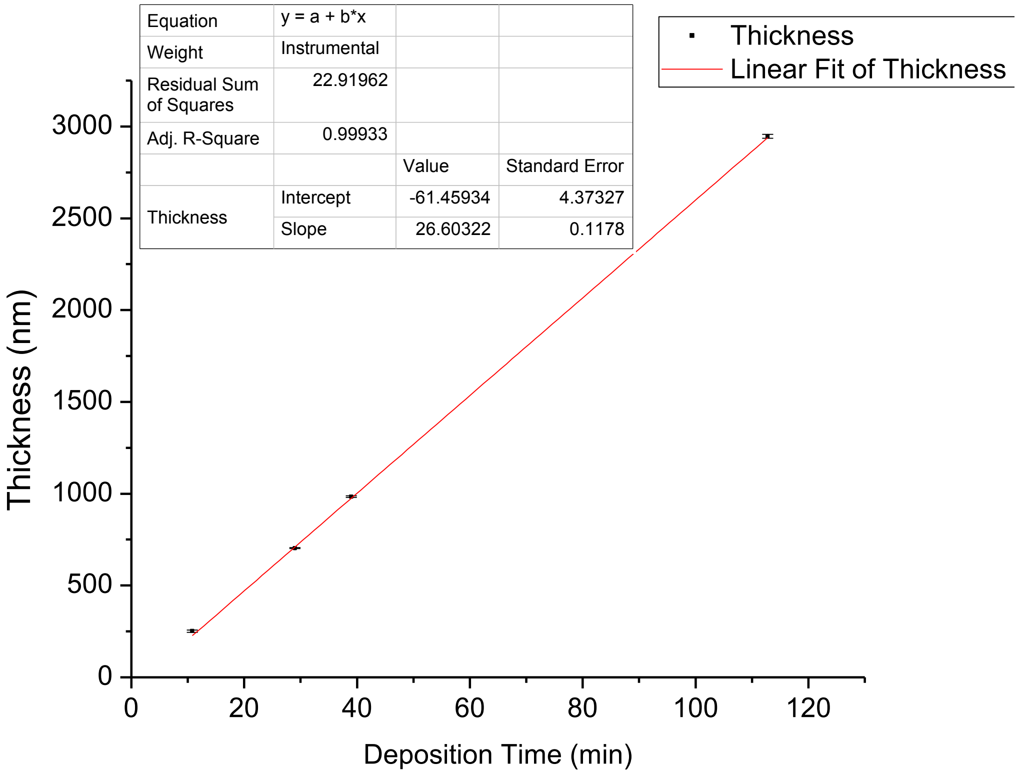

Equation	y = a + b*x		
Weight	Instrumental		
Residual Sum of Squares	22.91962		
Adj. R-Square	0.99933		
		Value	Standard Error
Thickness	Intercept	-61.45934	4.37327
	Slope	26.60322	0.1178

Figure C.5: Growth Rate curve obtained from single layers deposited on different fibers.

APPENDIX D SPEED DEPENDENT REFRACTIVE INDEX

D.1 Experiment and Results

Different growth kinetics observed for static (Figure 4.17) and dynamic deposition method (rotation) on fibers called for an investigation of effect of rotation speed. Four fibers were coated with silicon nitride for 21 minutes at different RPM's. During test rotation, the fiber rotates smooth and calm. But during deposition, as seen through the chamber viewing port, the fiber vibrates erratically as if some extra electrostatic forces are acting due to possible charging of the objects introduced in the otherwise relatively empty chamber. Naturally vibrations amplify with speed. The optical images of the fabricated fibers in Figure D.1 have a greenish-brown hue with ZN17 (30 rpm) more dominantly green. As mentioned in Chapter 3, this difference could be due to the fact that color also depends on the point along the axis of the fiber imaged.

The coated fibers were characterized by Mie scattering. The scattering patterns with best-fit patterns obtained are given in Figure D.1 and characterization results in Table 13. Note that the pattern of ZN16 is similar to ZN17 while that of ZN22 is similar to ZN23. This is because ZN16 and ZN17 were made out of old spool of substandard SMF28 of unknown origin while ZN22 and ZN23 out of high quality spool of SMF28e+ distributed by Fiber Instrument Sales. Running the root search for refractive index, thickness and diameter of the substrate fiber as in Chapter 4 gave the values in Table 13.

The refractive index (*n*) is increasing monotonically with speed (Figure D.2) while thickness has an overall increasing trend with a probable outlier at 15 rpm which could be due to axial non-uniformity of the thickness. The extent of axial non-uniformity should be characterized by SEM to estimate the degree of thickness variation in the fiber samples.

Nevertheless, the increase in refractive index is certain and has not been reported elsewhere. Note that n for 3 rpm is close to that of silicon nitride at 632.8 nm. That means rotation speed is what is affecting the composition more than elevation of the sample.

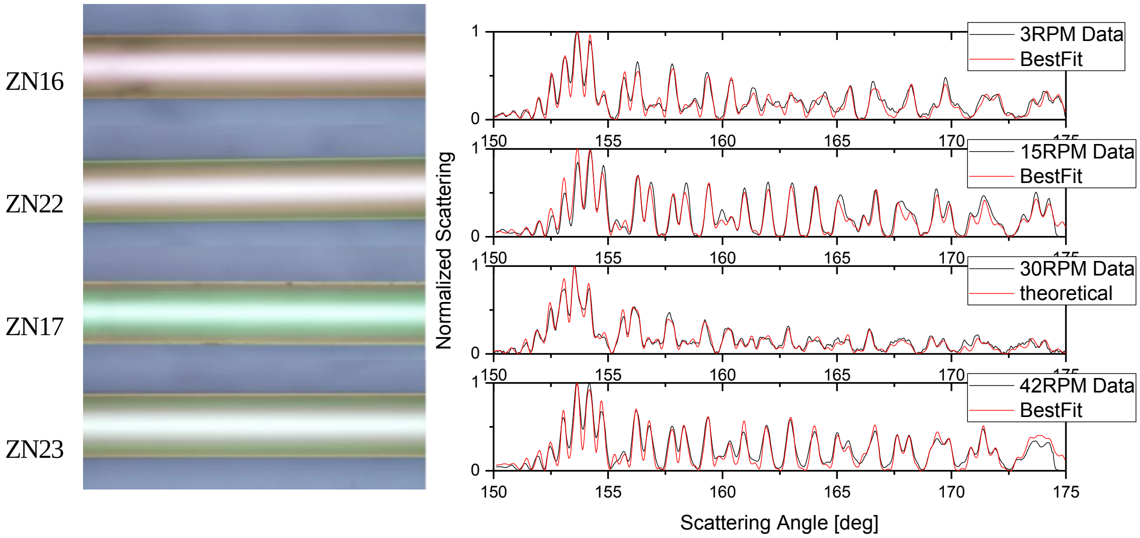

Figure D.1: Experimental Data vs best-fit scattering pattern for fibers fabricated at different rotation speed.

Table 13: Roots search result

Fiber ID	Deposition Time [min]	Material	RPM	Root		
				n	*t* [nm]	*d* [μm]
ZN16	21	SiN_x	3	1.95	435	124.83
ZN22	21	SiN_x	15	2.19	315	124.92
ZN17	21	SiN_x	30	2.49	502	124.99
ZN23	21	SiN_x	42	2.59	510	124.69

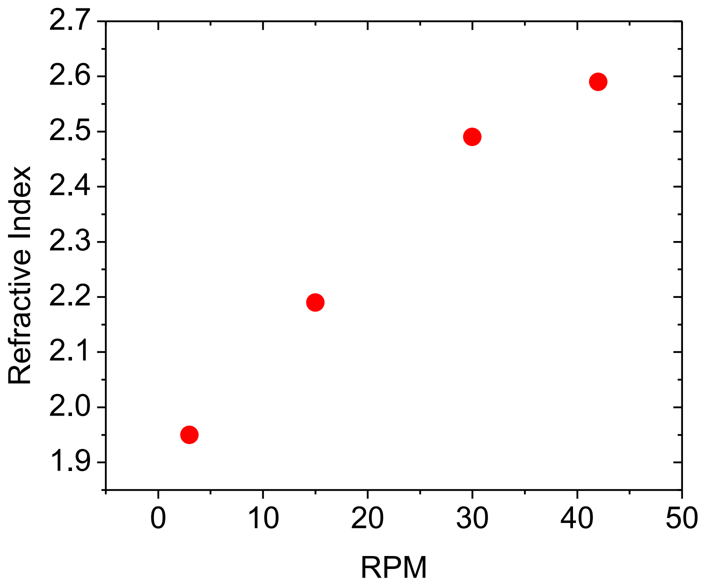

Figure D.2: Refractive index of SiN_x films as a function of RPM determined from scattering of the coated fibers. Four fibers were coated at 3, 15, 30 and 42 RPM respectively.

D.2 Discussion

The dependence of film properties on rotation speed is not surprising as gradual deposition of the amorphous material is a multistep process each happening at a rate determined by deposition conditions. Figure D.3 lists the differences in the deposition conditions for static, slow and fast rotating fiber.

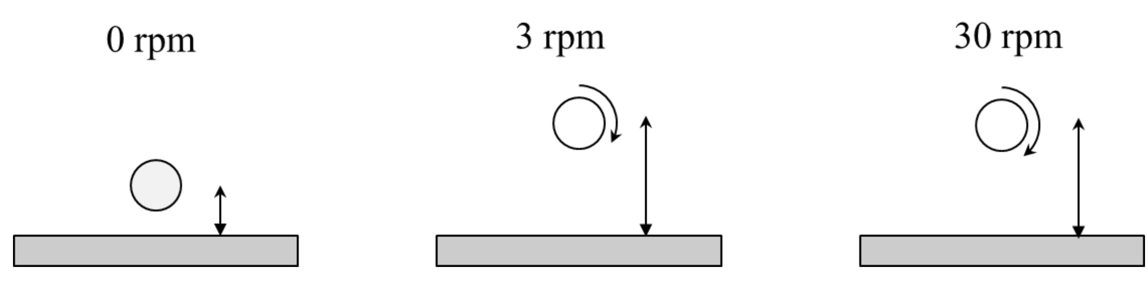

Lower Height	Higher	Higher
Metal Ring – affects flow field	Metal chuck	Metal chuck
Temperature – Higher	Lower	Lower
Temperature – Constant	Cycling	Cycling faster
Reactant flux – Non-uniform around the fiber	Uniform	Uniform
Static	Rotating calmly	Rotating with vigorous occasional vibration

Figure D.3: Comparison of deposition conditions for stationary, slow and fast rotating fiber.

Explanation of the apparent increase in RI in specific needs investigation as we don't have a conjecture as to why the density or Si-content increased with speed which are two possible factor of increased RI. It has been acknowledged in literature that many of the processes leading to film deposition in PECVD are not well understood [48]. Apart from the normally occurring processes such as electron impact creating ionized species, their transport to substrate, surface migration, chemical reactions and desorption, in this case a substrate of small surface area – a fiber is hanging in the middle of the plasma cloud supported by a metal chuck, unlike a wafer that is in contact with the base platen generally. It is known that geometry and material of the objects present in the plasma affect the flow field distribution and ion density which affect the film composition and thickness [50].

A factor affecting density is ion bombardment rate [48] which controls the precursor mobility on the surface. Higher ion bombardment rate means denser film thus higher index. Another factor is rooted in the nature of initial stages of growth of SiN_x on silica. SiN_x/SiO_2 interface is non-wettable leading to formation of 'islands' [49] as the ions migrate on the surface to growth sites and react. These islands eventually coalesce with continued deposition forming a solid continuous film while the unreacted volatile components desorb out of the film. If there isn't enough time and temperature for the ions to migrate, the film composition and physical properties will differ with speed. Also, as the fiber is cycling through the temperature gradient between the electrodes, rate of surface migration is expected to depend on speed [51]. To understand the initial growth stages, SEM of initial deposition would be helpful. As far as Si content is concerned, an XRD or Micro-Raman or other techniques are required to get the film composition.